

South Dakota State University

# Open PRAIRIE: Open Public Research Access Institutional Repository and Information Exchange

---

Electronic Theses and Dissertations

---

2021

## Design, Synthesis, and Evaluation of Glutathione Derivatives as Brain Targeting Agents

Yue Huang

*South Dakota State University*

Follow this and additional works at: <https://openprairie.sdstate.edu/etd>



Part of the [Pharmacy and Pharmaceutical Sciences Commons](#)

---

### Recommended Citation

Huang, Yue, "Design, Synthesis, and Evaluation of Glutathione Derivatives as Brain Targeting Agents" (2021). *Electronic Theses and Dissertations*. 5642.

<https://openprairie.sdstate.edu/etd/5642>

This Dissertation - Open Access is brought to you for free and open access by Open PRAIRIE: Open Public Research Access Institutional Repository and Information Exchange. It has been accepted for inclusion in Electronic Theses and Dissertations by an authorized administrator of Open PRAIRIE: Open Public Research Access Institutional Repository and Information Exchange. For more information, please contact [michael.biondo@sdstate.edu](mailto:michael.biondo@sdstate.edu).

DESIGN, SYNTHESIS, AND EVALUATION OF GLUTATHIONE DERIVATIVES  
AS BRAIN TARGETING AGENTS

BY

YUE HUANG

A dissertation submitted in partial fulfillment of the requirements for the

Doctor of Philosophy

Major in Pharmaceutical Science

South Dakota State University

2021

## DISSERTATION ACCEPTANCE PAGE

Yue Huang

This dissertation is approved as a creditable and independent investigation by a candidate for the Doctor of Philosophy degree and is acceptable for meeting the dissertation requirements for this degree. Acceptance of this does not imply that the conclusions reached by the candidate are necessarily the conclusions of the major department.

Xiangming Guan  
Advisor

Date

Omathanu Perumal  
Department Head

Date

Nicole Lounsbery, PhD  
Director, Graduate School

Date

## ACKNOWLEDGEMENTS

First of all, I would like to express my deep gratitude to Dr. Xiangming Guan for his mentoring, supporting, and guiding both in the work and life in the past five years. Without his help and encouragement, this work would not be possible. I would also like to thank my committee members, Dr. Teresa Seefeldt, Dr. Hemachand Tummala, and Dr. Lan Xu for their support and suggestions during my Ph.D. journey.

I want to acknowledge Dr. Omathanu Perumal, Dr. Hemachand Tummala and Dr. Joshua Reineke for their constructive and critical suggestions raised in my seminars, in particular questions associated with nanoparticle drug delivery related techniques. I would also like to acknowledge Dr. Teresa Seefeldt who guided me in our joint group meetings in the past five years.

I want to deliver my special thanks to the Department of Pharmaceutical Sciences for giving me the opportunity to pursue my Ph.D. and providing me the solid and comprehensive training that definitely will benefit me for my future career. I also want to thank all the graduate students in the department for their help. I really enjoy the time we spent together. It will be a forever memory with me.

Special thanks to my labmates Dr. Shenggang Wang, Dr. Asim Najmi, Dr. Yahya Alqahtani, and Dr. Metab Alharbi for their contribution through lab experiments and/or scientific discussion. I really appreciate our teamwork, our group meetings, and all the time we worked and plaid together. All those moments were enjoyable and unforgettable.

I also would like to thank all the great friends I met at SDSU, especially to Ke Chen, Jie Hu, Zengyue Wang, keliang Wang, Ming Xu, Yiqi Xu who are more than friends but family members to me.

I am truly thankful to my parents Youshan Huang and Qingrong Zhou for their unconditional love and support. Special thanks to my husband Shenggang Wang who stood by me through the journey, giving me the love, help and encouragement. Without his supports, I could not possibly accomplish this. My thanks to my daughter, Carlina H. Wang, for bringing the joy, hope and courage to our family. I also would like to thank Zhaojun Wang, Xia Wang and Shengnan Wang for their caring and support.

## TABLE OF CONTENTS

LIST OF FIGURES .....	xii
LIST OF TABLES.....	xviii
LIST OF SCHEMES .....	xix
ABBREVIATIONS .....	xx
ABSTRACT .....	xxiii
CHAPTER 1. INTRODUCTION.....	1
1.1 Brain .....	1
1.2 Blood Brain Barrier .....	2
1.2.1 History and development of the BBB.....	2
1.2.2 Structural components of BBB .....	2
1.2.3 Function of the BBB.....	4
1.3 Transport pathways across the BBB .....	7
1.4 Challenges for drug development for CNS diseases.....	10
1.5 Strategies for drug delivery into CNS .....	11
1.5.1 Transcranial brain drug delivery .....	12
1.5.2 Disruption of BBB.....	13
1.5.3 Prodrug approach .....	15
1.5.4 Biological Delivery Systems.....	18
1.5.5 Intranasal drug delivery to the brain.....	25

1.5.6	Nanocarriers drug delivery to the brain .....	26
1.5.6.1	Passive targeting.....	27
1.5.6.2	Active targeting .....	28
1.6	GSH for brain targeting .....	31
CHAPTER 2 DESIGN, SYNTHESIS, AND EVALUATION OF CLG, COLG AND CNLG AS BRAIN TARGETING AGENTS .....		42
2.1	Introduction.....	42
2.2	Result and Discussion.....	44
2.2.1	Synthesis and characterization .....	44
2.2.1.1	Synthesis and characterization of CLG .....	44
2.2.1.2	Synthesis and characterization of COLG.....	47
2.2.1.3	Synthesis and characterization of CNLG.....	49
2.2.2	CMC determination .....	52
2.2.3	Preparation of DiR loaded Micelles .....	54
2.2.3.1	Preparation and characterization of DiR loaded micelles.....	54
2.2.3.2	Storage stability of DiR loaded micelles .....	57
2.2.3.3	Evaluation of brain-targeting effects through <i>ex-vivo</i> imaging of brain .....	59
2.2.4	Further investigation of CNLG for a brain targeting drug delivery system.....	60

2.2.4.1	<i>In vitro</i> cytotoxicity .....	60
2.2.4.2	Rhodamine B <i>in vitro</i> release study.....	61
2.2.4.3	Cellular uptake of Rhodamine B loaded CNLG micelles.....	62
2.2.4.4	Whole-body fluorescence imaging of mice .....	64
2.2.4.5	<i>Ex-vivo</i> fluorescence imaging .....	65
2.2.4.5.1	Brain <i>ex-vivo</i> imaging .....	66
2.2.4.5.2	<i>Ex-vivo</i> imaging of organs other than brain.....	66
2.2.5	Conclusion .....	68
2.3	Methods .....	69
2.3.1	Chemicals and materials .....	69
2.3.2	Instrumentation.....	70
2.3.3	HPLC/MS and LC/MS/MS condition .....	71
2.3.4	Cells and animals.....	72
2.3.5	Synthesis of COXP derivatives (CLG, COLG, CNLG) .....	72
2.3.5.1	Synthesis of CLG .....	72
2.3.5.2	Synthesis of COLG.....	74
2.3.5.3	Synthesis of CNLG.....	75
2.3.6	Purity determination .....	77
2.3.7	<i>In vitro</i> cell cytotoxicity.....	77
2.3.8	CMC determination .....	78

2.3.9	Preparation of DiR loaded micelles.....	78
2.3.10	Preparation of Rhodamine B loaded CNLG micelles .....	79
2.3.11	Characterization of DiR loaded micelles .....	79
2.3.12	Determination of DiR encapsulation efficiency and loading capacity .....	79
2.3.13	Storage stability of DiR loaded micelles .....	80
2.3.14	Rhodamine B <i>in vitro</i> release study.....	80
2.3.15	Cellular uptake of Rhodamine B .....	80
2.3.16	<i>In vivo</i> animal study.....	81
2.3.16.1	Whole-body fluorescence images of mice .....	81
2.3.16.2	<i>Ex-vivo</i> brain and organs imaging of mice.....	82
2.3.17	Statistics .....	82

CHAPTER 3	DESIGN, SYNTHESIS, AND EVALUATION OF OG AND OLG AS BRAIN TARGETING AGENTS .....	83
3.1	Introduction.....	83
3.2	Result and Discussion.....	85
3.2.1	Synthesis and characterization of OG.....	85
3.2.2	Synthesis and characterization of OLG .....	88
3.2.3	CMC determination .....	91
3.2.4	<i>In vitro</i> cytotoxicity .....	93

3.2.5	Rhodamine B <i>in vitro</i> release study.....	94
3.2.6	Cellular uptake of Rhodamine B .....	95
3.2.7	Preparation and characterization of DiR loaded micelles.....	97
3.2.8	Storage stability of DiR loaded micelles .....	98
3.2.9	Whole-body fluorescence images of mice.....	99
3.2.10	<i>Ex-vivo</i> fluorescence imaging .....	102
3.2.10.1	<i>Ex-vivo</i> imaging of brain.....	102
3.2.10.2	<i>Ex-vivo</i> imaging of major organs other than brain.....	104
3.2.11	Conclusion .....	106
3.3	Methods .....	108
3.3.1	Chemicals and materials .....	108
3.3.2	Instrumentation.....	108
3.3.3	HPLC/MS and LC/MS/MS condition .....	110
3.3.4	Cells and animals.....	111
3.3.5	Synthesis of OG or OLG.....	111
3.3.5.1	Synthesis of OG.....	111
3.3.5.2	Synthesis of OLG .....	112
3.3.6	Purity determination .....	114
3.3.7	<i>In vitro</i> cell cytotoxicity.....	114
3.3.8	CMC determination (use the same procedure I edited earlier) ...	115

3.3.9	Preparation of DiR loaded micelles.....	115
3.3.10	Preparation of Rhodamine B loaded micelles.....	116
3.3.11	Characterization of DiR loaded micelles.....	116
3.3.12	Determination of DiR encapsulation efficiency and loading capacity .....	116
3.3.13	Storage stability of DiR loaded micelles .....	117
3.3.14	Rhodamine B <i>in vitro</i> release study.....	117
3.3.15	Cellular uptake of Rhodamine B .....	117
3.3.16	<i>In vivo</i> animal study.....	118
3.3.16.1	Whole-body fluorescence images of mice .....	118
3.3.16.2	<i>Ex-vivo</i> brain and organs imaging of mice.....	119
3.3.17	Statistics .....	119
CHAPTER 4. CONCLUSION AND FUTURE PLAN.....		120
4.1	Conclusion .....	120
4.2	Future plan .....	124
CHAPTER 5. PHARMACOKINETIC CONSIDERATIONS IN THE DEVELOPMENT OF THERAPEUTICAL MONOCLONAL ANTIBODIES COMPARED WITH SMALL-MOLECULE DRUGS .....		126
5.1	Introduction.....	126
5.2	Route of Administration and Absorption of mAbs .....	127

5.3	Distribution of mAbs .....	128
5.4	Metabolism of mAbs .....	129
5.5	Elimination of mAbs .....	129
5.6	Conclusion .....	131
	References .....	131

## LIST OF FIGURES

Figure 1. Brian and brain region function.....	1
Figure 2. Structural components of BBB. Adapted from reference [11]......	3
Figure 3. Transport pathways across the BBB. Adapted from reference [43]. .....	8
Figure 4. Challenge in CNS drug development. Adapted from reference [57]. .	11
Figure 5. Strategies for drug delivery into CNS.....	12
Figure 6. Key in success of CNS prodrugs. Adapted from reference [75] .....	15
Figure 7. Illustration of the chemical drug delivery system (CDS). Adapted from reference [74].....	18
Figure 8. Blood–brain barrier Trojan horse technology. Adapted from reference [57].....	22
Figure 9. Chemical Structure of COXP.....	33
Figure 10. DiR loaded COXP micelles.....	34
Figure 11. Release of Rhodamine B from Rhodamine B loaded COXP micelles. Rhodamine B loaded COXP micelles (4.7µg rhodamine/mL, 0.5 mL) were dialyzed in a pre-swollen dialysis bag (molecule weight cut-off: 10 kDa) in a 40 mL PBS buffer with a stirring speed of 100 rpm. Aliquots (3 mL) were withdrawn at predetermined time (0, 0.25, 0.5, 1,2, 4, 6, 10, 24 h) for HPLC analysis of Rhodamine B. After each aliquot withdrawn, the same volume of the PBS buffer was added back to maintain the dialysis volume. A parallel dialysis in which a dialysis bag containing the same amount of free Rhodamine B was conducted for comparison.....	35
Figure 12. Results from the whole-body fluorescence imaging of mice after a single dose tail vein injection of free DiR (A: 5 µg DiR in 25 µL ethanol, control) and	

DiR loaded COXP micelles (C: 0.2 mL containing 5  $\mu$ g DiR). I: Representative images derived from in vivo whole-body fluorescence imaging. II: Brain fluorescence intensities from the whole-body imaging in I. Results are presented as mean  $\pm$  SD (n=3).  $P < 0.05$  \*;  $P < 0.01$  \*\*;  $P < 0.001$ \*\*\* .....37

Figure 13. Representative *ex-vivo* images (**I**) and corresponding fluorescence intensities (**II**) of the mouse brains 1 h after a single dose tail vein injection of free DiR (**A**: 5  $\mu$ g DiR in 25  $\mu$ L ethanol, control) and DiR-loaded COXP micelles (**B**: 0.2 mL containing 5  $\mu$ g DiR). *Data are presented as mean  $\pm$  SD (n = 3 for A, n = 4 for B).  $P < 0.05$  \** .....39

Figure 14. Cell uptake and uptake inhibition of COXP micelles by probenecid. Mouse kidney cells (2<sup>nd</sup> passage) were placed in a 96 well plates with a concentration of 5000 cells/well. When a 90% confluence was reached, cells were treated with medium only (no inhibitor) or probenecid (1 mM) for 30 min followed by replacement of the medium containing only Rhodamine B loaded COXP micelles (0.35 mg/mL) or Rhodamine B loaded COXP micelles (0.35 mg/mL) plus probenecid (1 mM), The cells were allowed to incubate at 37  $^{\circ}$ C for an additional 30 min before removal of the medium and measured for fluorescence intensity with a microplate reader ( $\lambda_{ex}$  540 nm,  $\lambda_{em}$  625 nm). *The data are expressed as a percentage of control (COXP group). (n = 3,  $P < 0.05$ \*,  $P < 0.01$ \*\* , Student's t-test).....40*

Figure 15. Chemical structure of COXP and COXP derivatives (**A**: CLG; **B**: COLG; **C**: CNLG).....43

Figure 16. HRMS spectrum of CLG.....45

Figure 17. <i>S</i> -isomer ( <b>A</b> ) and <i>N</i> -isomer ( <b>B</b> ) of GSH analog generated from Michael addition with GSH and their expected MS fragmentation pattern. ....	46
Figure 18. LC/MS/MS spectrum of CLG .....	47
Figure 19. HRMS spectrum of COLG.....	48
Figure 20. LC/MS/MS spectrum of COLG .....	49
Figure 21. HRMS spectrum of CNLG.....	51
Figure 22. LC/MS/MS spectrum of CNLG .....	51
Figure 23. Determination of CMC of ( <b>A</b> ) CLG micelles; ( <b>B</b> ) COLG micelles; ( <b>C</b> ) CNLG micelles. ....	53
Figure 24. Preparation of DiR loaded micelles .....	54
Figure 25. Stability of ( <b>A</b> ) DiR loaded CLG micelles; ( <b>B</b> ) DiR loaded COLG micelles; ( <b>C</b> ) DiR loaded CNLG micelles during 7 days' storage at 4°C. <i>Data are presented as mean ± SD (n=3)</i> .....	58
Figure 26. Representative <i>ex-vivo</i> images ( <b>I</b> ) and corresponding fluorescence intensities ( <b>II</b> ) of the mouse brains 2 h after i.v injection of Free DiR (n=1); CLG DiR micelle (n=1); COLG DiR micelle (n=1); CNLG DiR micelles (n=1) .....	59
Figure 27. Dose-response curves for the determination of IC <sub>50</sub> values of CNLG with ( <b>A</b> ) CV-1 cell line, ( <b>B</b> ) NCI-H226 cell line. ....	61
Figure 28. Release of Rhodamine B from Rhodamine B loaded CNLG micelles with Rhodamine B ethanol solution as a control in PBS buffer (pH 7.4) or citric acid buffer (pH 4.5). <i>Data are presented as mean ± SD (n=3)</i> .....	62

Figure 29. Cell uptake and uptake inhibition by probenecid of Rhodamine B loaded CNLG micelles in mouse kidney cells. <i>The data are expressed as a percentage of control (n = 3, P &lt; 0.01**, Student's t-test).</i> .....	63
Figure 30. Whole-body fluorescence imaging of mice after i.v injection of free DiR (A) and DiR loaded CNLG micelles (B).....	64
Figure 31. Brain fluorescence intensities from the whole-body imaging. <i>Results are presented as mean ± SD (n=3). P &lt; 0.01 **; P &lt; 0.001***</i> .....	65
Figure 32. Representative ex-vivo images (I) and corresponding fluorescence intensities (II) of the mouse brains 2 h after i.v injection of free DiR (A), DiR loaded CNLG micelles (B). <i>Results are presented as mean ± SD (n=3). P &lt; 0.01**</i> .....	67
Figure 33. Representative <i>ex-vivo</i> images (I) and corresponding fluorescence intensities (II) of the organs 2 h after i.v injection of free DiR (A) or DiR loaded CNLG micelles (B). <i>Results are presented as mean ± SD (n=3).</i> .....	68
Figure 34. Chemical structure of COXP, Stearyl alcohol, OG and OLG .....	85
Figure 35. HRMS spectrum of OG.....	87
Figure 36. LC/MS/MS spectrum of OG. ....	88
Figure 37. HRMS spectrum of OLG .....	90
Figure 38. LC/MS/MS spectrum of OLG .....	90
Figure 39. Determination of CMC of (A)OG micelles; (B) COLG micelles .....	92
Figure 40. Dose-response curves for the determination of IC <sub>50</sub> values of OG with (A) CV-1 cell line (B) NCI-H226 cell line. ....	93
Figure 41. Dose-response curves for the determination of IC <sub>50</sub> values of OLG with (A) CV-1 cell line (B) NCI-H226 cell line. ....	94

Figure 42. Release of Rhodamine B from (A) Rhodamine B loaded OG micelles and (B) Rhodamine B loaded OLG micelles with a comparison to the Rhodamine B ethanol solution in a pH 7.4 PBS buffer. *Data are presented as mean  $\pm$  SD (n=3).* .....95

Figure 43. Cell uptake inhibition of (A) OG micelles and (B) OLG micelles by probenecid. *Data are presented as mean  $\pm$  SD (n=3).  $P < 0.05$  \**.....96

Figure 44. Stability of (A) DiR loaded OG micelles; (B) DiR loaded OLG storage at 4°C. *Data are presented as mean  $\pm$  SD (n=3).* .....99

Figure 45. Representative whole-body fluorescence imaging (I) and corresponding fluorescence intensities (II) of the brains 2h after i.v injection of free DiR (A) or DiR loaded OG micelles (B). *Results are presented as mean  $\pm$  SD (n=3).  $P < 0.01$  \*\*  $P < 0.001$  \*\*\**..... 100

Figure 46. Representative whole-body fluorescence imaging (I) and corresponding fluorescence intensities (II) of the mouse brains after i.v injection of free DiR (A), DiR loaded OLG micelles (B). *Results are presented as mean  $\pm$  SD (n=3).  $P < 0.01$  \*\*  $P < 0.001$  \*\*\** ..... 102

Figure 47. Representative *ex-vivo* images (I) and corresponding fluorescence intensities (II) of the mouse brains 2 h after a single dose tail vein injection of (A) free DiR and (B) DiR loaded OG micelles. *Results are presented as mean  $\pm$  SD (n=3).  $P < 0.05$  \** ..... 103

Figure 48. Representative *ex-vivo* images (I) and corresponding fluorescence intensities (II) of the mouse brains 2 h after a single dose tail vein injection of (A) free DiR and (B) DiR loaded OLG micelles. *Results are presented as mean  $\pm$  SD (n=3).  $P < 0.01$  \*\** ..... 103

Figure 49. Representative <i>ex-vivo</i> images ( <b>I</b> ) and corresponding fluorescence intensities ( <b>II</b> ) of the organs 2 h after i.v. injection of ( <b>A</b> ) free DiR and ( <b>B</b> ) DiR loaded OG micelles. <i>Results are presented as mean <math>\pm</math> SD (n=3).</i> .....	105
Figure 50. Representative <i>ex-vivo</i> images ( <b>I</b> ) and corresponding fluorescence intensities ( <b>II</b> ) of the organs 2 h after i.v. injection of ( <b>A</b> ) free DiR and ( <b>B</b> ) DiR loaded OLG micelles. <i>Results are presented as mean <math>\pm</math> SD (n=3).</i> .....	106
Figure 51. Development of antibody therapeutics and their applications. Adapted from Ref [210].....	126
Figure 52. Convective extravasation as a major distribution process for monoclonal antibodies. Adapted from Ref [211]. .....	128
Figure 53. FcRn - mediated recycling protection mechanism of IgG. Adapted from Ref [212].....	130

## LIST OF TABLES

Table 1 Carrier-mediated transporters present at the BBB and their transported molecules. ....	21
Table 2 Receptor-mediated transporters present at the BBB and their transported molecules. ....	23
Table 3 Active efflux transporters present at the BBB and their drug substrates. ....	25
Table 4 Current nanoparticle platforms and its features .....	26
Table 5 Other ligands studied for NPs to cross the BBB .....	30
Table 6 Characterization of DiR loaded micelles.....	56
Table 7 Characterization of DiR loaded micelles.....	98

## LIST OF SCHEMES

Scheme 1 Synthesis of CLG .....	44
Scheme 2 Synthesis of COLG.....	48
Scheme 3 Synthesis of CNLG.....	50
Scheme 4 Synthesis of OG.....	86
Scheme 5 Synthesis of OLG .....	89

## ABBREVIATIONS

CNS	Central nervous system
BBB	Blood-brain barrier
P-gp	P-glycoprotein
GSH	Glutathione
COXP	2-(2-cholesteroxyethoxyl) ethyl 3'-S-glutathionylpropionate
CMC	Critical micelle concentration
DiR	1,1'-dioctadecyl-3,3,3',3'-tetramethylindo-tricarbocyanine iodide
CLG	N5-(1-((carboxymethyl)amino)-3-((3-((10,13-dimethyl-17-(6-methylheptan-2-yl)-2,3,4,7,8,9,10,11,12,13,14,15,16,17-tetradecahydro-1H-cyclopenta[a]phenanthren-3-yl) oxy)-3-oxopropyl) thiol)-1-oxopropan-2-yl)glutamine
COLG	19-amino-14-((carboxymethyl)carbamoyl)-1-((10,13-dimethyl-17-(6-methylheptan-2-yl)-2,3,4,7,8,9,10,11,12,13,14,15,16,17-tetradecahydro-1H-cyclopenta[a]phenanthren-3-yl) oxy)-1,9,16-trioxo-2,5,8-trioxa-12-thia-15-azaicosan-20-oic acid
CNLG	16-amino-11-((carboxymethyl)carbamoyl)-1-((10,13-dimethyl-17-(6-methylheptan-2-yl)-2,3,4,7,8,9,10,11,12,13,14,15,16,17-tetradecahydro-1H-cyclopenta[a]phenanthren-3-yl) oxy)-1,6,13-trioxo-9-thia-2,5,12-triazaheptadecan-17-oic acid
OG	N5-(1-((carboxymethyl)amino)-3-((3-(octadecyloxy)-3-oxopropyl) thio)-1-oxopropan-2-yl)glutamine
OLG	2-amino-7-((carboxymethyl)carbamoyl)-5,12-dioxo-13, 16,19- trioxa-9-thia-6-azaheptatriacontanoic acid
CSF	Cerebrospinal fluid
CMT	Carrier-mediated transport
RMT	Receptor-mediated transport

AMT	Adsorptive-mediated transport
ABC transporter	Adenosine triphosphate-binding cassette transporter
MDR	Multidrug resistance receptor
BCRP	Breast cancer resistance receptor
IC implantation	Intracerebral implantation
ICV infusion	Intracerebroventricular infusion
CED	Convection enhanced diffusion
IgG	Immunoglobulin G
CPP	Cell penetrating peptide
TAT	Trans-activating transcription factor
LAT1	Large neutral amino acid transporter
GLUT1	Glucose transporter
TfR	Transferrin receptor
mAbs	Monoclonal antibodies
EPR	Enhanced permeability and retention
NP	Nanoparticle
RES	Reticuloendothelial system
FA	Folic acid
FaR	Folate receptor
Lf	Lactoferrin
LfR	Lactoferrin receptor
InR	Insulin receptor
TMC	Trimethylated chitosan

EGF	Epidermal growth factor
EGFR	Epidermal growth factor receptor
SPIO	Superparamagnetic iron oxide

ABSTRACT

DESIGN, SYNTHESIS, AND EVALUATION OF GLUTATHIONE DERIVATES AS  
BRAIN TARGETING AGENTS

YUE HUANG

2021

Treatment of central nervous system (CNS) diseases, such as Alzheimer's disease, Parkinson's diseases, and brain tumors, is still a challenge due to the existence of the blood-brain barrier (BBB). The BBB as a membrane barrier that separates systemic blood circulation from the CNS is structurally formed by endothelial cells, astrocyte, pericyte and neurons and is one of the crucial protection mechanisms for the CNS. The BBB protects the brain by preventing foreign compounds (non-endogenous compounds) from entering the brain and helps maintain brain homeostasis. In addition, the presence of drug efflux pumps (i.e., P-glycoproteins, multidrug-resistance proteins) in the BBB helps pump some of foreign compounds out of the brain. Because of the BBB, a drug molecule usually exists in the CNS in low concentration. Difficulty in achieving its therapeutic concentration caused by the BBB is often the major cause for a drug to fail to treat a CNS disease.

To cross the BBB and deliver a drug to the brain, various strategies have been attempted. These strategies can be mainly divided into two categories: invasive approaches (i.e., neurosurgical or disruption of BBB) and noninvasive approaches. A nanocarrier drug-delivery system with a brain targeting agent is an effective noninvasive approach to cross the BBB and deliver a drug to the brain.

Although the BBB prevents foreign compounds from entering the CNS, endogenous compounds such as glucose, amino acids, neurotransmitters, and glutathione (GSH) are able to enter the CNS through their corresponding transporters or receptors present at the BBB. The ligand or ligand analogue of these transporters or receptors have been employed to develop brain targeting agents to help deliver drug to the brain.

GSH is a tripeptide serving as a major molecule in the body to protect cells from oxidative stress and reactive toxic species. GSH is a hydrophilic and cell membrane impermeable molecule. As an endogenous molecule, GSH crosses the BBB and reaches the brain through a Na<sup>+</sup>-dependent GSH transporter. Thanks to the overexpression of GSH transporters in the BBB, successes have been made by using GSH to develop brain targeting agents or brain targeting drug delivery systems to facilitate drug entry to the brain.

In our previous work, we have successfully designed and synthesized 2-(2-cholesteroxyethoxyl) ethyl 3'-S-glutathionylpropionate (COXP) by connecting the hydrophilic GSH molecule with a hydrophobic cholesterol through a two-ethylene glycol unit linker. COXP is an amphiphilic molecule and can self-assemble to form micelles with a CMC value of 3.9 μM. The low μM of CMC suggests that COXP micelle is stable enough when diluted in the blood circulation after administration and has a potential for clinical applications as a drug delivery system. Micelle is one of the major nanocarrier drug delivery systems. The COXP micelle is featured with GSH molecules on the micelle surface to serve as a ligand for the GSH transporter recognition for brain targeting. Using 1,1'-dioctadecyl-3,3',3',3'-tetramethylindolyl-tricarbo-cyanine iodide (DiR), a near IR fluorescent and hydrophobic dye, as a fluorescence tracker and the whole-body

fluorescent imaging technique with mice, our previous data showed that COXP micelles increased the delivery of DiR to the brain by ~20 folds when compared with free DiR. The work not only provides a proof of concept that COXP micelle is an effective brain drug delivery system but also validates our strategy of using GSH as a brain targeting ligand for designing a novel brain targeting molecule.

The aim of this dissertation was to identify more effective brain targeting agents and brain-targeting drug delivery systems by conducting structural modification of COXP. The structural modification mainly involved two parts of the COXP structure: i). replacement of the linker between GSH and cholesterol; ii). replacement of the hydrophobic cholesterol structure with a hydrophobic fatty alcohol. All designed compounds are amphiphilic molecules and expected to form micelles.

Chapter 2 describes the structural modification through a replacement of the linker between GSH and cholesterol. Three compounds were designed with three different linkers: i) N5-(1-((carboxymethyl)amino)-3-((3-((10,13-dimethyl-17-(6-methylheptan-2-yl)-2,3,4,7,8,9,10,11,12,13,14,15,16,17-tetradecahydro-1H-cyclopenta[a]phenanthren-3-yl)-oxy)-3-oxopropyl)thiol)-1-oxopropan-2-yl)glutamine (CLG); ii) 19-amino-14-((carboxymethyl)carbamoyl)-1-((10,13-dimethyl-17-(6-methylheptan-2-yl)-2,3,4,7,8,9,10,11,12,13,14,15,16,17-tetradecahydro-1H-cyclopenta[a]phenanthren-3-yl)-oxy)-1,9,16-trioxo-2,5,8-trioxa-12-thia-15-azaicosan-20-oic acid (COLG); iii) 16-amino-11-((carboxymethyl)carbamoyl)-1-((10,13-dimethyl-17-(6-methylheptan-2-yl)-2,3,4,7,8,9,10,11,12,13,14,15,16,17-tetradecahydro-1H-cyclopenta[a]phenanthren-3-yl)-oxy)-1,6,13-trioxo-9-thia-2,5,12-triazaheptadecan-17-oic acid (CNLG). All three were able to form a micelle with a CMC value of 1.34  $\mu$ M, 5.70  $\mu$ M, and 6.01  $\mu$ M for CLG, COLG, and CNLG, respectively. A preliminary ex-vivo work with mice using DiR as a fluorescence

tracking agent showed that the micelles from these three compounds were all effective brain-targeting micelles with CNLG micelles being the most effective brain targeting micelles. Results from the whole-body imaging showed that CNLG micelles delivered DiR to the brain 40 folds higher when compared with free DiR, significantly higher than COXP micelles.

Chapter 3 describes the structural modification through a replacement of the cholesterol structure with a fatty alcohol. Two compounds were designed: i) N<sup>5</sup>-(1-((carboxymethyl)amino)-3-((3-(octadecyloxy)-3-oxopropyl) thio)-1-oxopropan-2-yl)glutamine (OG); ii) 2-amino-7-((carboxymethyl)carbonyl)-5,12-dioxo-13, 16,19- trioxa-9-thia-6-azaheptatriacontanoic acid (OLG). Both OG and OLG were able to form micelles with a CMC value of 12.48  $\mu$ M for OG and 2.0  $\mu$ M for OLG, respectively. Both micelles were brain targeting micelles. The OG micelles increased the delivery of DiR to the brain by 63 folds at 2 h compared with free DiR. The OLG micelles were even better and increased the delivery of DiR to the brain by 98.3 folds at 30 min compared with free DiR. Both OG micelles and OLG micelles delivered DiR to the brain substantially higher than COXP micelles.

In conclusion, we have successfully developed five GSH derivatives as a brain targeting agents based on the structural modification of COXP. The results from this dissertation further validate the use of GSH as an effective ligand for the development of novel brain targeting agents. The results also confirm that a change of the linker and replacement of the cholesterol with a hydrophobic alcohol are valid structural modifications and can lead to more effective brain targeting agents and brain targeting micelles.

## CHAPTER 1. INTRODUCTION

### 1.1 Brain

The human brain is one of the most important organs in the body and also the most complex organ consisting primarily of cerebrum, brainstem, and cerebellum (Figure 1). The brain is encased in the skull with cerebrospinal fluid (CSF) circulating around and is separated from the peripheral bloodstream by two principal protective barriers: blood–brain barrier (BBB) and blood-CSF barrier (BCSFB)[1]. The BBB is a physical barrier that separates the brain tissue and the blood while the blood-CSF barrier is a functional barrier that separates the cerebrospinal fluid and blood. Besides, the brain is one of major structures of central nervous system (CNS) which plays a critical role in the regulation of the body function that includes motor control, cognition, sensory, speech and memory [2].

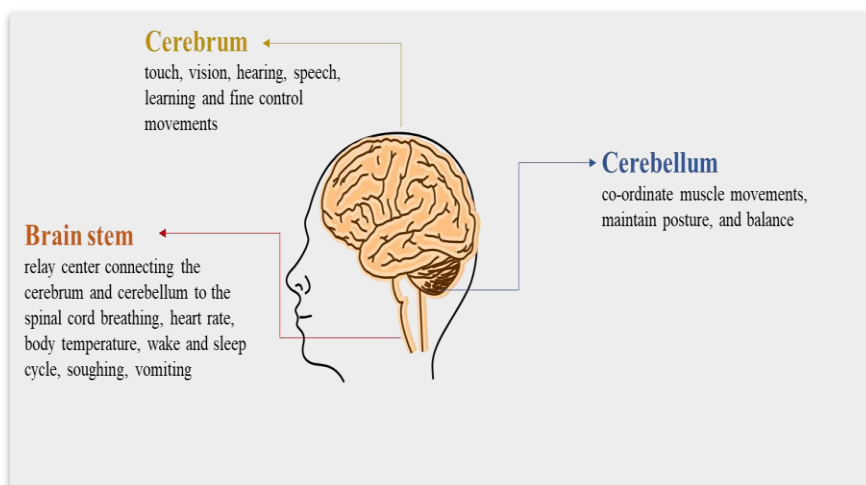


Figure 1. Brian and brain region function

## **1.2 Blood Brain Barrier**

### **1.2.1 History and development of the BBB**

The BBB was first described by Paul Ehrlich when he found that the dye he injected into blood only stained the peripheral organs but not the brain[3]. In a later time, Ehrlich's student Edwin Goldman injected trypan blue directly into CSF and found that the brain became stained but not the periphery, indicating the existence of a barrier between the CNS and peripheral vessels[4]. In the early 1960's, Reese and Karnovsky demonstrated through electron microscopic cytochemical studies that it was the tight junctions between endothelial cells that comprise the BBB instead of the astrocyte end-feet [5, 6].

The BBB appears to be formed by the time of birth and matures during fetal life[7] according to the report that the existence of a barrier of trypan blue from at least the beginning of second trimester and this barrier was similar with that of adult human[8].

### **1.2.2 Structural components of BBB**

The BBB is a highly selective barrier between blood and brain, which is formed by endothelial cells of the capillary wall, astrocyte end-feet, and pericytes [1, 9]. Additionally, the neurovascular unit that is made up by microglial cells and neurons is also closely associated with the endothelium and works altogether to support BBB induction, maintenance, and function by cell-cell interactions (Figure 2)[1, 10]

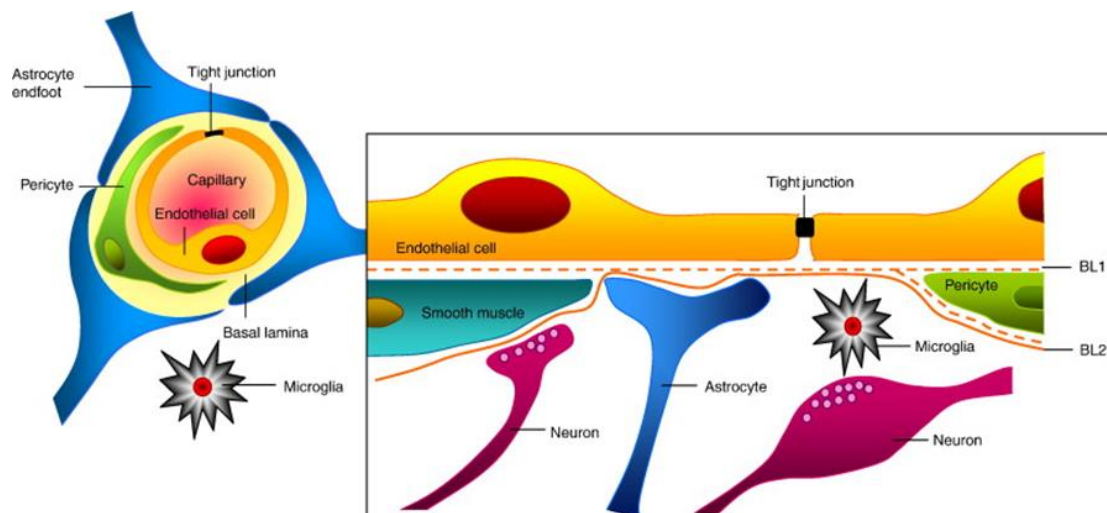


Figure 2. Structural components of BBB. Adapted from reference [11].

### *Endothelial cells*

Endothelial cells, located at the interface between the blood and the brain, are characterized by the unique phenotype of tight junctions. Similar to epithelial tight junctions, tight junctions between brain endothelial cells are also composed of transmembrane proteins (occludin, claudins and junctional adhesion molecules) with a much tighter nature (around 50-100 times) than that found between epithelial cells in peripheral microvessels [10]. Due to this property, the BBB selectively prevents most hydrophilic molecules from entering the brain. The expression of specific transport systems in endothelial cells is another feature of the BBB. In particular, drug efflux pumps such as P-glycoprotein (P-gp) and multidrug-resistance protein (MDR) that are present mainly on the luminal membrane surface play a critical role in restricting the passage of hydrophobic molecules into brain[12, 13].

### *Pericytes*

Pericytes are flat, undifferentiated, contractile connective tissue cells that are embedded in the vascular basement membrane. It has been suggested that the association of pericytes to blood vessels could regulate the proliferation, survival, migration, and differentiation of endothelial cells as well as vascular branching[14]. Furthermore, studies also show evidence to support the hypothesis that pericytes play an important role in the induction of polarization of astrocyte end-feet around brain microvessels to maintain the integrity of the BBB structure[15-17].

### *Astrocytes*

Astrocytes are glial cells that envelop >99% of the BBB endothelium[18]. Astrocytes interact with pericytes and endothelial cells by end-feet ensheathing the capillary vessels. This interaction not only greatly enhances the tight junction of endothelial cell but also increases the number of astrocytic membrane particle assemblies as well as the density of astrocyte[11, 19]. Coculture of brain endothelial cells with astrocytes *in vitro* suggests that astrocytes are essential in the maintenance of BBB tightness and function[19-21]. Moreover, astrocytes are also essential for proper neuronal function[22].

## **1.2.3 Function of the BBB**

### *Neuronal and vascular function*

Although the human brain accounts for only ~2% of the total body mass, it consumes more than 20% of total body oxygen and energy [23]. The integrated system of neuronal and vascular cells serves to maintain brain homeostasis by providing the energy

demands to neuronal activity via blood flow[24], but the exact mechanism of the intact BBB in regulation between neuronal activity and blood flow remains unknown. Studies showed that BBB disruption occurring in pathological conditions (ischemia, hemorrhage, or traumatic injury) could decrease cerebral blood flow that is likely to result in impaired neurovascular function[25, 26].

### *Neurotoxins*

The regenerative capacity of adult CNS is relatively weak if it has been damaged. It is not easy for fully differentiated neurons to divide and replace themselves under normal circumstances. It has also been stated that the neuronal cell death in a healthy human brain is at a continuous steady rate from birth throughout life while neurogenesis is at a relative low rate [27]. Therefore, an increased access of neurotoxins, either endogenous metabolites or xenobiotics, into the brain could stimulate the rate of cell death, thus resulting in premature impairment in brain. The BBB thereby serves as a protective barrier to protect CNS from neurotoxic substances that circulated in the bloodstream by reducing their entry and/or pumping them out of the brain actively through efflux pumps.

### *Neurotransmitters*

The amino acid L-glutamate is an excitatory neurotransmitter in the CNS. The increased brain interstitial fluid concentration of L-glutamate could result in excitotoxicity to neural tissues. However, during ischemic stroke where the homeostasis of L-glutamate cannot be maintained. Therefore, it is important to maintain optimal

amount of neurotransmission to avoid such excitotoxicity. The BBB protects the nerve cells from such variation and maintain the homeostasis of L-glutamate [27, 28].

### *Ion regulation*

In addition to providing a homeostatic environment for normal neural function, the BBB also maintains a constant concentration of ions for synaptic signaling function by specific ion channels and transporters. For example, the concentration of potassium in plasma is at ~3.5–5.0 mM. However, plasma potassium concentration may increase to the level as high as 10 mM during exercise or a meal or under pathological conditions[29-31]. Despite these variation in potassium concentration in blood, potassium concentration in the CNS is maintained at ~2.5–2.9 mM since the BBB can regulate the movement of ions. Similarly, other ions such as  $\text{Ca}^{2+}$  and  $\text{Mg}^{2+}$  are also regulated by the BBB actively due to the impermeability of the BBB to most ions[32-34].

### *Protein synthesis and regulation*

Essential amino acids are always needed for protein synthesis in the brain, but they are incapable of diffusion into the brain due to their high hydrophilicity. Therefore, specific transporter proteins are expressed in the BBB to transport amino acids into the brain to meet the needs of the CNS [35-37]. Moreover, the typical plasma protein concentrations are higher than that in CSF largely because of the ability of the BBB to prevent such macromolecules from entering the brain. It has been reported that serum proteins, such as thrombin, plasmin, and albumin are harmful to nervous tissue by triggering cellular activation, inflammation, and apoptosis[38-40]. Thus, the

extravasation of these serum proteins from plasma into the brain could result in serious pathological outcomes[41, 42].

### **1.3 Transport pathways across the BBB**

There are various mechanisms for molecules to pass through the BBB. The paracellular aqueous pathway for water soluble small molecule (Figure 3 a) and transcellular lipophilic pathway for lipid soluble (hydrophobic) molecules (Figure 3 b), the two most common mechanisms for drug molecules to pass through cell membrane, still operate for molecules to pass through the BBB though these two mechanisms are greatly impacted and restricted by the structure and function of the BBB. In addition to these two mechanisms, specific transport mechanisms such as transporter proteins (Figure 3 c), efflux pumps (Figure 3 d), receptor-mediated transport (Figure 3 e), adsorptive transport (Figure 3 f), and cell-mediated transport (Figure 3 g), play significant roles in transporting various molecules through the BBB to reach the brain. Since these pathways are relevant to brain targeting, a detailed discussion for each pathway will be discussed below.

#### *Paracellular Transport*

The paracellular pathway occurs through the junctional complex between endothelial cells and is concentration gradient-driven diffusion. Since the junction is aqueous in nature with limited space, only small water-soluble molecule are allowed to pass with a limited capacity. Although this is one of the primary transport routes, it plays a minor role for molecules to cross the BBB.

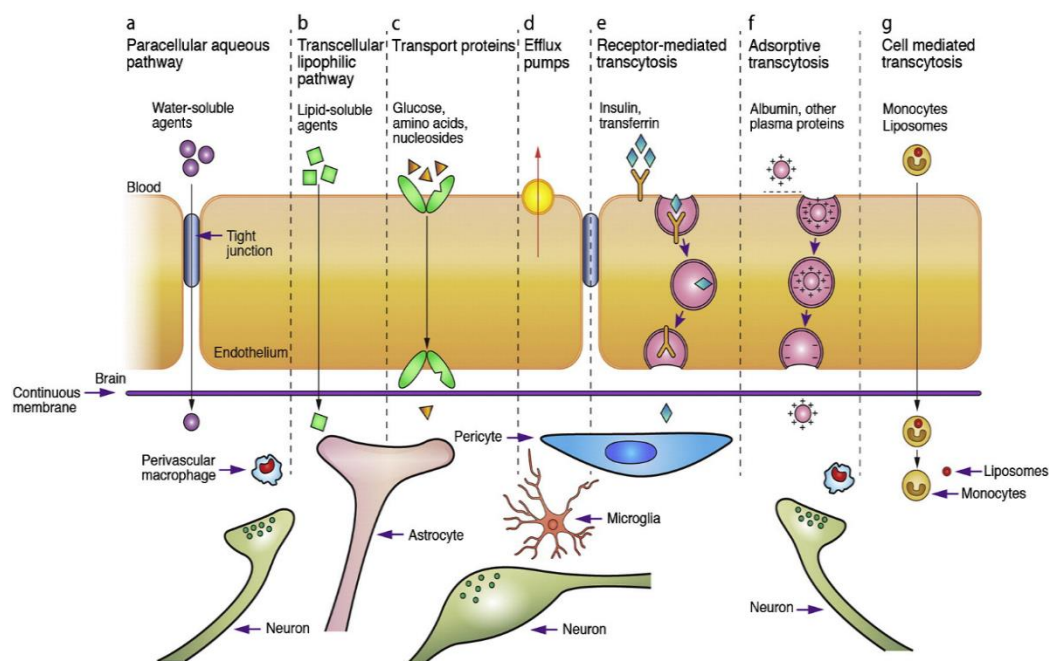


Figure 3. Transport pathways across the BBB. Adapted from reference [43].

### *Transcellular Transport*

The transcellular pathway is for molecules to move across either the luminal membrane or the abluminal membrane of the brain capillary endothelial cells[44] and is also a concentration gradient-driven diffusion. As a result of the lipophilic nature of cell membrane, the higher the lipophilicity of the compounds, the greater the diffusion. However, the limitation of this pathway lies in the lipophilicity of compounds, since lipophilic compounds can be a good substrate for P-glycoprotein (P-gp) drug efflux pump, meaning that although these compounds have the ability to cross the BBB, they also bear a risk of being pumped out from the brain back into blood by P-gp.

### *Transporter-mediated transport*

Transporter-mediated transport, also known as carrier-mediated transport (CMT), is a form of pathway that mediates the exchange of molecules between blood and brain through their corresponding transporters expressed both in the luminal membrane and abluminal membrane of the BBB[45]. These transporters are generally polarized proteins and the pathway they mediate is a saturable process and can be either energy-dependent or energy-independent. Small endogenous molecules such as glucose, amino acids, nucleosides, and GSH can be transported by their corresponding transporters [46-48].

### *Receptor-Mediated transport*

Receptor-mediated transport (RMT) provides a mean for brains to take up large needed endogenous molecules. These macromolecules such as hormones, growth factors, insulin, and transferrin enter the brain by binding with their specific receptors present in the BBB[49, 50]. This transport route is energy-dependent and saturable owing to the limited number of receptors existed on the cell surface.

### *Efflux Transport*

As mentioned before, the efflux transport system is another feature of brain endothelial cell that contribute to the protection of the brain from harmful substances by actively removing harmful substances from the brain into the systemic circulation. This pathway is both energy and concentration dependent. In addition to P-gp, a key element of glycosylated member of ABC transporter (adenosine triphosphate-binding cassette) present at the luminal membrane of brain endothelial cells, other well-known ABC efflux

transporters are **multidrug resistance receptors (MDRs) and breast cancer resistance receptors (BCRPs)** that function on the luminal membrane of brain endothelial cells[51, 52].

#### *Absorptive-mediated transport*

Generally, adsorptive-mediated transport (AMT) facilitates cationic compounds to pass the BBB through the nonspecific electrostatic interaction with the negatively charged cell membrane[53]. Compared with CMT, AMT has a low affinity but high capacity.

#### *Cell-mediated transport*

Cell-mediated transport is an established mechanism for some pathogens to cross the intact BBB [54, 55]. This transport route works through immune cells such as monocytes and macrophages. The uniqueness of cell-mediated transport is that it can be applied for any type of molecules as well as particulate carrier systems [56].

### **1.4 Challenges for drug development for CNS diseases**

Frequent challenge with new drug candidates, regarding CNS delivery, is the high polarity of candidates. Based on the aforementioned features of the BBB, an ideal new drug candidate for CNS diseases should have the following physicochemical properties: molecular weight <400 Da and a certain degree of lipophilicity but not a good substrate for an active efflux transporter. However, as demonstrated in Figure 4, the majority of new drug molecules, including >98% of small molecule drugs and nearly all large molecule drugs, lack the above mentioned features that are essential for crossing the BBB to enter into brain[57].

Besides crossing the BBB, other problems also exist for brain drug development. First, even if a drug can cross the BBB, it may not reach its relevant therapeutic concentration in the brain since only a small amount of drug was allowed to pass the BBB under the current approaches. Other possible reasons can be attributed to binding of a drug molecule with proteins making the drug either be less therapeutically active or reducing its ability to cross the BBB [58]. Another problem lies in the inactivation of a drug by enzymes in the brain. Therefore, it is a challenge to develop a drug candidate for the treatment of CNS diseases (i.e., Alzheimer's disease, Parkinson's disease, multiple sclerosis, stroke, brain cancer) [58-60].

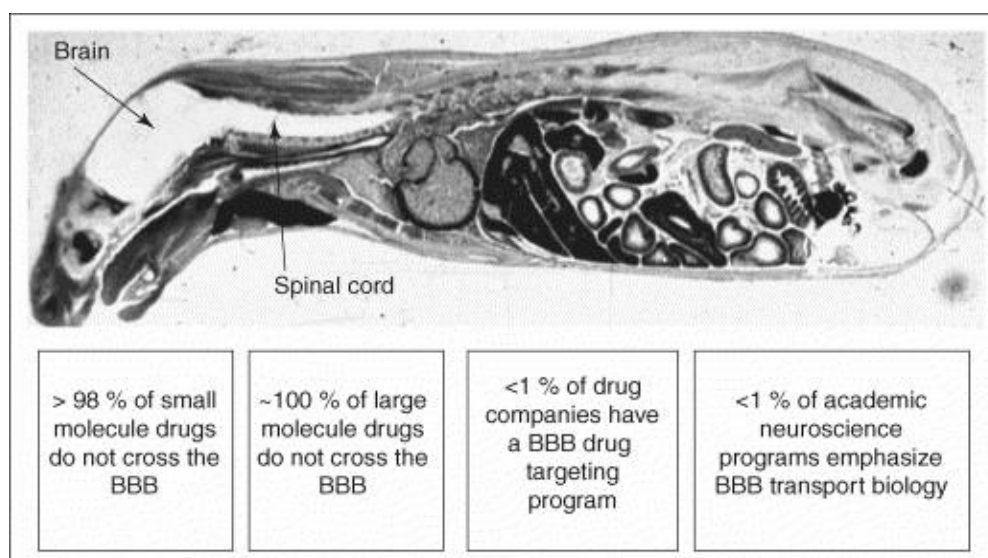


Figure 4. Challenge in CNS drug development. Adapted from reference [57].

### 1.5 Strategies for drug delivery into CNS

Multiple strategies have been reported to overcome the problem of delivering drugs into the CNS. These strategies can fall into six categories: (1) neurosurgical-based approach, direct local drug infusion approach; (2) BBB disruption approach, which attempts to disrupt the junctional complexes and increase drug uptake in CNS; (3)

chemistry-based approach, which usually refers to chemical modification of a drug in order to increase the lipophilicity of the drug; (4) biology-based approach, which involves reformulation of a drug to access endogenous BBB transporters; (5) intranasal drug delivery approach, an alternative method to deliver drug from nose to the brain; and (6) using a nanocarrier drug delivery system (DDSs), an innovative strategy that takes advantage of nanotechnology. Among these strategies, approaches 1 and 2 are invasive while the others are non-invasive (Figure 5).

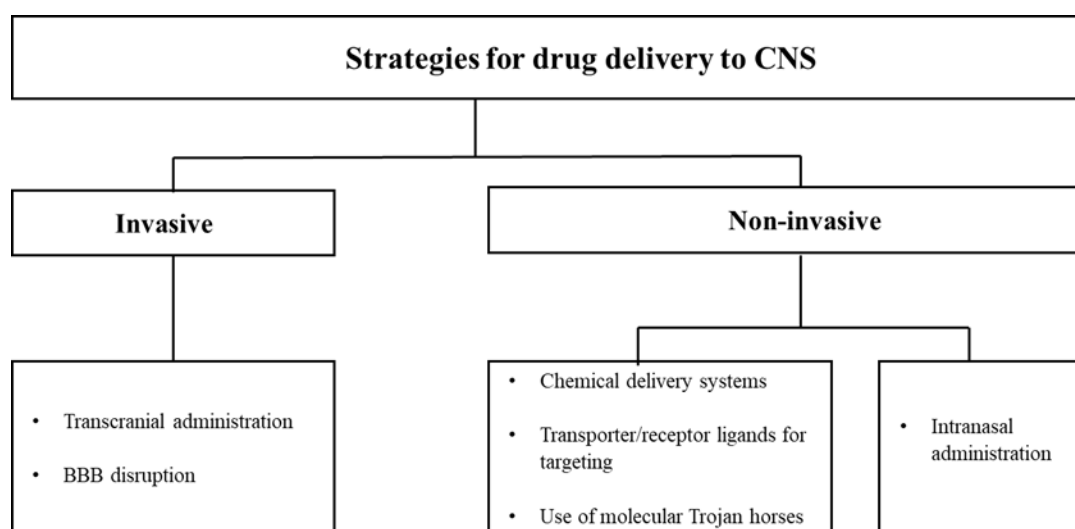


Figure 5. Strategies for drug delivery into CNS.

### 1.5.1 Transcranial brain drug delivery

Transcranial brain drug delivery is a typical neurosurgical-based strategy to bypass the BBB. It includes intracerebral (IC) implantation, intracerebroventricular (ICV) infusion, and convection enhanced diffusion (CED).

Drug delivered to the brain through either IC implantation or ICV infusion does not move into the brain from the injection site significantly and the diffusion of drug decreases exponentially with the diffusion distance. Therefore, drug concentration

decreases from the injection site with IC implantation or from the ependymal surface with ICV infusion[59, 60]. Drug delivered through CED is triggered by convection, but the limitation of this convention approach results from the fact that the brain is the only organ that has no lymphatic system, and it is not aimed at clearing off a large volume of fluid. Moreover, fluid from CED device enters the brain prefers to move along white matter tracts [61, 62].

### **1.5.2 Disruption of BBB**

The goal of BBB modification is to disrupt the junctional complexes to increase drug delivery into brain. Four methods, namely osmotic, biochemical, alkylglycerols and ultrasound, are accessible to open parts of the BBB in a transit and reversible way, which can avoid an extended opening of the barrier. However, the potential risk of this approach is associated with a diminished control of drug as well as an increased access of potentially toxic molecules.

#### *Osmotic Disruption of the BBB*

It is carried out by the infusion of a hyperosmotic solution into brain. Due to the osmotic pressure, brain endothelial cells would shrink under a hypertonic environment resulting in small holes at the tight junction to allow a drug molecule to cross the BBB [63]. The commonly used hyperosmolar agents are saccharide solutions and mannitol [64, 65]. However, infusion of hyperosmotic agents into brain may lead to chronic neuronal damage and vasculopathy in brain[66].

### *Biochemical Disruption of the BBB*

Vasoactive agents such as histamine, bradykinin, and other compounds such as solvents (i.e., high dose ethanol, DMSO, SDS, Tween 80), or immune adjuvants (i.e., Freuds) could disrupt the tight junctions between brain endothelial cells and increases the permeability of the brain resulting in BBB opening[67-69]. Studies show that these agents work through a biochemical change by phosphorylation/dephosphorylation of the junctional complex proteins to weaken the cell-cell junction thus facilitating the access of drug by the paracellular pathway [70, 71].

### *BBB Disruption by Alkylglycerols*

It has been reported that administration of alkylglycerols could increase the uptake of drug to the site with glioma tumors, compared with hyperosmotic shock and biochemical disruption [72]. Although the mechanism is not clear, a possible explanation is the interaction between alkylglycerols and the receptor present in brain endothelium since BBB disruption is both concentration and structure dependent which is similar with a typical receptor-ligand response. Studies also showed that the length of alkyl group and the number of glycerol would play a part in the degree of BBB disruption [73].

### *BBB Disruption by Ultrasound*

Compared with the generalized approach mentioned above for BBB opening, the advantage of ultrasound techniques is that it is site-directed opening, meaning it is capable of specifically opening the local BBB to enhance the drug delivery, thereby reducing the risk of damaging surrounding normal brain [80, 81].

### 1.5.3 Prodrug approach

The term prodrug refers to a parent drug molecule's derivatives could undergo a biotransformation within the body to release the parent drug prior to exerting its pharmacological activity[74]. The main purpose of a prodrug approach is to overcome the existing limitation factors of a drug, for example, poor aqueous solubility, chemical or metabolic instability issues, etc. In regard to the CNS delivery, a prodrug approach has been applied to overcome the problems resulting from the limited access of a drug to the brain by either a traditional approach to structurally modify a drug to become a more lipophilic prodrug or by a more sophisticated approach based on a biological delivery system mentioned in section 1.3, such as CMT, AMT, and RMT.

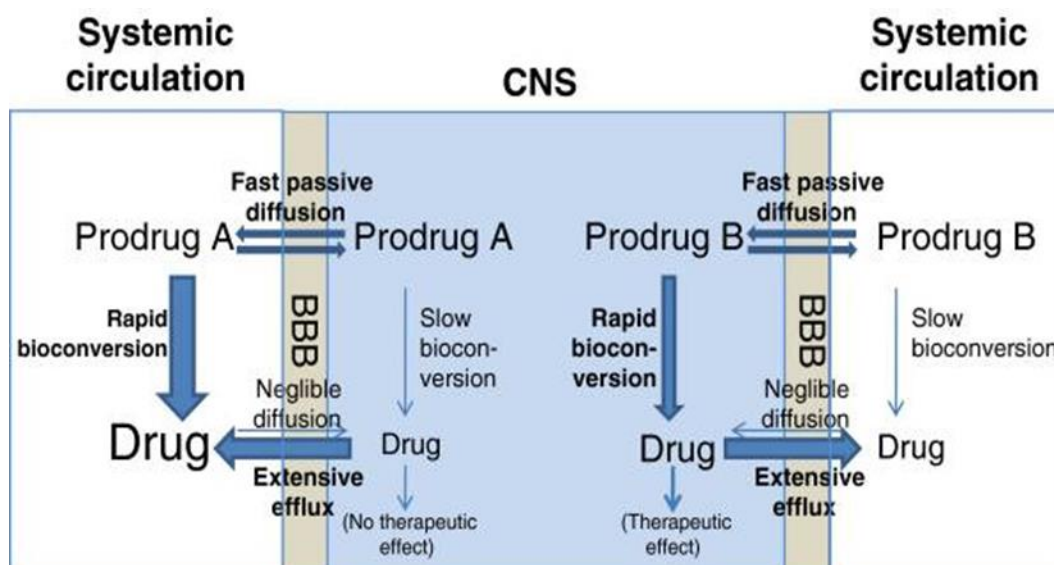


Figure 6. Key in success of CNS prodrugs. Adapted from reference [75]

For a CNS prodrug, the key is to make sure that premature bioconversion of the prodrug in the periphery is slow enough while the CNS bioconversion is fast and selective enough to enable the achievement of a therapeutic concentration of the drug before its elimination from CNS as demonstrated in Figure 6.

In this section, we will focus on the traditional method, mainly lipidation and chemical delivery systems. For prodrug design based on biological delivery systems, details will be discussed in section 1.5.4.

#### *Lipidization of small molecules*

The lipid soluble small molecules (MW <400 Da) are able to cross the BBB through the lipid bilayer. Therefore, BBB crossing is favored by small molecules with a certain lipophilicity instead of polar molecules [75]. However, small polar molecules are less favorable to go through the BBB due to the hydrophobic nature of the BBB. A prodrug approach by adding a hydrophobic and bioremoveable functional group to the drug molecule is a common approach to increase the hydrophobicity of the molecule, which is termed as lipidization of molecules [76]. After entering the brain, the prodrug is converted back to the drug [58, 77]. One of the examples is heroin, a prodrug of morphine. Heroin is obtained by acetylation of both -OH groups of morphine. Through removal of the polar hydroxyl group, heroin is able to cross the BBB ~100 fold better than its parent drug morphine. Heroin is turned back to morphine by diacetylation by an esterase in the body.

However, the drawbacks of lipidation cannot be ignored. First, the increased lipophilicity of a drug molecule is likely to increase the chance of the drug refluxed by an

efflux pump resulting in poor brain tissue retention and difficulty reaching reach therapeutic drug levels [78]. Second, the increased lipophilicity of a drug molecule may increase its permeability to other biological membranes as well, which may have an impact on its pharmacokinetics [79, 80]. Last, the molecular weight of a drug also increases, which is likely to lead to decreased BBB permeability if the molecular weight of the molecule exceeds 400–500 Da. It has been reported that BBB permeability could decrease by 100-fold, if the molecular weight a drug is increased from 200 Da to 450 Da [81].

#### *Chemical delivery system*

The chemical delivery systems (CDSs) also could be referred as a lock-in system, since the principle of CDS not only offer a way to cross the BBB by increased lipophilicity of a prodrug, but can lock the drug in the brain through generating a brain-trapped intermediate. The most investigated CDS is dihydropyridine $\leftrightarrow$ quaternary pyridinium ion redox system (Figure 7) [82].

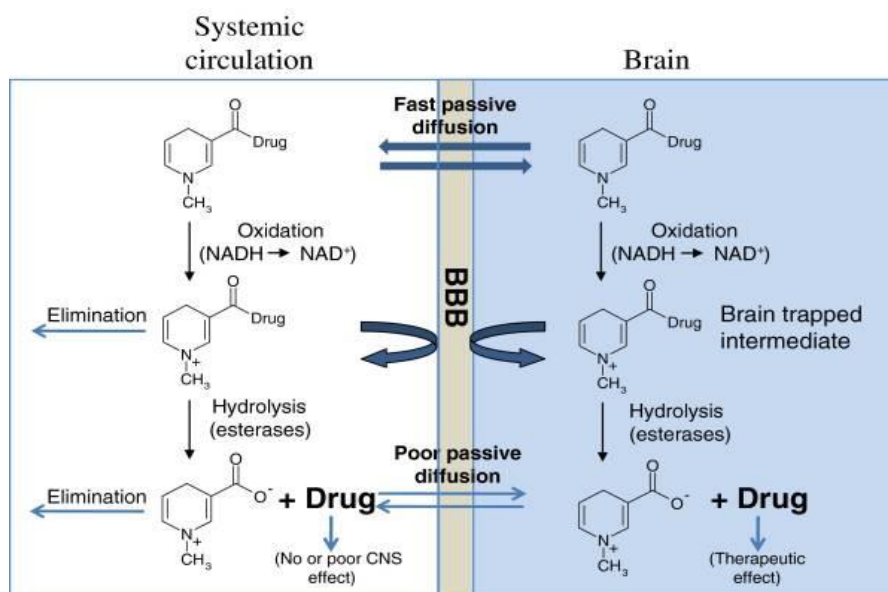


Figure 7. Illustration of the chemical drug delivery system (CDS). Adapted from reference [74]

#### 1.5.4 Biological Delivery Systems

In addition to the lipid-mediated pathway, recent attempts for CNS prodrugs have been made based on other transport mechanisms at the BBB, such as adsorptive-mediated transport (AMT), carrier-mediated transport (CMT), receptor-mediated transport (RMT), and active efflux transport. What is worth mentioning is that these transporters have also become a target for the evolution of nanocarriers drug delivery systems in an attempt to ferry drug across the BBB via a transporter-mediated pathway which will be discussed in section 1.5.6.

##### *Adsorptive-Mediated Transport (AMT)*

Adsorptive-mediated transport is generally triggered by electrostatic interaction between a cationic molecule and anionic charges on the BBB. Brain uptake of drug through cationic modification could be enhanced by conjugating a cationized protein

such as cationized albumin or cationized antibodies with the active drug. It has been reported that  $\beta$ -endorphin exhibits poor BBB passage due to its large molecular weight. The uptake of  $\beta$ -endorphin in the brain was increased after conjugation with cationized albumin[83, 84]. The most studied cationized antibody is immunoglobulin G (IgG), which is excluded from crossing the BBB in its native form. However, an enhanced BBB delivery was observed after IgG cationization[85].

The AMT system was also observed with cell penetrating peptides (CPPs), histone, and protamine[86, 87]. The most commonly used CPP is trans-activating transcriptor (TAT) peptide, which is involved in the replication cycle of HIV-1 virus. Fusion of  $\beta$ -galactosidase to TAT-peptide demonstrated the passage of the conjugated biomacromolecule across the BBB in mice[88].

#### *Carrier-mediated transport (CMT)*

Carrier-mediated transport could be implemented by modification of a drug structure into a prodrug with a structure mimicking a nutrient, such as amino acids, glucose, and vitamins. These nutrient molecule structures can be recognized by the corresponding transporter expressed in BBB and cross the BBB through mediation of their corresponding transporter. Table 1 lists the important CMT transporters in the BBB and their transported molecules.

The classic example is the transformation of dopamine to L-Dopa to deliver dopamine into the brain for the treatment of Parkinson's disease. Dopamine itself cannot cross the BBB due to its water-soluble nature, but L-dopa is a neutral amino acid and can cross BBB through large neutral amino acid transporter (LAT1) [89, 90]. L-Dopa is to

date the only prodrug that is used in clinic for entering the brain via the LAT1-mediated transport. Once inside the brain, L-dopa is decarboxylated to dopamine, a therapeutic active molecule for the treatment of Parkinson's disease. In clinical practice, around 95% of L-Dopa will be metabolized by L-amino acid decarboxylase existed in peripheral tissues, with the remaining percentage of L-dopa capable of reaching the brain and yielding the therapeutic level of dopamine in the brain[90, 91]

Another attractive and most exploited transporter is glucose transporter, especially GLUT1 transporter that constitutes >90% of BBB glucose transporters and is responsible for the transport of glucose and other hexoses[92]. Compared with other CMT transporters at the BBB, GLUT1 transporter has the highest transport capacity[93]. Researchers have designed a prodrug ester of two anticonvulsant drugs (nipecotic acid and 7-chloronokynurenic acid) by conjugating galactose and tyrosine chemically with glucose to increase the transportation across the BBB by GLUT1[94, 95]. Chlorambucil, a dialkylating anticancer agent, with the attachment of glucose through different linkers was synthesized. The result showed chlorambucil-glucose conjugate enabled its recognition by GLUT1 transporters to cross the BBB [138].

Table 1 Carrier-mediated transporters present at the BBB and their transported molecules.

<b>Transporter</b>	<b>Molecule transported</b>	<b>Reference</b>
Large neutral amino acid (LAT1)	Large and small neutral amino acid	[90, 96]
Organic anion transporting polypeptides (OATP)	Conjugated and unconjugated bile acids, hormones such as thyroid and steroid hormones	[97]
Cationic amino acid transporter (CAT1)	Basic amino acids, such as histidine, l -arginine, l -lysine, and glutamate	[98]
Monocarboxylic acid transporter (MCT1)	Lactate, pyruvate	[99]
Concentrative nucleoside transporter (CNT2)	Purine nucleosides, and certain pyrimidine nucleosides, such as uridine	[100]
Choline transporter	Choline	[101]
Glucose transporter (GLUT1)	Glucose, hexose, 2-deoxyglucose, fluorodeoxyglucose	[92, 102]
Glutathione transporter	Glutathione	[103, 104]

### Receptor-mediated transport (RMT)

Receptor-mediated transport is designed to transport large endogenous molecules, such as insulin, transferrin, or leptin to cross the BBB. They are commonly known as insulin receptor, transferrin receptor, and leptin receptor [105, 106]. There are two type of receptor-mediated transport systems: one is bidirectional receptor-mediated transport system. A typical example is transferrin receptor that can not only transport holo-transferrin from blood to the brain but also transport apo-transferrin from the brain to blood [107]. The other is the reverse receptor-mediated transport system such as neonatal Fc receptor (FcRn) that can only mediate the reverse transcytosis of IgG from the brain to blood, but not from blood to the brain [108]. Through conjugation of human transferrin (Tf) with diphtheria toxin (CRM107), CRM107 was able to distribute into malignant brain tumors area via Tf receptor-mediated transport, one of the most extensively studied RMT system [109].

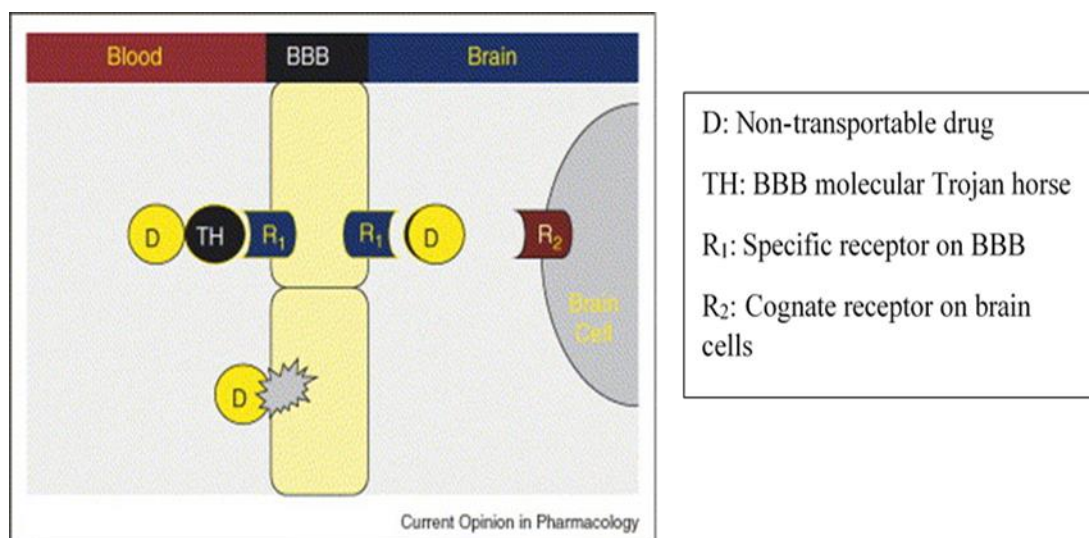


Figure 8. Blood–brain barrier Trojan horse technology. Adapted from reference [57]

The discovery of the endogenous BBB receptor-mediated transport systems has led to the development of the “molecular Trojan horse (TH)” technology for BBB transport of large molecule drugs[57, 110]. As illustrated in Figure 8, this technique takes advantage of endogenous receptors at the BBB by fusing a drug, that cannot cross the BBB, with “molecular Trojan horse”, such as endogenous peptide and certain peptidomimetic monoclonal antibodies (mAbs ) to form a chimeric peptide that is able to across the BBB, and then further to trigger the desired therapeutic effect in the brain by binding with its cognate receptor [111]. Table 2 lists receptors of brain endothelial cells that can be used as a target for drug delivery to the brain.

Table 2 Receptor-mediated transporters present at the BBB and their transported molecules.

<b>Receptor</b>	<b>Molecule transported</b>	<b>Reference</b>
Insulin receptor (INSR)	Insulin	[112]
Insulin-like growth factor receptors	Insulin like growth factor	[113]
Transferrin receptor (TFR)	Transferrin	[114]
Leptin receptor (LEPR)	Leptin	[115]
Folic acid receptor	Folic acid	[116]
Fc-like growth factor receptor (FCGRT)	Immunoglobulin	[108, 117]
Low-density lipoprotein (LDL)	LDL particles, nanoparticles, and solid lipid nanoparticles	[118]

### *Active efflux transport*

Active drug efflux pumps pump a drug out of the brain and back to peripheral blood circulation [113]. Table 3 lists active efflux transporters present at the BBB and their drug substrates. In order to avoid translocating a drug back into the blood by an active efflux transporter, three main methods have been investigated: 1) modification of drug structure to decrease their affinity to the efflux transporter. However, it is very challenging to reduce the affinity just by chemical modification since these efflux transporters have a broad substrate specificity. 2) co-administration of efflux inhibitors. It has been demonstrated that co-administration of elacridar (P-gp inhibitor) in mice could enhance CNS penetration of amprenavir (HIV Protease Inhibitor) around 13-fold [114]. 3) conjugation of an efflux inhibitor with a therapeutic drug [115]. To our knowledge, this approach has not been widely accepted for the treatment of chronic brain diseases due to a long-term impact of an efflux pump inhibition since efflux pumps are responsible for the removal of toxic metabolites from CNS as well. The consequence of chronic inhibition of efflux systems is the accumulation of toxic compounds in the brain that may result in neurodegenerative disease [116].

Table 3 Active efflux transporters present at the BBB and their drug substrates.

<b>Active efflux transporter</b>	<b>Expression</b>	<b>Drug Substrate</b>
P-gp	BBB-apical	Abacavir [119]
	Choroid plexus (CP)- apical	Digoxin[120]
BCRP	BBB-apical	Gefitinib[121], Topotecan[122]
MRP4	BBB-apical	9-(2-phosphonylmethoxyethyl)adenine (PMEA)[123]
	CP-basolateral	Topotecan[124]

### 1.5.5 Intranasal drug delivery to the brain

An alternative non-invasive method to deliver drugs to the CNS is intranasal administration. After intranasal administration, therapeutically active compounds are able to reach the CNS through the CSF of olfactory region by being absorbed via olfactory sensory neurons. Recent studies suggests that drug uptake through this pathway depends on the molecular weight and the lipophilicity of the drug. Brain-derived neurotrophic factor (BDNF) have been successfully delivered into brain for the treatment of Alzheimer's disease by this approach[125]. The benefit of this pathway is that drugs can avoid first-pass drug metabolism. However, there are still other physiological factors associated with drug administration via intranasal pathway. These factors include higher pH, high enzymatic activity of the epithelium, and mucosal irritation [126].

### 1.5.6 Nanocarriers drug delivery to the brain

The term nanocarriers refer to colloidal nanoparticle (NP) carrier systems. They include liposomes, micelles or polymeric nanoparticles formed by natural materials (i.e., chitosan, polysaccharides) or synthetic material (i.e., polymer, inorganic substances) with a size ranging roughly from 1 nm to 1000 nm. Table 4 lists the examples and features of current nanoparticle platforms.

Table 4 Current nanoparticle platforms and its features

NPs	Size	Main component	Reference
Liposomes	10nm-1000nm	Lipid	[115]
Micelles	20nm-200nm	Amphiphilic molecule	[127]
Polymeric nanoparticles	10nm-1000nm	Polymer	[118]
Gold nanoparticles	1 nm–100 nm	Gold	[128] [129]
Solid lipid nanoparticles	10nm-1000nm	Lipid and emulsifier	[130]

Using NPs as brain drug delivery systems has shown the advantages of improved drug solubility, enhanced drug stability in blood circulation, increased BBB passage, and controlled drug release. Further, the payload incorporated into NPs can be a

therapeutic drug or an imaging probe making it applicable for treatment or diagnosis. More importantly, the surface of NPs can be easily modified to meet various applications. NPs deliver their cargo across the BBB through passive and active targeting.

#### **1.5.6.1 Passive targeting**

Passive targeting, in principle, is achieved through the enhanced permeability and retention (EPR) effect. The EPR effect is the high and effective accumulation of macromolecules in a disease site due to the fact that the vascular endothelium becomes more permeable under a disease state than that in the healthy state. Furthermore, a lack of adequate lymphatic drainage in cancer sites also contributes to the EPR effect.

NPs take advantage of these unique features to passively target and selectively accumulated in brain cancer. The passive targeting of NPs also relies on the characteristic properties (size and circulation time) of nanocarriers. The inherent limitation of passive targeting is that only a small amount of NPs will reach the brain tumor sites due to the opsonization and the clearance by reticuloendothelial system (RES) while the most common locations where NPs are trapped in are liver, spleen, lung, and kidney. To achieve better EPR effect for passive targeting in CNS drug delivery, the size of NPs need to be smaller than 150nm and the surface of NPs could be modified to avoid the clearance from RES.

Current application of passive targeting for NPs is mostly restricted to brain cancer with no severely disrupted BBB [131].

### 1.5.6.2 Active targeting

An initial approach of active targeting is to design a prodrug by conjugating an endogenous ligand with a drug. The prodrug is expected to have a good affinity with the corresponding specific transporter present in the BBB and transported into the brain by the biology transport system (e.g., AMT, CMT, RMT).

With the emergence of NPs and the feasibility of functionalizing NPs' surface, an alternative approach for active targeting of NPs is to couple an endogenous ligand to NPs' surface through covalent or non-covalent linkage or by indirectly coating NPs' surface with an endogenous ligand. The mechanism of transporting these surface-functionalized NPs across the BBB is through the corresponding transporter or receptor of the coupled surface endogenous ligand by the biology transport systems at the BBB.

Cationized albumin (CBSA) was known to be involved in the AMT system and CBSA-conjugated PEGylated liposomes exhibited high accumulation in porcine brain capillary endothelial cells (BCEC) in contrast to albumin (BSA)-conjugated PEGylated liposomes[132]. Another AMT-based delivery is CPPs that have been successfully exploited to enhance drug delivery by various nanocarriers. Studies showed that trans-activating transcriptional activator (TAT) -conjugated PLA nanoparticles help promote the delivery of anti-HIV drug ritonavir to the CNS[133]. Brain targeting via large amino acid transporter 1(LAT1) in the CMT system has been employed in docetaxel-loaded glutamate decorated liposomes with the aim to overcome the problem of the low BBB permeability of docetaxel and to increase cellular uptake by brain glioma [134]. Apolipoprotein E derived peptide-coupled PEGylated liposomes have been developed based on the fact that the low-density lipoprotein (LDL) receptor is involved in transportation of low-density

lipoprotein via the RMT system and the result showed an increased uptake of liposomes by both porcine brain capillary endothelial cells and isolated intact brain capillaries[128]. Cross-reacting material 197 (CRM197), a ligand of diphtheria toxin receptor (DTR), has been grafted to polybutylcyanoacrylate (PBCA) NPs with zidovudine (AZT) loaded inside. A permeability study with human brain-microvascular endothelial cells demonstrated that AZT-loaded CRM197/PBCA NPs yielded more permeation across the BBB [135].

It is worth noting that some of the receptors can also bind monoclonal antibody (mAbs) or their fragments beside binding with their natural ligands. These antibodies-conjugated NPs have been thoroughly investigated for BBB targeting. For instance, the natural ligand for TfR is iron binding protein T. However, evidence showed that OX26 antibodies could also bind to TfR at the site different from transferrin-binding site – a site that can avoid affecting the normal transport of transferrin[136]. OX26 modified hyperbranched polyglycerol-conjugated poly (lactic-co-glycolic acid) nanoparticles (HPG–PLGA NPs) loaded with endomorphins was prepared and showed both time- and concentration-dependent uptake of OX26 modified NPs by brain endothelial cells. Moreover, OX26 modified HPG–PLGA NPs can effectively deliver endomorphin into the brain to show its analgesic effects in chronic constriction injury (CCI) indicating the ability of OX26 modified HPG–PLGA NPs to cross the BBB via TfR mediated transport[137]. In addition to the ligand discussed above, several other targeting moieties for BBB transporters/receptors have also been applied to various NPs for drug delivery into the brain (Table 5).

Table 5 Other ligands studied for NPs to cross the BBB

<b>NPs</b>	<b>Ligand</b>	<b>Transporter/Receptor</b>	<b>Cargo</b>	<b>Application</b>	<b>Ref</b>
PEGylated liposome	FA	FaR	Doxorubicin	Brain tumor	[138]
ODN/PEI polyplex	8D3 antibody	TfR	Anti-sense oligonucleotides	Neuro-inflammatory diseases	[139]
Gold NPs	Insulin	InR	-	Imaging and therapeutic	[129]
Human serum albumin NPs	29B4 antibody	InR	Loperamide	Antinociceptive	[140]
PEG-PLGA NPs	Lf	LfR	Urocortin	Parkinson's disease	[141]
PLGA NPs	TMC	Negative charged molecule	Q10(Co-Q10)	Alzheimer's Disease	[142]
SPIO NPs	EGF	EGFR	-	Imaging and Brain glioma	[143]
Avidin-nanomicelles	Biotin- $\alpha$ -PECAM1 Antibody	Biotin	-	Brain uptake	[144]

## 1.6 GSH for brain targeting

GSH is an endogenous tripeptide consisting of glutamate, cysteine, and glycine. GSH is involved in the intracellular redox reaction and plays a significant role in protecting cells from oxidative stress and xenobiotics [145]. GSH deficiency is known to be associated with a number of neurological diseases[146]. Although the brain is able to synthesize GSH, it needs to take GSH from the systemic circulation to meet its need. Since GSH is water-soluble and cell membrane impermeable, it crosses the BBB through the aid of a GSH transporter in the BBB [147]. Studies showed that GSH transportation into the brain depends on a sodium dependent GSH transporter localized on the luminal membrane of endothelial cells[103, 148, 149]. GSH transporter has a preferential expression in the BBB in all mammalian species [148, 150]. The expression of GSH transporters in other tissues are limited except in kidneys. It has been reported that GSH transporter is richly expressed in kidneys, since the kidney is the main organ to ingest and degrade GSH. Around 80% of plasma GSH is taken by the kidney, and 62.5% of them enters the renal tubule in the form of GSH through a GSH transporter[151].

The overexpression of GSH transporter in the BBB and well-established safety profiles of exogenously administered GSH make GSH an attractive ligand for developing brain-targeting agents. In fact, GSH has been linked to PEG (PEGylated GSH) and the PEGylated GSH has been coated to the surface of liposomes (GSH-PEG liposomes) to develop brain-targeting liposomes. GSH-PEG liposomes have been demonstrated for safe delivery of doxorubicin, methylprednisolone, and opioid peptide to the brain [152-155]. GSH-PEG liposomal doxorubicin (2B3-101) demonstrated an enhanced brain delivery of doxorubicin and acceptable safety profile in brain tumor-bearing mice resulting in a

reduced tumor growth and prolonged survival. The promising results also led to the clinical phase I/IIa studies of 2B3-101 in patients with solid tumors and brain metastases or recurrent malignant glioma (clinicaltrials.gov NCT01386580) in 2014[152]. GSH-PEG liposomal methylprednisolone (2B3-201) has also been found to enhance the sustained delivery of methylprednisolone by around 6.5-fold when compared with free methylprednisolone in a rat model with neuroinflammation[154]. Additionally, GSH has also been successfully utilized in other nanocarrier systems. For instance, GSH conjugated cationic poly(ethyleneimine)s has been synthesized to enable genetic material delivery[156]. More recently, the possibility of GSH-conjugated magnetic nanoparticles as an MRI-monitored paclitaxel (PTX) delivery vehicle across the BBB using BALB/c mouse model has also been demonstrated[157].

Besides the nanocarrier systems, GSH transporter targeted prodrug has also been designed by using a suitable linker between GSH and the active drug. More, SS More and colleagues used GSH as a brain targeting ligand and successfully designed brain targeting prodrugs for dopamine and adamantamin [158].

1.7 COXP as a GSH brain-targeting agent and COXP micelles as brain targeting micelles *This work was published in Int J Pharm. 2021 May 1;600:120520*

In our recently published work [159], we have successfully designed and synthesized amphiphilic molecule 2-(2-cholesteroxyethoxy)ethyl 3'-S-glutathionylpropionate (COXP) by connecting the hydrophilic GSH molecule with a hydrophobic cholesterol through a two-ethylene glycol unit linker (Figure 9). COXP can self-assemble to form micelles in aqueous solution due to its amphiphilic nature.

Micelle is one of the well-established effective drug nanocarriers that have been used widely for a decade to deliver various molecules, covering from small molecules to macromolecules (i.e., DNA, RNA, and proteins)[160, 161]. Compared with other nanocarriers mentioned in section 1.5.6, micelles have their own merits. First, it has a relatively small hydrodynamic size[162, 163]. Particles with small size (e.g., < 100 nm) benefit tissue penetration and cellular uptake in regard with the dimensions of physiological pores in the body such as tumor tissue and endothelial junctions of healthy tissue[164-166]. Therefore, small micelles are capable of enhancing the performance of encapsulated drugs *in vivo*, causing high accumulation at the target site and improving the cellular response[163, 167, 168]. Second, micelle formulations are favored for large-scale manufacture on account of its self-assembled nature that allows simple drug formulation and easy manufacturing[169]. These two advantages offer micelles an opportunity to become a crucial drug formulation technology[160].

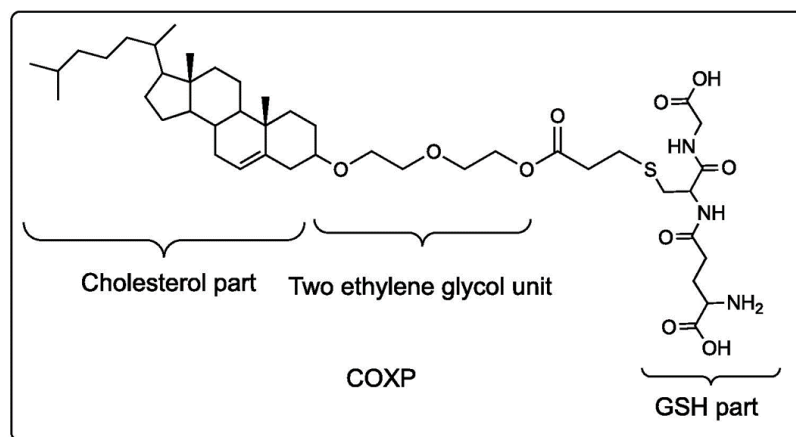


Figure 9. Chemical Structure of COXP.

One of the critical parameters to determine whether the micelles will be stable enough as a drug delivery system for clinical application is the critical micelle

concentration (CMC)[170]. CMC is a concentration at which an amphiphilic molecule starts to form micelles while below the CMC, the amphiphilic molecule remains as a monomer. In general, the CMC of micelles needs to be in  $\mu\text{M}$  concentration so that the micelles are stable enough to remain as micelles once being diluted in the bloodstream after administration[171].

As illustrated in Figure 10, the feature of our COXP micelle is that the hydrophilic GSH molecule is located on the micelle surface to serve as a ligand for GSH-transporter for brain targeting, and the hydrophobic cholesterol molecule towards the inside to form the inner hydrophobic core to encapsulate hydrophobic drug molecules. In addition to serving as a hydrophobic part of the COXP structure, cholesterol is an endogenous molecule. COXP is expected to be less toxic and biocompatible since it releases two endogenous molecules (GSH and cholesterol) after degradation in the body [172]. The CMC value of COXP micelles was determined to be  $3.9 \mu\text{M}$ , suggesting COXP micelle is stable enough to be used as a drug delivery system for a clinical application.

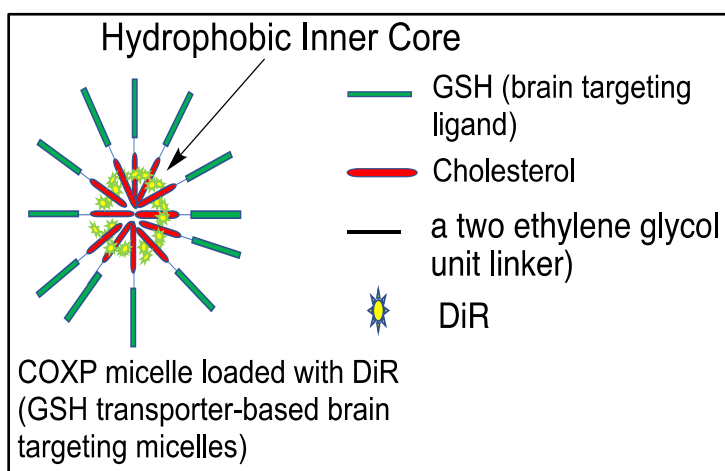


Figure 10. DiR loaded COXP micelles

The result from the *in vitro* releasing study of Rhodamine B loaded COXP micelles showed that Rhodamine B was uniformly released from COXP micelles for 24 h with the majority released in about 4 h. In comparison, the majority of free Rhodamine B were detected in the dialysis buffer within 1 h (Figure 11).

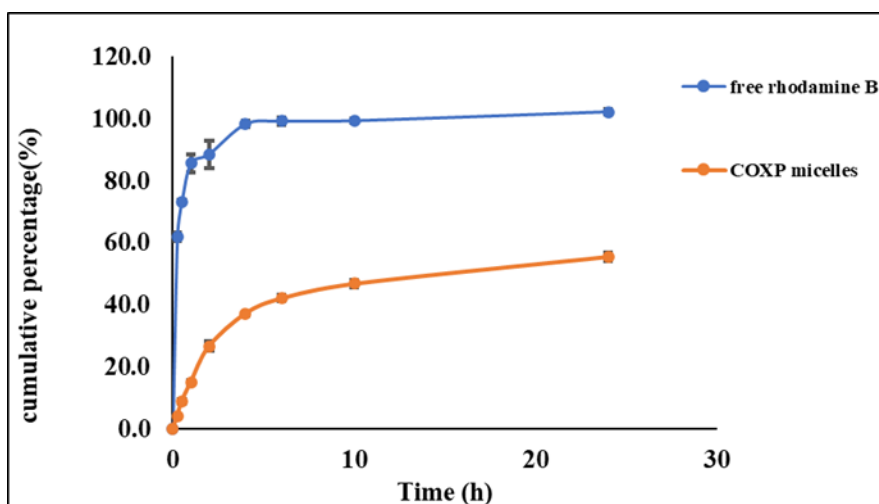


Figure 11. Release of Rhodamine B from Rhodamine B loaded COXP micelles.

Rhodamine B loaded COXP micelles (4.7 $\mu$ g rhodamine/mL, 0.5 mL) were dialyzed in a pre-swollen dialysis bag (molecule weight cut-off: 10 kDa) in a 40 mL PBS buffer with a stirring speed of 100 rpm. Aliquots (3 mL) were withdrawn at predetermined time (0, 0.25, 0.5, 1, 2, 4, 6, 10, 24 h) for HPLC analysis of Rhodamine B. After each aliquot was withdrawn, the same volume of the PBS buffer was added back to maintain the dialysis volume. A parallel dialysis in which a dialysis bag containing the same amount of free Rhodamine B was conducted for comparison. Data are presented as the mean  $\pm$  SD (n=3).

To determine whether COXP micelles exhibit a brain-targeting effect, DiR-loaded COXP micelles were prepared by a film dispersion method (Figure 1.9). DiR is a hydrophobic fluorescence tracking agent that can be used to help track tissue distribution

of COXP micelles in mice. The particle sizes of DiR-loaded COXP micelles were determined to be  $29.1 \pm 5$  nm with a poly distribution index (PDI) value of 0.126, indicating a narrow size distribution of micelles. The zeta potential of DiR-loaded COXP micelles was found to be  $-19 \pm 2.1$  mV, suggesting the negatively charged GSH molecules are located on the surface of the micelles. The encapsulation efficiency (EE%) and loading capacity (LC%) of DiR-loaded COXP micelles were determined to be  $68 \pm 0.6\%$  and  $0.24\%$  respectively. We also demonstrate that DiR-loaded COXP micelles were stable enough in the stock solution for 5 days at  $4^\circ\text{C}$ .

Brain targeting of DiR-loaded COXP micelles was investigated through the whole-body fluorescence imaging. The result is shown in Figure 12. DiR-loaded COXP micelles distributed to the brain rapidly in 15 min while no significant fluorescence was observed in the brain of the mice treated with free DiR. The brain fluorescence intensity remained strong in mice treated with DiR-loaded COXP micelles even at 48 h (Figure 12-I). Figure 12-II shows the brain distribution of DiR delivered by COXP micelles was around 20 folds higher compared with free DiR at different times.

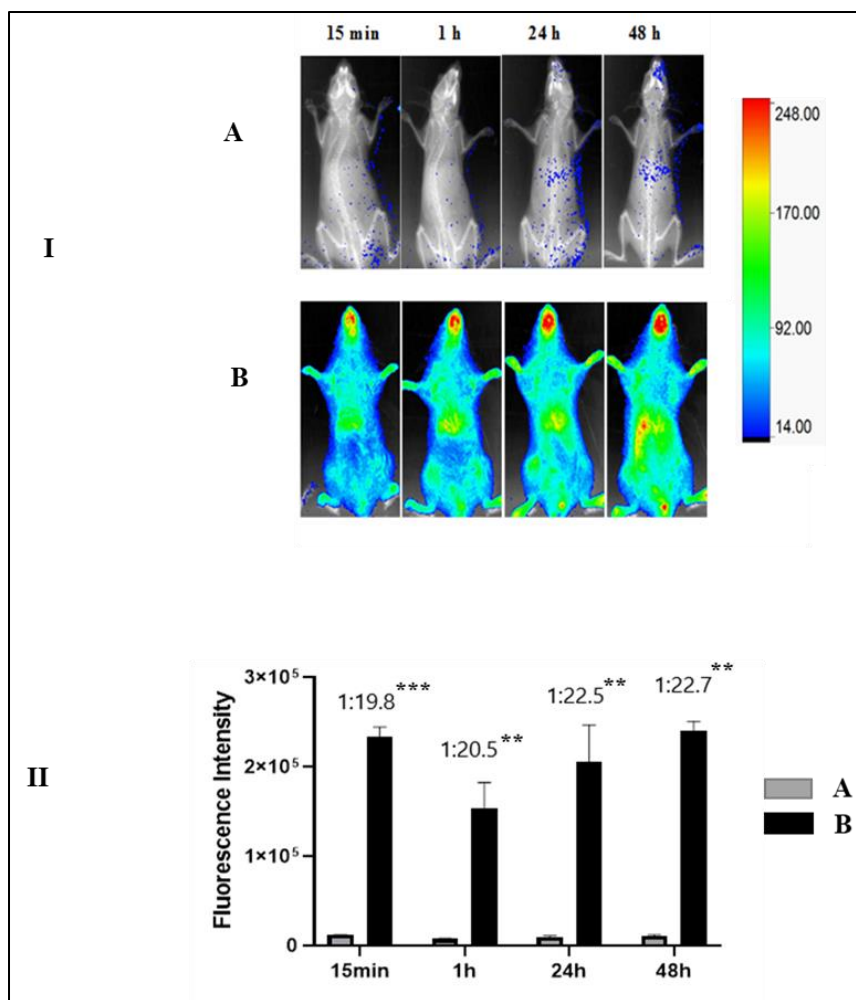


Figure 12. Results from the whole-body fluorescence imaging of mice after a single dose tail vein injection of free DiR (A: 5  $\mu$ g DiR in 25  $\mu$ L ethanol, control) and DiR loaded COXP micelles (C: 0.2 mL containing 5  $\mu$ g DiR). I: Representative images derived from in vivo whole-body fluorescence imaging. II: Brain fluorescence intensities from the whole-body imaging in I. Results are presented as mean  $\pm$  SD (n=3).  $P < 0.05$  \*;  $P < 0.01$  \*\*;  $P < 0.001$ \*\*\*

Further, the *ex-vivo* imaging of isolated brains from mice with a treatment of DiR-loaded COXP micelles or free DiR after 1h demonstrated that the fluorescence intensity was significantly higher from the brains of the mice treated with DiR-loaded

COXP micelles when compared with free DiR (Figure 13-I). Approximately 8.1-fold increase in fluorescence intensity in the brains of mice treated with DiR-loaded COXP micelles was observed when compared with free DiR ( $P < 0.05$ , Student's t-test) (Figure 13-II).

Since COXP micelles were able to deliver DiR to the brain, the next step was to investigate if COXP micelles were taken by cells through a GSH transporter. For this investigation, mouse kidney cells were employed since it is known that kidney cells are rich in GSH transporters, and a kidney (MDCK II) cell line has already been used to explore and confirm that glutathionyl prodrugs entered the cell via a glutathione transport system [158]. Rhodamine B loaded COXP micelles were used in the investigation instead of DiR loaded COXP micelles due to the detection sensitivity issue with DiR. Both Rhodamine B and DiR are cationic hydrophobic molecules. As shown in Figure 14, Rhodamine B loaded COXP micelles were taken by the kidney cells readily. In a literature report, GSH-transporter mediated cell uptake was significantly inhibited by probenecid [173]. A similar result was obtained. In the presence of probenecid (1 mM), the cell uptake of Rhodamine B loaded COXP micelles was inhibited significantly (Figure 14).

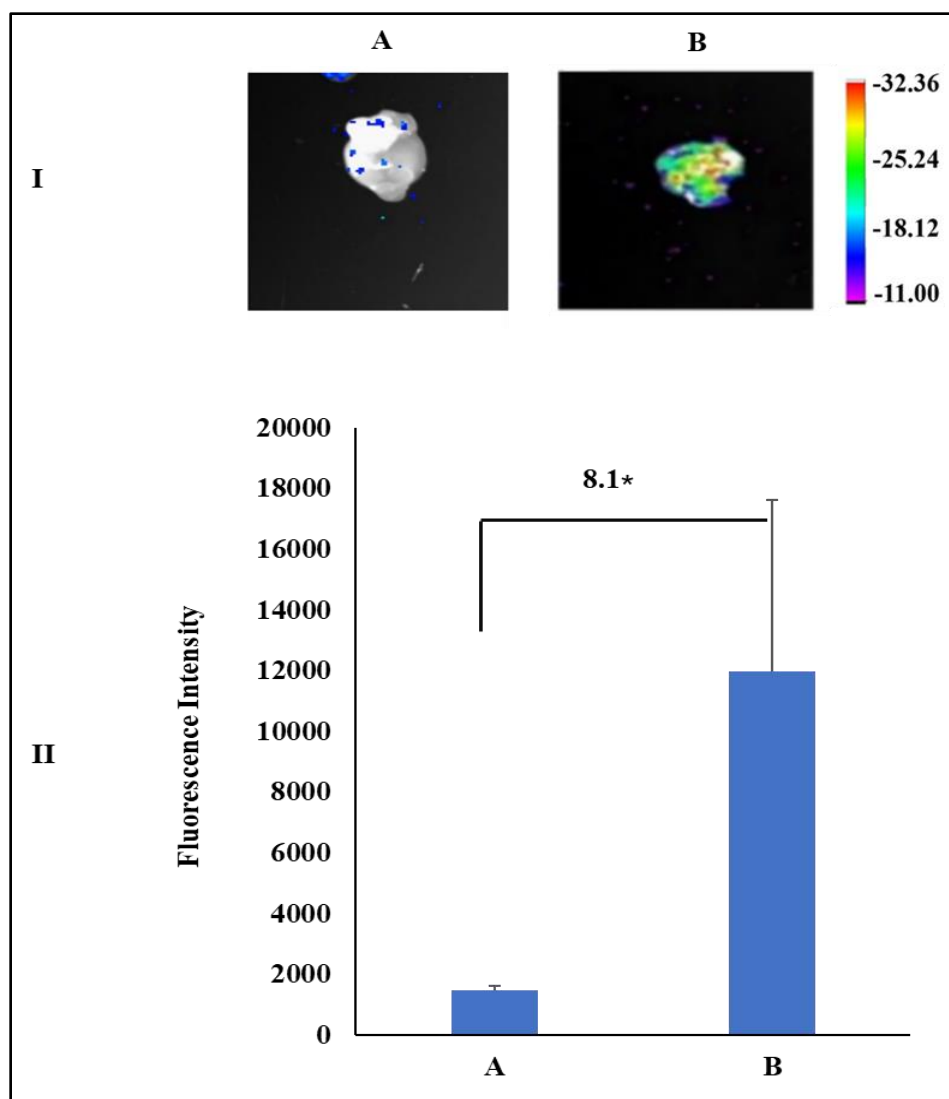


Figure 13. Representative *ex-vivo* images (I) and corresponding fluorescence intensities (II) of the mouse brains 1 h after a single dose tail vein injection of free DiR (A: 5  $\mu$ g DiR in 25  $\mu$ L ethanol, control) and DiR-loaded COXP micelles (B: 0.2 mL containing 5  $\mu$ g DiR). Data are presented as mean  $\pm$  SD ( $n = 3$  for A,  $n = 4$  for B).  $P < 0.05$  \*

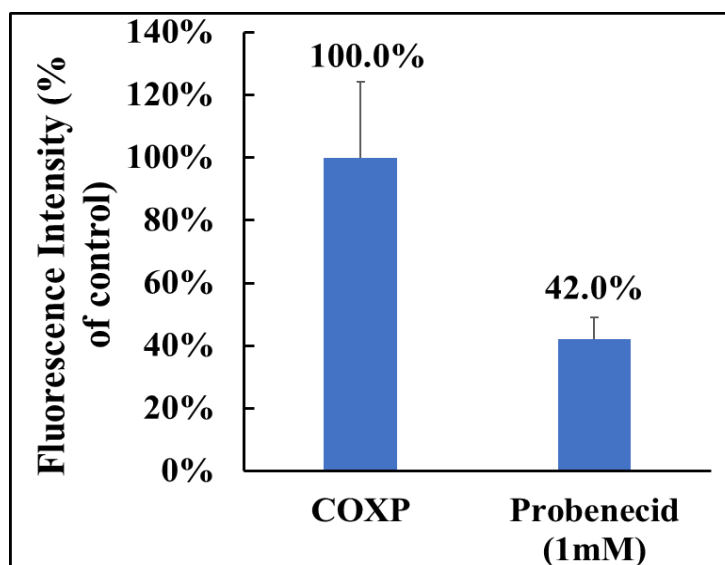


Figure 14. Cell uptake and uptake inhibition of COXP micelles by probenecid. Mouse kidney cells (2<sup>nd</sup> passage) were placed in a 96 well plates with a concentration of 5000 cells/well. When a 90% confluence was reached, cells were treated with medium only (no inhibitor) or probenecid (1 mM) for 30 min followed by replacement of the medium containing only Rhodamine B loaded COXP micelles (0.35 mg/mL) or Rhodamine B loaded COXP micelles (0.35 mg/mL) plus probenecid (1 mM), The cells were allowed to incubate at 37 °C for an additional 30 min before removal of the medium and measured for fluorescence intensity with a microplate reader ( $\lambda_{ex}$  540 nm,  $\lambda_{em}$  625 nm). *The data are expressed as a percentage of control (COXP group). (n = 3, P < 0.05\*, P < 0.01\*\*, Student's t-test).*

Our work demonstrate that COXP micelles can effectively transport DiR to the brain via a GSH transporter mediated process and provide a proof of concept for the potential application of COXP micelles as an effective brain drug delivery system. In addition, our data also demonstrate the strategy of using GSH as brain targeting ligand to

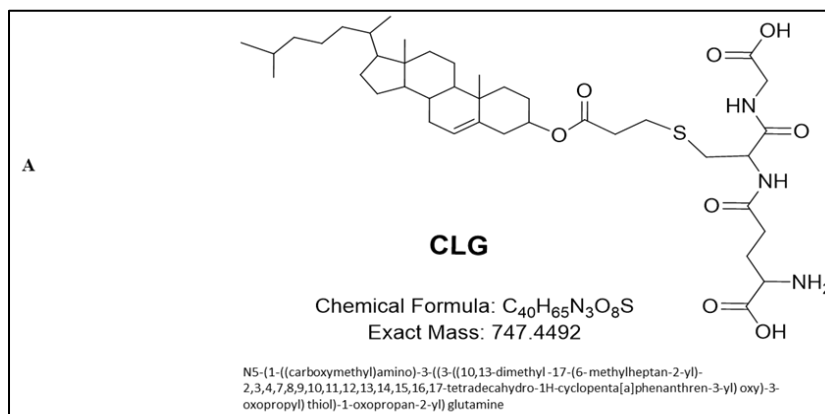
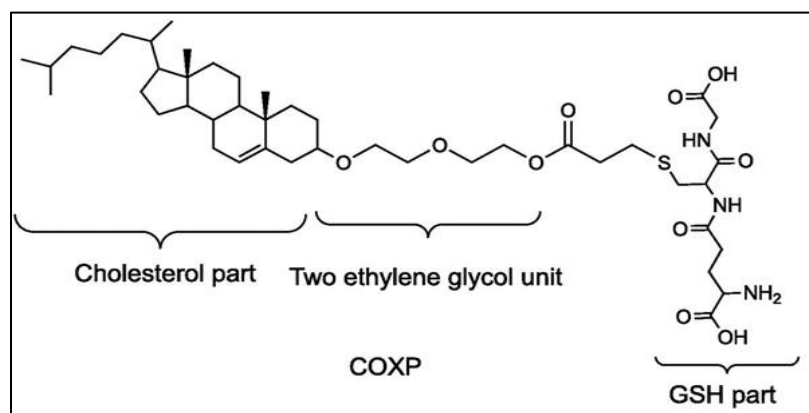
design a brain targeting molecule is a valid one. A patent application has been filed for COXP as well as COXP micelles for brain targeting[173].

The aim of this dissertation was to identify more effective brain targeting molecules and brain-targeting drug delivery systems by conducting structural modification of COXP. The structural modification mainly involved two parts of the COXP structure: i). replacement of the linker between GSH and cholesterol (Chapter 2); ii). replacement of the cholesterol structure with a long chain fatty alcohol (Chapter 3).

## CHAPTER 2 DESIGN, SYNTHESIS, AND EVALUATION OF CLG, COLG AND CNLG AS BRAIN TARGETING AGENTS

### 2.1 Introduction

As discussed earlier, COXP was designed as a GSH transporter-mediated brain targeting amphiphilic molecule capable of self-assembling to form a micelle. In this chapter, we modified the linker to see if better brain targeting agents and better brain targeting micelles can be identified. Three structural modifications of the linker were conducted (Figure 15): i). to decrease the length of the linker (CLG); ii). to increase the length of the linker (COLG); iii). to replace the ester group of the linker with an amide group which is more resistance to biodegradation (CNLG).



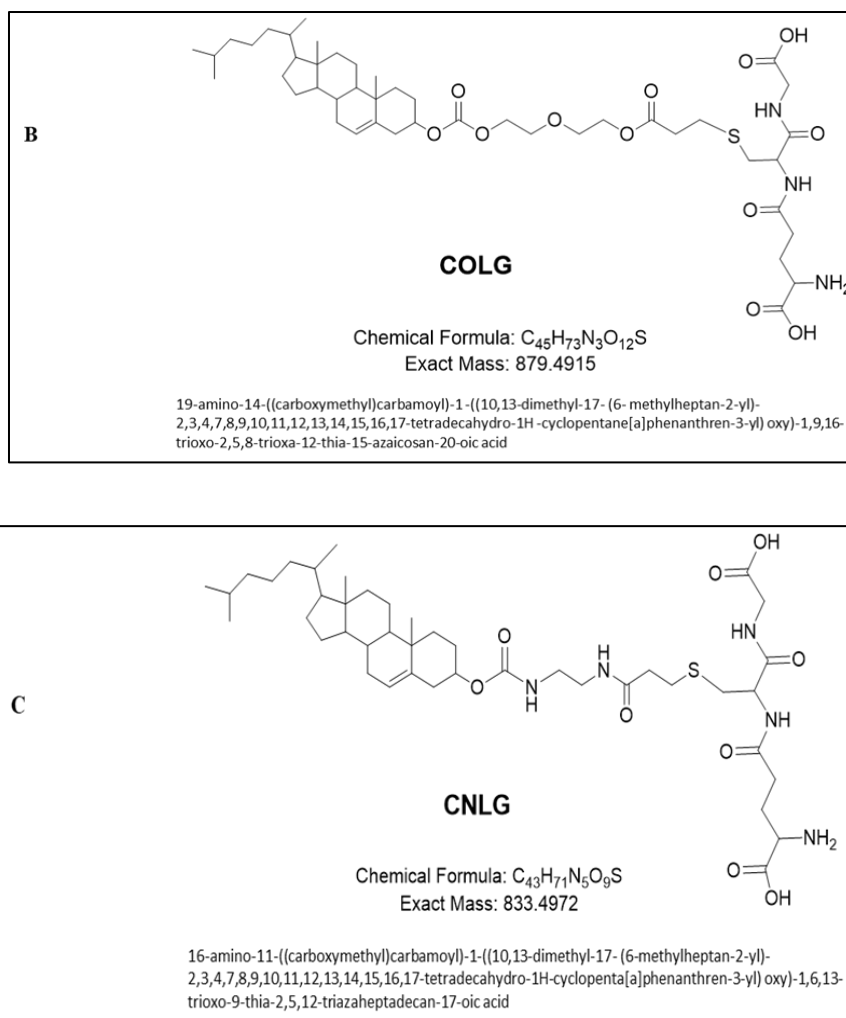


Figure 15. Chemical structure of COXP and COXP derivatives (**A**: CLG; **B**: COLG; **C**: CNLG).

These three compounds were synthesized and fully characterized. All three were able to undergo self-assembly to form a micelle. A preliminary study with *ex-vivo* imaging of the collected brains showed that CNLG micelles had a better brain targeting ability than CLG micelles and COLG micelles. Therefore, we decided to focus on CNLG micelles for a full investigation of the nanoparticles as a brain targeting delivery system. The whole-body imaging results demonstrate that CNLG micelles delivered DiR to the

brain >40 fold higher when compared with free DiR, significantly higher than COXP micelles which delivered DiR 20 fold higher to the brain when compared with free DiR.

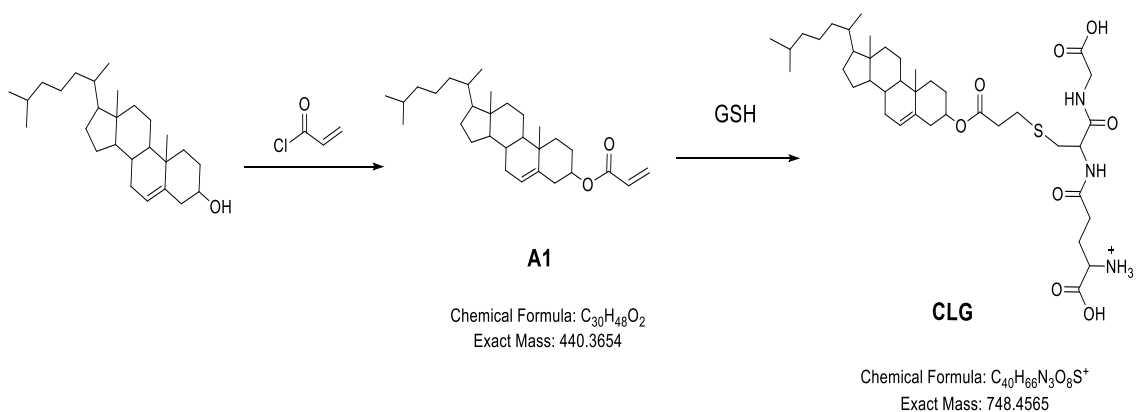
## 2.2 Result and Discussion

### 2.2.1 Synthesis and characterization

#### 2.2.1.1 Synthesis and characterization of CLG

CLG was synthesized in 2 steps as outlined in Scheme 1. The synthesis started with esterification of cholesterol with acryloyl chloride in the presence of triethylamine to yield compound (A1) in 52% yield. Then, GSH was attached to compound A1 through a Michael addition reaction to produce our desired compound (CLG) in 48% yield with a melting point of 204 °C.

CLG was characterized by  $^1\text{H}$  NMR, IR and HRMS. The calculated HRMS for the protonated CLG [ $\text{C}_{40}\text{H}_{66}\text{N}_3\text{O}_8\text{S} (\text{M}+\text{H})^+$ ] is 748.4565 and the found is 748.4563 (Figure 16). The purity of CLG was checked by HPLC and found to be >97%.



Scheme 1 Synthesis of CLG

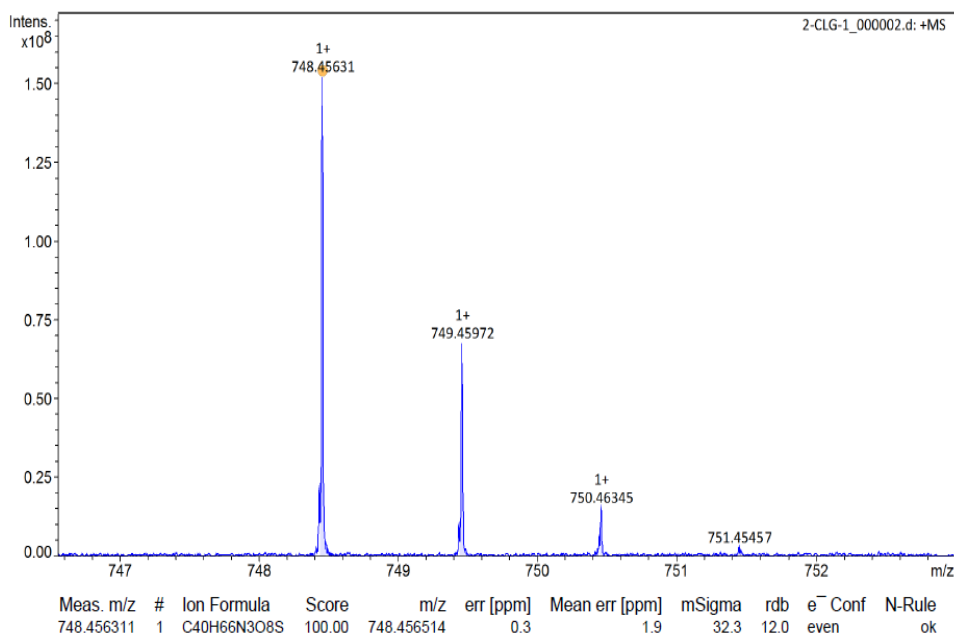


Figure 16. HRMS spectrum of CLG

It needs to be noted that our desired product CLG is an *S*-isomer (Figure 17) resulting from a Michael addition reaction of the thiol group of GSH in the last step. However, it is possible that the Michael addition could occur with the addition of the amino group of GSH in the last step leading to an *N*-isomer (Figure 17), although a thiol Michael addition is much preferred than an amino Michael addition and the predicted dominating product should be the *S*-isomer. It has been reported that the MS fragmentation pattern obtained from LC/MS/MS was capable of differentiating the structure between the *S*-isomer and the *N*-isomer [174]. For the *S*-isomer, two neutral losses [neutral loss of glycine ( $C_2H_5NO_2$ , 75 Da) and neutral loss of pyroglutamate ( $C_5H_7NO_3$ , 129 Da)] are expected. For the *N*-isomer, a neutral loss of 178.04 Da ( $C_5H_{10}N_2O_3S$ ) is expected (Figure 17).

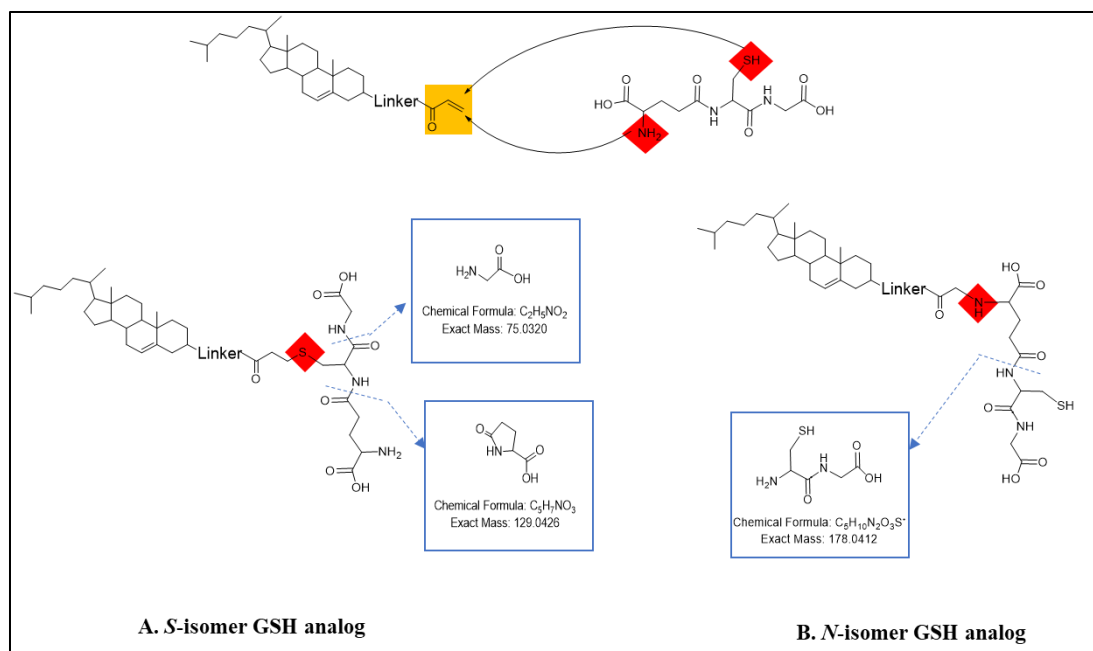


Figure 17. *S*-isomer (A) and *N*-isomer (B) of GSH analog generated from Michael addition with GSH and their expected MS fragmentation pattern.

As demonstrated in Figure 18, two neutral losses with  $m/z$  fragment at 75.28 and  $m/z$  fragment at 129.86 generated from glycine and pyroglutamate respectively were observed in the LC/MS/MS spectrum of CLG. Besides, the  $m/z$  fragment at 369.5 generated from the cholesterol ion was also observed. These two neutral losses plus the cholesterol ion fragment match well with the structure of *S*-isomer not *N*-isomer, thus confirming out product is the *S*-isomer.

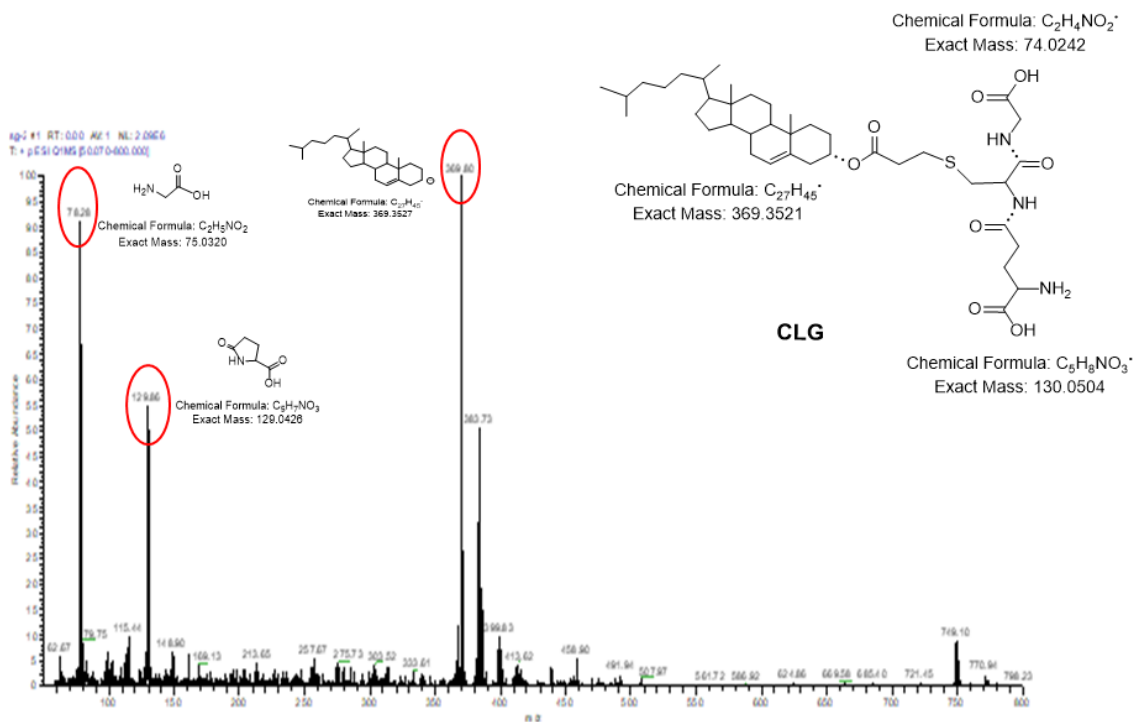
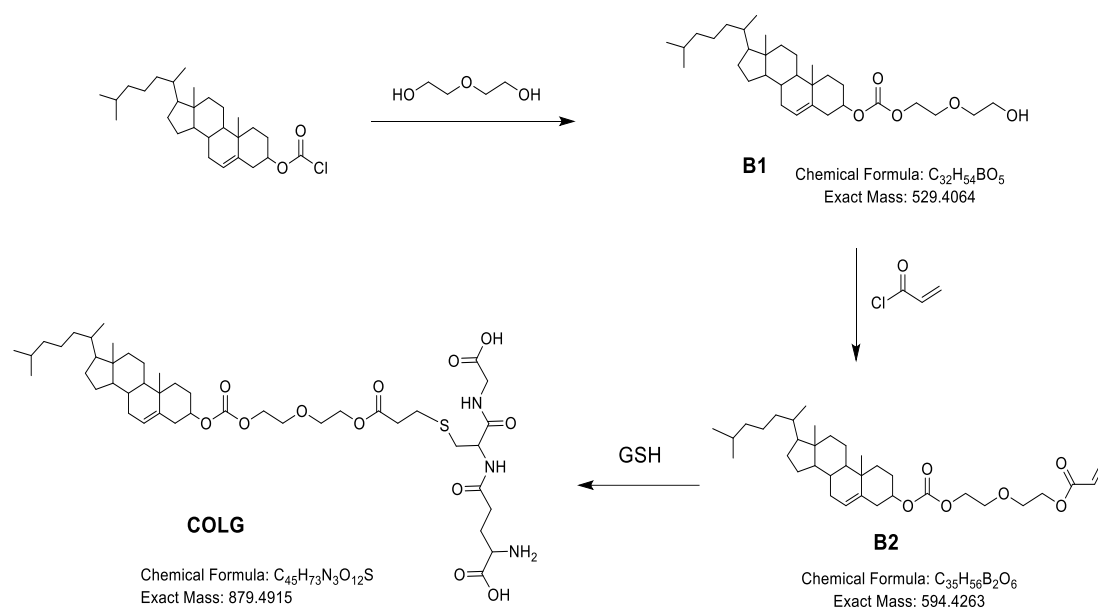


Figure 18. LC/MS/MS spectrum of COLG

### 2.2.1.2 Synthesis and characterization of COLG

COLG was synthesized in 3 steps as outlined in Scheme 2. The synthesis started with esterification of diethylene glycol with cholesteryl chloroformate in the presence of triethylamine to yield compound B1 in 70% yield. Compound B1 reacted with acryloyl chloride through another esterification at a similar condition to yield compound B2 in 33% yield. The final compound (COLG) was produced through a Michael addition of thiolate in GSH with compound B2 in 58% yield with a melting point of 204 °C.

COLG was characterized by <sup>1</sup>H NMR, IR and HRMS. The calculated HRMS for the sodium adduct of COLG (C<sub>45</sub>H<sub>73</sub>N<sub>3</sub>O<sub>12</sub>S) (M+Na)<sup>+</sup> is 902.4807 and the found is 902.4804 (Figure 19). The purity of COLG was checked by HPLC and found to be >97%.



Scheme 2 Synthesis of COLG

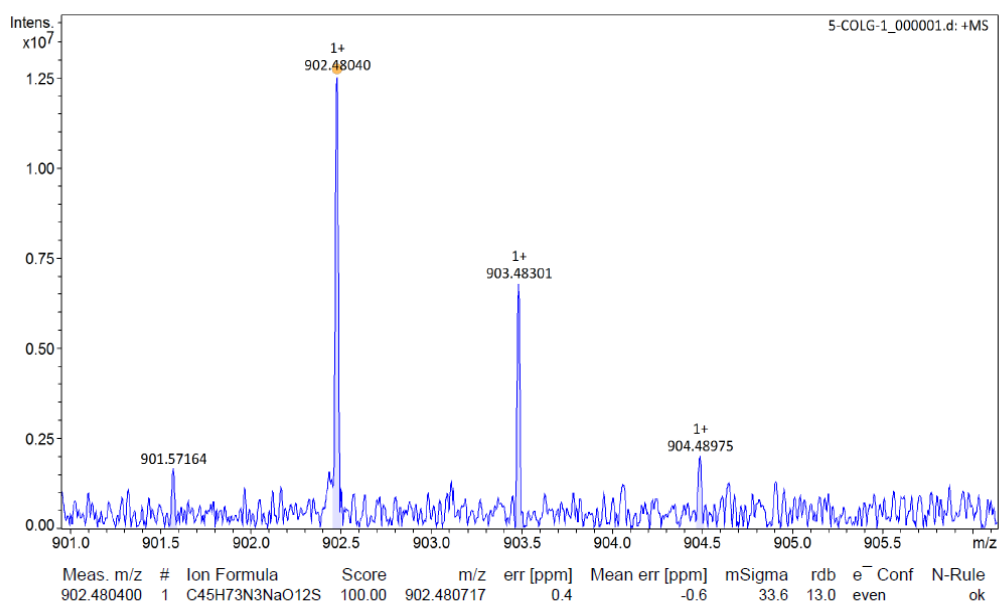


Figure 19. HRMS spectrum of COLG

Similar to CLG, COLG was confirmed to be the *S*-isomer by LC/MS/MS not *N*-isomer based on the fact that two fragments ( $m/z$  fragment at 805.4 and  $m/z$  fragment at

750.4) generated from the neutral losses of glycine and pyroglutamate respectively were observed (Figure 20). In addition to these two reported typical neutral losses of the *S*-isomer,  $m/z$  fragment at 369.5 generated from the cholesterol ion and the  $m/z$  fragment at 468.2 generated from the neutral loss of  $C_{17}H_{29}N_3O_{10}S$  were also observed, which further confirmed the structure of the *S*-isomer of COLG.

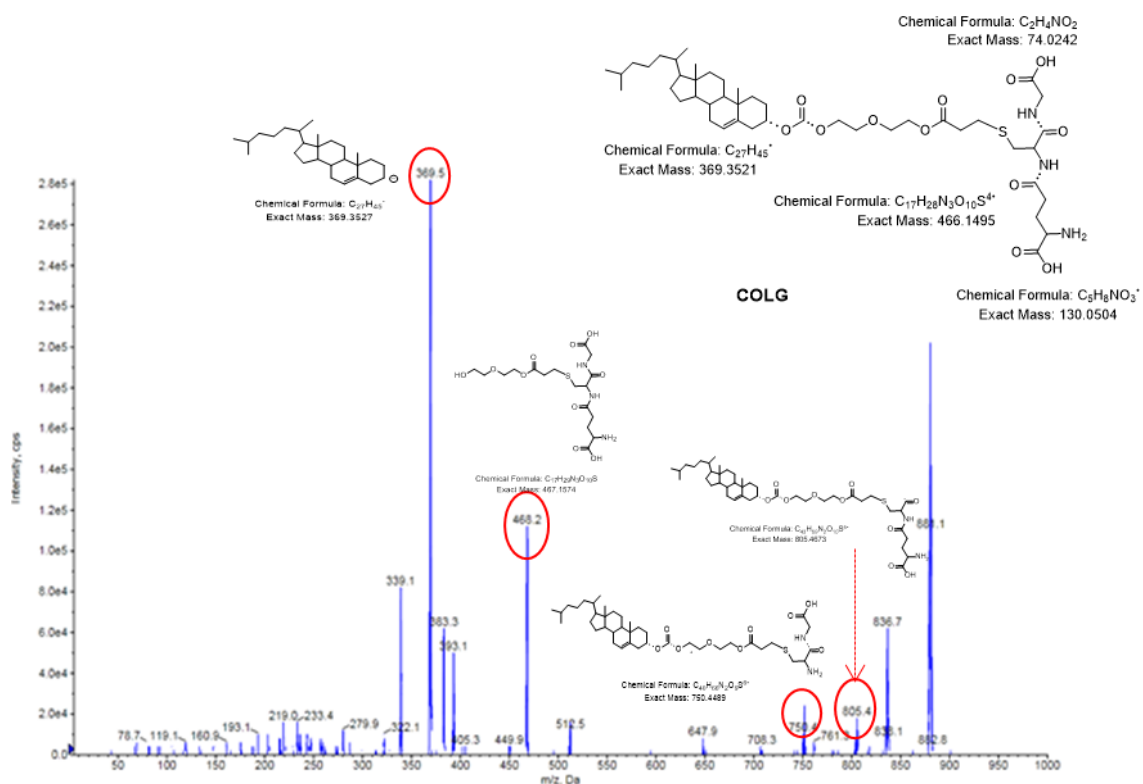


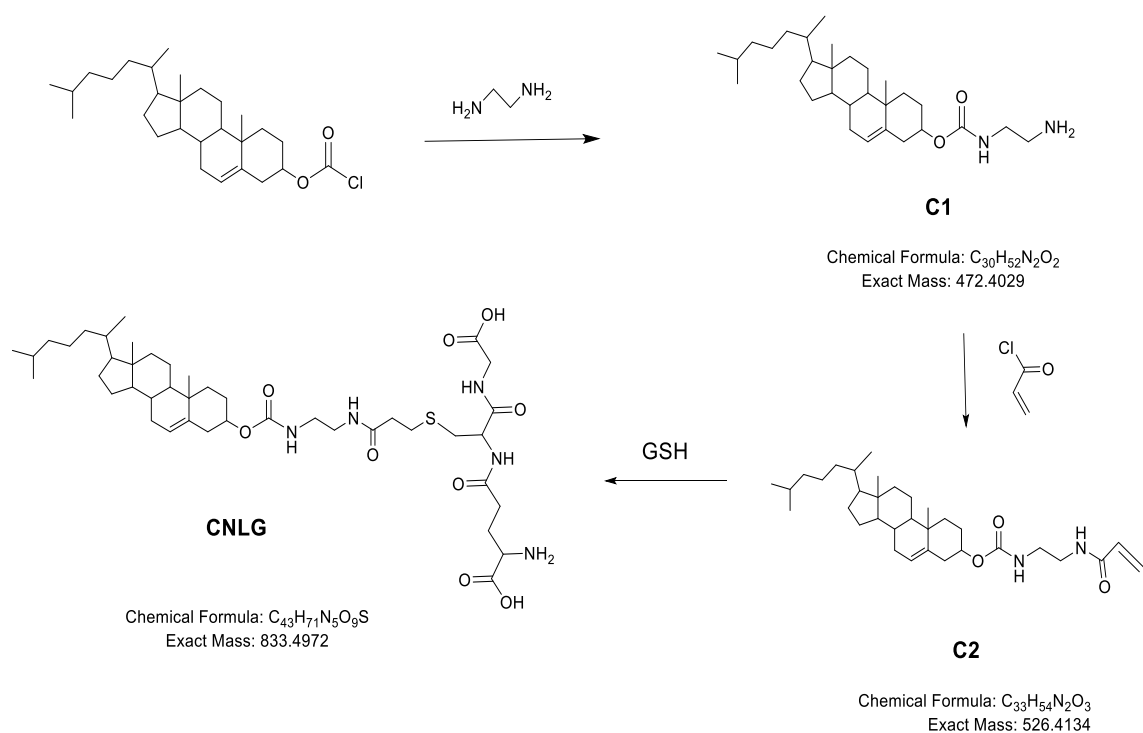
Figure 20. LC/MS/MS spectrum of COLG

### 2.2.1.3 Synthesis and characterization of CNLG

CNLG was synthesized in 3 steps as outlined in Scheme 3. Cholesteryl chloroformate and 1,2-diaminoethane were coupled together to produce cholesterol carbamate (Compound C1) in 62.5% yield in the presence of triethylamine. Then compound C1 reacted with acryloyl chloride at 0 °C to yield compound C2 in 62% yield.

GSH was attached to compound C2 through a Michael addition to yield our final compound (CNLG) in 43% yield with a melting point of 212 °C.

CNLG was characterized by  $^1\text{H}$  NMR, IR and HRMS. The calculated HRMS for protonated CNLG [ $\text{C}_{43}\text{H}_{72}\text{N}_5\text{O}_9\text{S}$  ( $\text{M}+\text{H}$ ) $^+$ ] is 834.504527 and the found 834.5063 (Figure 21). The purity of CNLG was checked by HPLC and found to be >97%.



Scheme 3 Synthesis of CNLG

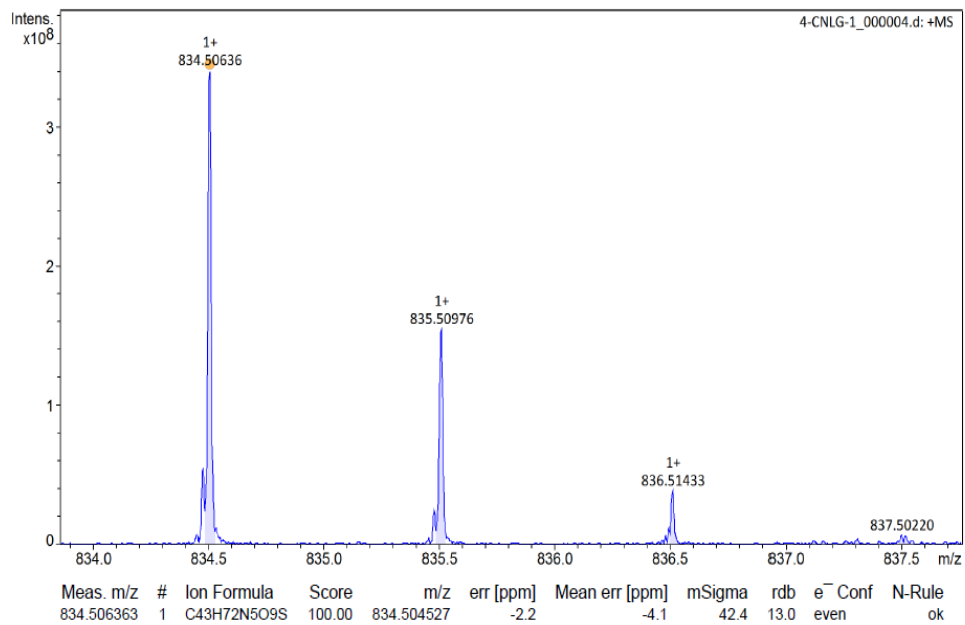


Figure 21. HRMS spectrum of CNLG

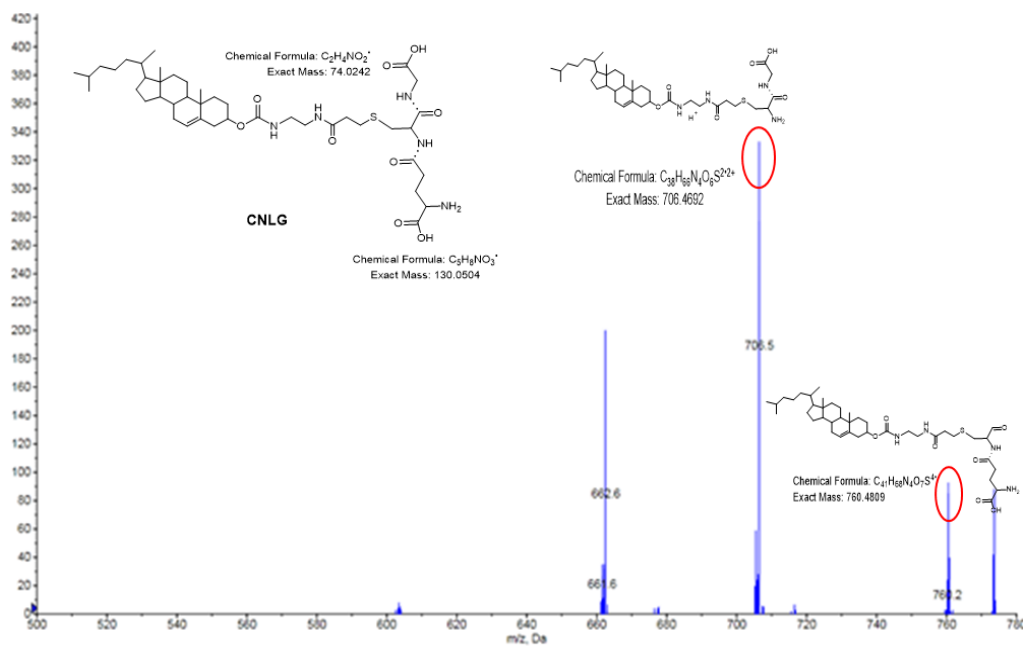


Figure 22. LC/MS/MS spectrum of CNLG

Again, CNLG was confirmed to be the *S*-isomer by the two neutral losses [neutral loss of glycine ( $m/z$  fragment at 760) and neutral loss of pyroglutamate ( $m/z$  fragment at 706)] (Figure 22).

### 2.2.2 CMC determination

The CMC is the minimum concentration for an amphiphilic molecule to form micelles. It is a critical micelle parameter to indicate the stability of micelles upon dilution. To determine CMC, the pyrene fluorescence method was used [175-177]. Pyrene is a fluorescence molecule that has a poor water solubility and prefers to be in hydrophobic microenvironment. To determine CMC, the fluorescence intensity of pyrene against logarithm of a compound's concentration was plotted.

As shown in Figure 23, at low concentration, a low but constant fluorescence intensity of pyrene was observed by the relatively small change in the value of  $I_3/I_1$ , indicating the molecule existed in a monomer state. However, a dramatic increase in fluorescence intensity of pyrene was observed by the sudden change in the value of  $I_3/I_1$ , indicating CLG, COLG, or CNLG formed micelles and pyrene started to move from water environment to the micelle's hydrophobic core. The concentration at the intersection of the two straight lines of the plot is the CMC value. As indicated in the figure, the CMC values of CLG, COLG and CNLG were determined to be 1.34  $\mu\text{M}$ , 5.70  $\mu\text{M}$ , 6.01  $\mu\text{M}$ , respectively. The low  $\mu\text{M}$  CMC value suggests CLG, COLG and CNLG can remain as micelles when diluted in the blood circulation.

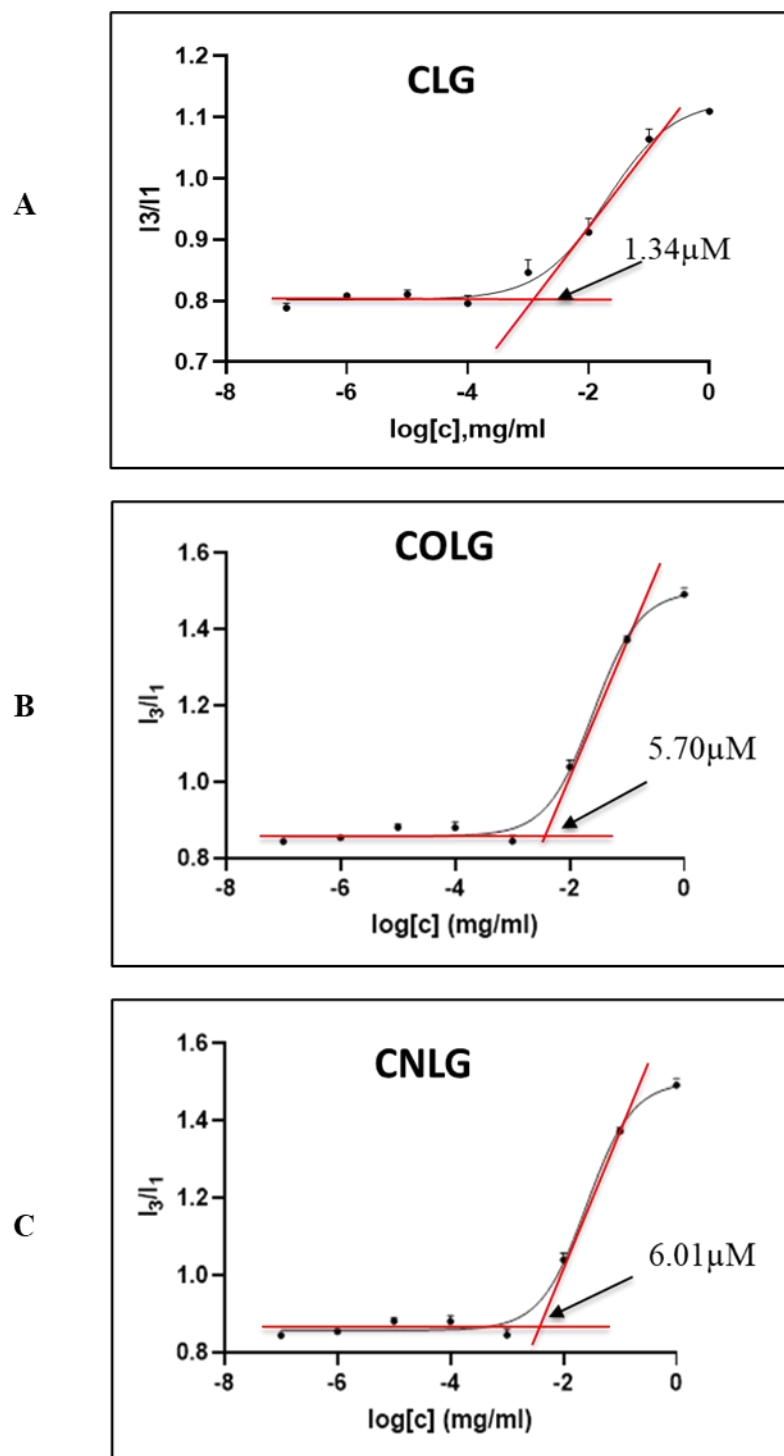


Figure 23. Determination of CMC of (A) CLG micelles; (B) COLG micelles; (C) CNLG micelles. Data are presented as the mean  $\pm$  SD ( $n=3$ ).

### 2.2.3 Preparation of DiR loaded Micelles

To facilitate the brain-targeting investigation, DiR encapsulated micelles of CLG, COLG and CNLG were prepared. DiR is a commonly used near infrared fluorescent hydrophobic carbocyanine dye for determining the *in vivo* tissue distribution of nanoparticles [178-181].

#### 2.2.3.1 Preparation and characterization of DiR loaded micelles

DiR loaded micelles were prepared by a film-dispersion method as demonstrated in Figure 24 [182]. Briefly, CLG, COLG or CNLG and DiR were dissolved in ethanol, followed by evaporation of ethanol under a stream of nitrogen. The residue was hydrated with DPBS, then centrifuged to remove insoluble DiR to produce DiR loaded micelles.

The particle size, zeta potential, size distribution, encapsulation efficiency (EE%) (the amount of drug loaded in the nanoparticles/the amount of drug used for encapsulation) and loading capacity (LC%) (the amount of drug loaded in the nanoparticles/nanoparticle weight) are all key parameters needed for micelle characterization and presented in Table 6.

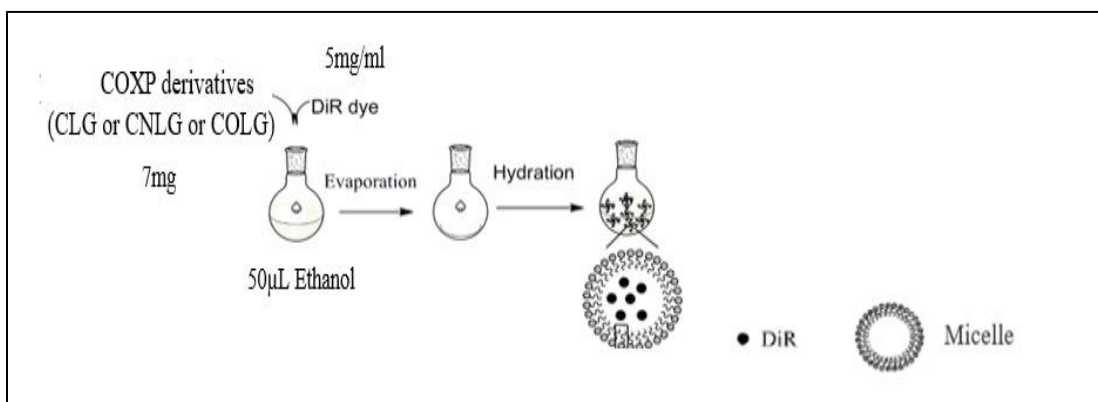


Figure 24. Preparation of DiR loaded micelles

As illustrate in Table 6-I, the average particle sizes of DiR loaded CLG micelles, DiR loaded COLG micelles and DiR loaded CNLG micelles were determined to be  $36.18 \pm 3.05$  nm (n=3),  $63.64 \pm 0.89$  nm (n=3) and  $61.99 \pm 1.00$  nm (n=3) with PDI values of  $0.32 \pm 0.01$  nm,  $0.24 \pm 0.07$  nm and  $0.29 \pm 0.02$  nm respectively. The particle sizes of the three micelles were all well below 150 nm, which is preferred for brain targeting. The lower PDI values suggest a narrow size distribution of DiR loaded micelles. The zeta potential of DiR loaded CLG micelles, DiR loaded COLG micelles, and DiR loaded CNLG micelles were determined to be  $-43.3 \pm 9.84$  mV (n=3),  $-51.3 \pm 2.25$  mV (n=3), and  $-46.36 \pm 1.19$  mV (n=3), confirming that these micelles carry a negative surface charge suggesting the negatively charged GSH molecule is on the surface of the micelles.

The EE% of DiR loaded CLG micelles, DiR loaded COLG micelles and DiR loaded CNLG micelles were determined to be  $94.91 \pm 0.01\%$  (n=3),  $97.60 \pm 0.01\%$  (n=3), and  $95.56 \pm 0.84\%$  (n=3) with the LC% to be  $0.33 \pm 0.0019\%$ ,  $0.34 \pm 0.0017\%$  and  $0.33 \pm 0.0019\%$ , respectively (Table 6-II), indicating DiR was successfully encapsulated into the hydrophobic core of these derivatives.

Table 6 Characterization of DiR loaded micelles

**I**

Preparation	Size (nm)	PDI	Zeta potential (mV)
DiR loaded CLG micelles	36.18±3.05	0.32±0.01	-43.3±9.84
DiR loaded COLG micelles	63.64±0.89	0.24±0.07	-51.3±2.25
DiR loaded CNLG micelles	61.99±1.00	0.29±0.02	-46.36±1.19

**II**

Preparation	Theoretical loading (%)	EE (%)	LC (%)
DiR loaded CLG micelles	0.35	94.91±0.01	0.33±0.0019
DiR loaded COLG micelles	0.35	97.60±0.01	0.34±0.0017
DiR loaded CNLG micelles	0.35	95.56±0.84	0.34±0.0030

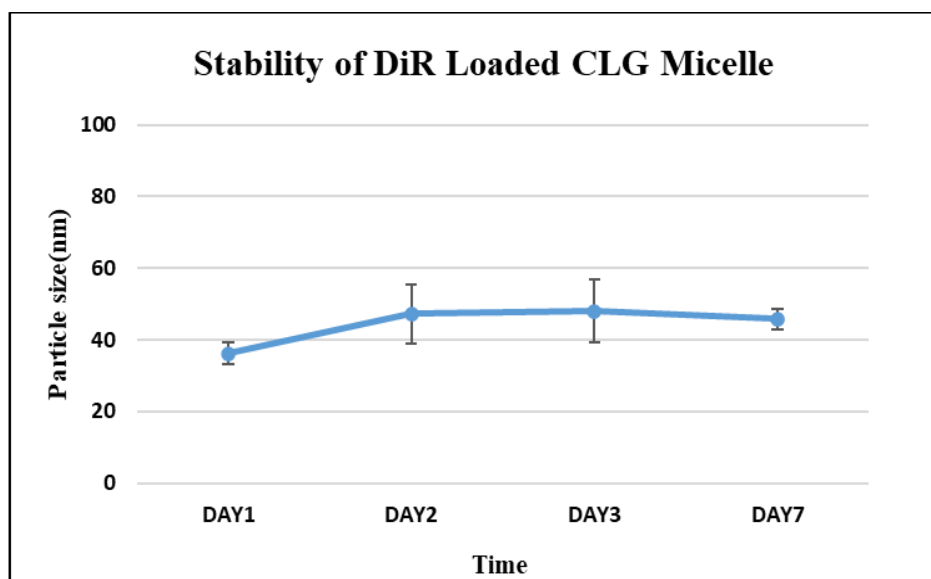
*Data are presented as mean ± SD (n=3).*

### 2.2.3.2 Storage stability of DiR loaded micelles

The storage stability of DiR loaded micelles was checked by the changes in micellar particle size at 4 °C on day 0, day 1, day 2, day 3, and day 7. The data are shown in Figure 25.

For DiR loaded CLG micelles (Figure 25-A), the particle size on day 1 was  $36.1 \pm 3.06$  nm vs  $45.8 \pm 2.84$  nm on day 7. No significant differences in particle size ( $P = 0.164$ , one-way anova) were observed between days. For DiR loaded COLG micelles (Figure 25-B), there is a slight increase in particle size between days with particle size  $63.6 \pm 0.89$  nm on day 1 vs particle size  $66.3 \pm 1.22$  nm on day 7. For DiR loaded CNLG micelles (Figure 25-C), the particle size on day 1 was  $61.9 \pm 1.00$  nm vs  $68.9 \pm 1.76$  nm on day 7, no significant difference in particle size ( $P = 0.756$ , one-way anova) between days was observed.

A



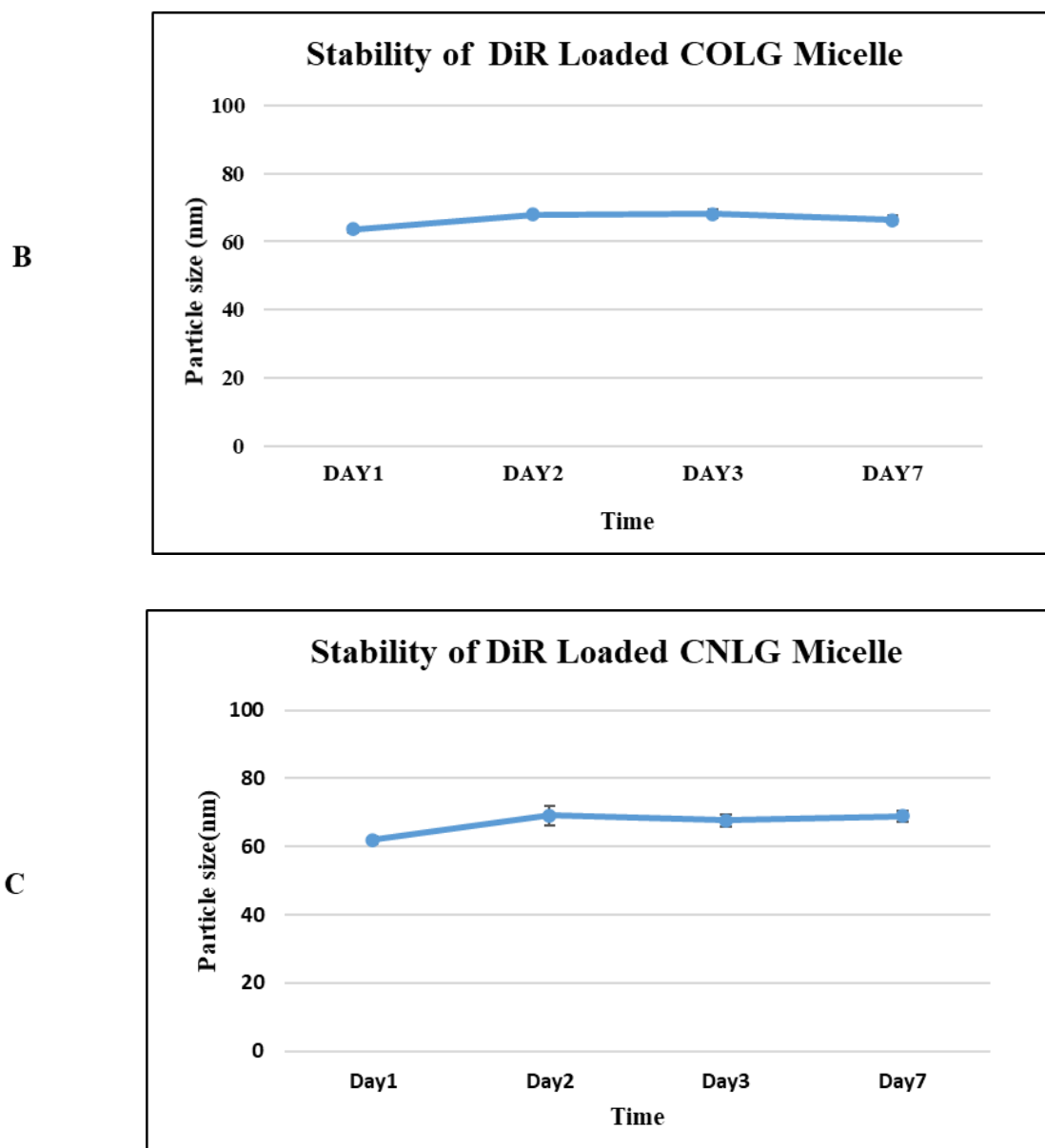


Figure 25. Stability of (A) DiR loaded CLG micelles; (B) DiR loaded COLG micelles; (C) DiR loaded CNLG micelles during 7 days' storage at 4°C. Data are presented as mean  $\pm$  SD ( $n=3$ ).

### 2.2.3.3 Evaluation of brain-targeting effects through *ex-vivo* imaging of brain

To help evaluate the brain targeting effect, *ex-vivo* imaging of the isolated brains were carried out. Figure 26 shows representative fluorescence images and the corresponding fluorescence intensities of the isolated brain from mice (n=1/group) after a 2 h-treatment with free DiR, DiR loaded CLG micelles, DiR loaded COLG micelles, and DiR loaded CNLG micelles. The brains were collected after heart perfusion with DPBS to remove blood in tissues.

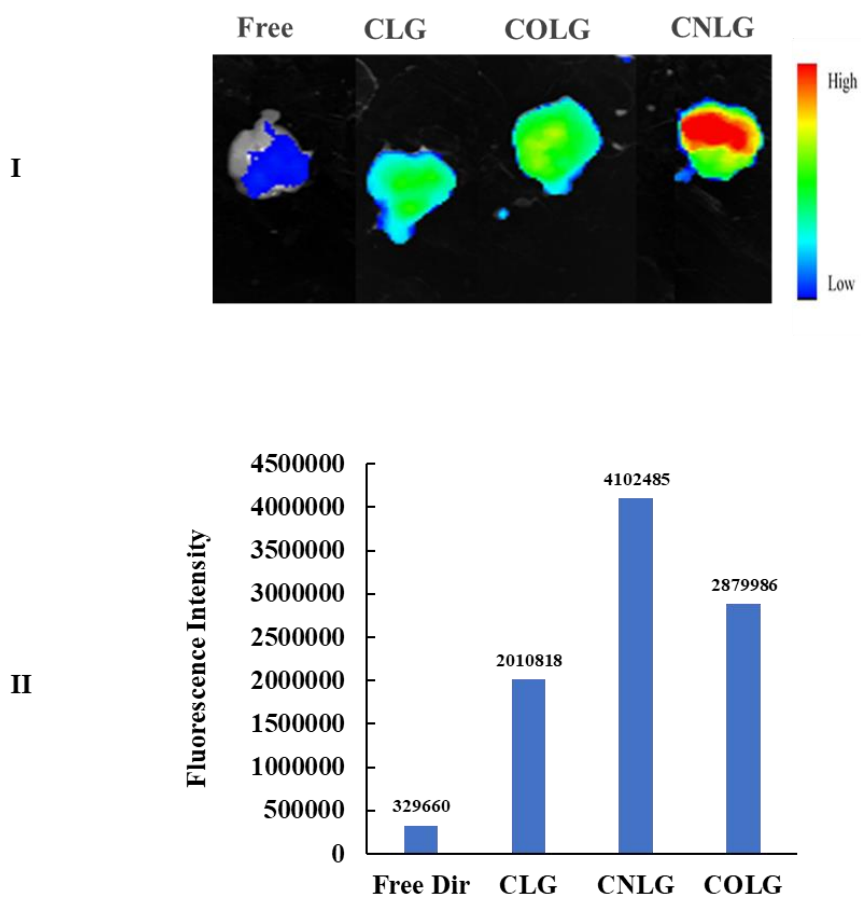


Figure 26. Representative *ex-vivo* images (**I**) and corresponding fluorescence intensities (**II**) of the mouse brains 2 h after i.v injection of Free DiR (n=1); CLG DiR micelle (n=1); COLG DiR micelle (n=1); CNLG DiR micelles (n=1)

Compared with brains from the mice treated with free DiR, the fluorescence intensities were significantly higher from the brains of the mice treated with DiR loaded micelles with the highest fluorescence intensity from the brain of the mice treated with DiR loaded CNLG micelles. No statistical analysis has been conducted since only 1 mice is available for each treatment group.

The *ex-vivo* fluorescence images of the brains confirmed that CLG, CNLG and COLG micelles were all effective brain-targeting micelles. Since CNLG micelles appears to be the most effective brain targeting micelles of the three, we decided to focus on CNLG micelles for further investigation.

#### **2.2.4 Further investigation of CNLG for a brain targeting drug delivery system**

Since CNLG micelles appeared to be the most effective brain targeting micelles of the three, a further investigation of CNLG as an effective brain targeting drug delivery system was conducted. The further investigation included a cytotoxicity study of CNLG, releasing study using Rhodamine B loaded CNLG micelles and a cell uptake study with Rhodamine B loaded CNLG micelles. Finally, the brain targeting effect was investigated with DiR loaded CNLG micelles in mice using the whole-body fluorescence imaging technique and *ex-vivo* fluorescence imaging of the brains.

##### **2.2.4.1 *In vitro* cytotoxicity**

The *in vitro* cytotoxicity of CNLG was tested with CV-1 cell line and NCI-H226 cell line through the MTT assay at 24h. Based on the dose-response curves (Figure 27), IC<sub>50</sub> values of CNLG for CV-1 cell line and NCI-H226 cell line were 49  $\mu$ M and 63.56  $\mu$ M, respectively. The IC<sub>50</sub> values are much higher than the CMC value (3.9  $\mu$ M) of

CNLG suggesting that CNLG could be used as a safe carrier for brain-targeting drug delivery.

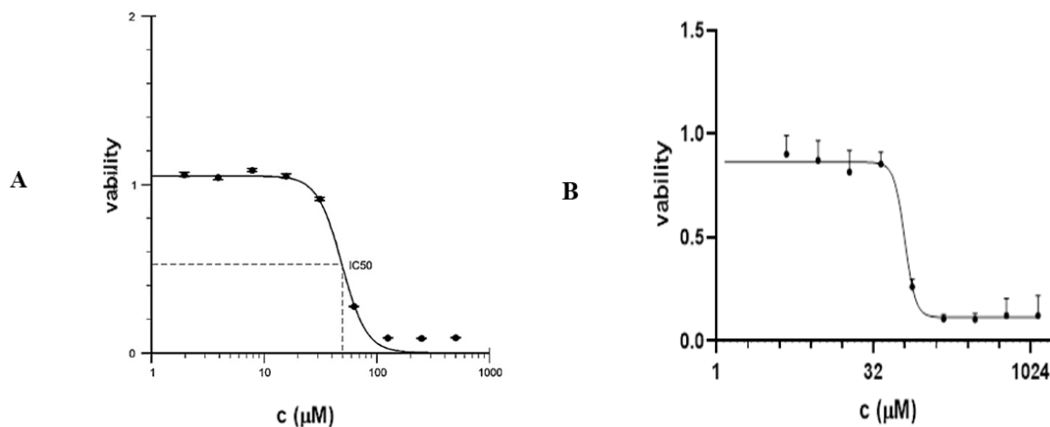


Figure 27. Dose-response curves for the determination of  $IC_{50}$  values of CNLG with (A) CV-1 cell line, (B) NCI-H226 cell line. Data are presented as the mean  $\pm$  SD ( $n=3$ ).

#### 2.2.4.2 Rhodamine B *in vitro* release study

The release study was conducted with Rhodamine B loaded CNLG micelles by a dialysis method with PBS (pH 7.4) or citric acid buffer (pH 4.5) as the release medium. The reason to use Rhodamine B not DiR was based on the sensitivity. The near infrared dyes DiR was poorly detected by HPLC with a UV/Vis detector. Considering both Rhodamine B and DiR are hydrophobic cationic dyes and Rhodamine B has been reported to replace DiR for *in vitro* studies for the same reason [183], Rhodamine B was chosen for the *in vitro* release study.

As shown in Figure 28, the majority of Rhodamine B in the control experiment where free Rhodamine B was used was detected in either pH 7.4 dialysis buffer or pH 4.5 dialysis buffer within 1h. In contrast, only about 20% of Rhodamine B was released from CNLG micelles in either pH 7.4 dialysis buffer or pH 4.5 dialysis buffer in ~4 h. After 48

h, nearly 80% of Rhodamine B was released from CNLG micelles in pH 4.5 dialysis buffer while only 35% of Rhodamine B was released from CNLG micelles in pH 7.4 dialysis buffer.

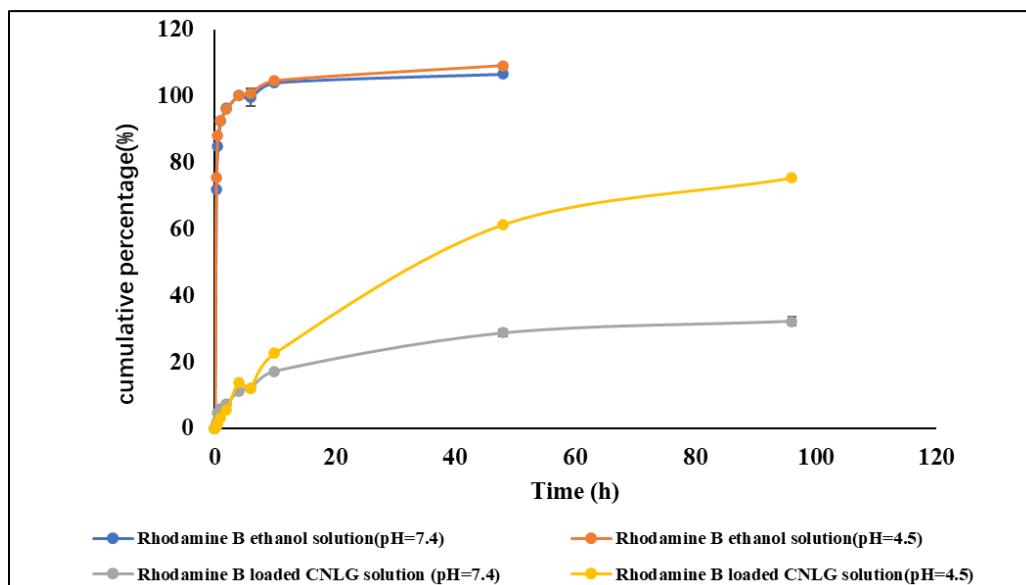


Figure 28. Release of Rhodamine B from Rhodamine B loaded CNLG micelles with Rhodamine B ethanol solution as a control in PBS buffer (pH 7.4) or citric acid buffer (pH 4.5). Data are presented as mean  $\pm$  SD ( $n=3$ ).

The results from the release study indicated that CNLG micelles showed a slow-release profile compared with free Rhodamine B solution. It is worth noting that CNLG micelles also showed a pH-sensitive release profile since more release was observed in pH 4.5 dialysis buffer than in pH 7.4 dialysis buffer.

#### 2.2.4.3 Cellular uptake of Rhodamine B loaded CNLG micelles

The cell uptake study was aimed to determine if CNLG micelles were taken by cells through a GSH transporter. As discussed earlier, the tissue other than the brain which is rich with GSH transporters is kidneys. The Madin Darby canine kidney

(MDCK II) cell line has already been used to confirm the cell uptake by GSH transporters for prodrugs[184]. In this experiment, we employed mouse kidney cells. The reason we used Rhodamine B loaded micelles instead of DiR loaded micelles is for the same reason described in the release study (section 2.2.4.2)

As shown in Figure 29, Rhodamine B loaded CNLG micelles were able to be taken by the kidney cells. We also used probenecid – a literature reported compound used to demonstrate an inhibition of GSH transporters, since GSH transporter is organic anion transporter and probenecid is reported as inhibitor of organic anion transporter [185]. As shown in the figure, about 50% of cell uptake inhibition was observed in the presence of 1mM probenecid consistent with the observed inhibition in the literature[186]. The cell uptake study supports that CNLG micelles were taken into cells through a GSH transporter-mediated process.

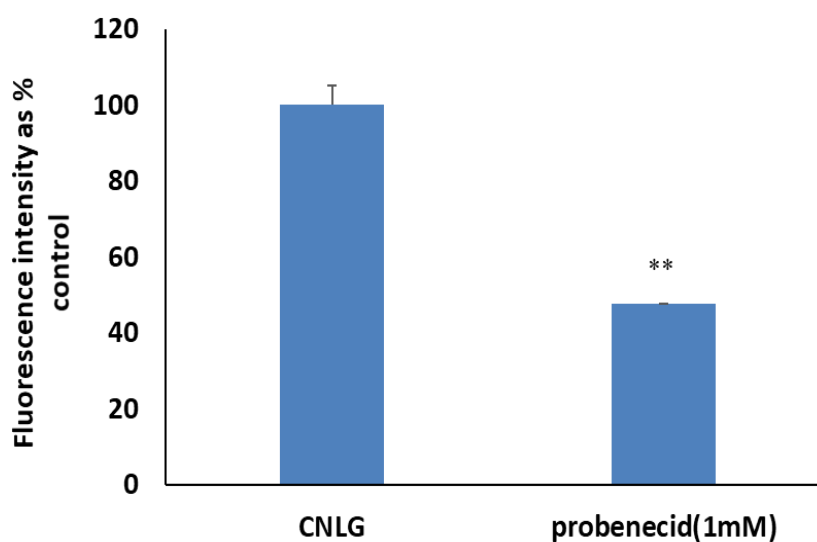


Figure 29. Cell uptake and uptake inhibition by probenecid of Rhodamine B loaded CNLG micelles in mouse kidney cells. *The data are expressed as a percentage of control (n = 3, P < 0.01\*\*, Student's t-test).*

#### 2.2.4.4 Whole-body fluorescence imaging of mice

Whole-body imaging of mice treated with DiR loaded CNLG micelles was conducted at different time points (15 min, 30 min, 1 h, 2 h, 4 h, 6h, 12 h, and 24 h) to check the brain targeting effect of CNLG micelles. Free DiR was employed as a control. Pixel quantification of the region of interest was obtained for comparison.

As demonstrated in Figure 30, DiR loaded CNLG micelles distributed rapidly to the brain within 15 min. The fluorescence intensity remained strong in brain even at 24 h confirming DiR loaded CNLG micelles could be retained in the brain for 24 h. In contrast, detectable but not significant fluorescence intensity was observed in the brain of the mice treated with free DiR consistent with the poor ability of DiR to pass the BBB.

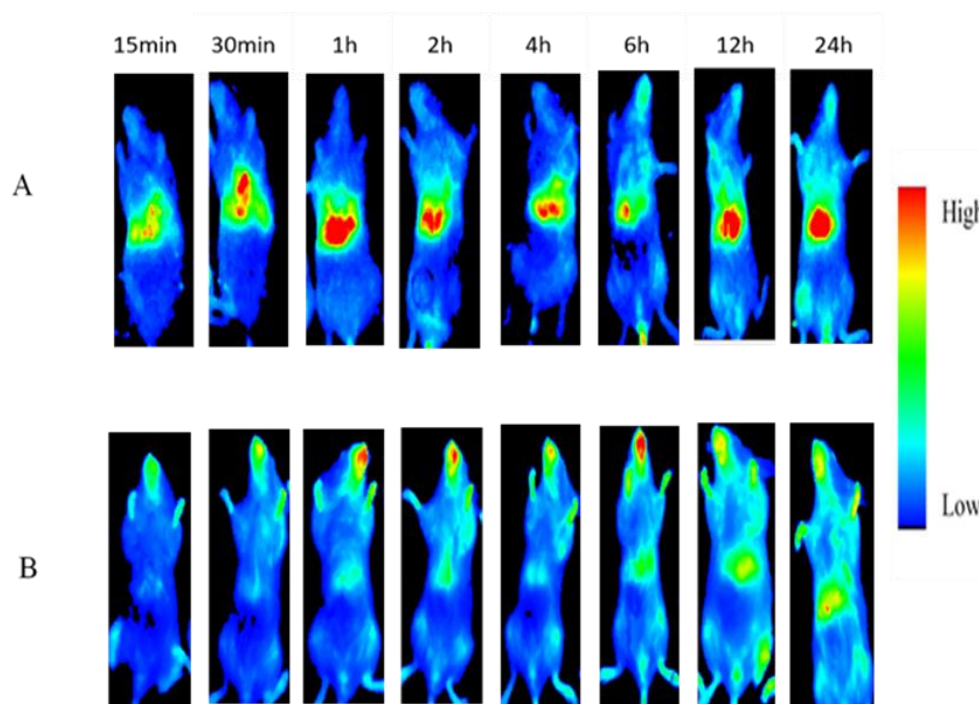


Figure 30. Whole-body fluorescence imaging of mice after i.v injection of free DiR (A) and DiR loaded CNLG micelles (B).

Figure 31. shows the fluorescence intensity obtained from the brains of the whole-body images. An average of more than 39-fold increase in brain distribution was observed for DiR delivered by CNLG micelles when compared with free DiR within the first 2h after injection. However, after 2h, the average increase in fluorescence intensity from brain treated with CNLG micelles was ~25-fold compared with that treated with free DiR. The drop in brain targeting after 2h was likely due to an increase in free DiR in the brain (Figure 31).

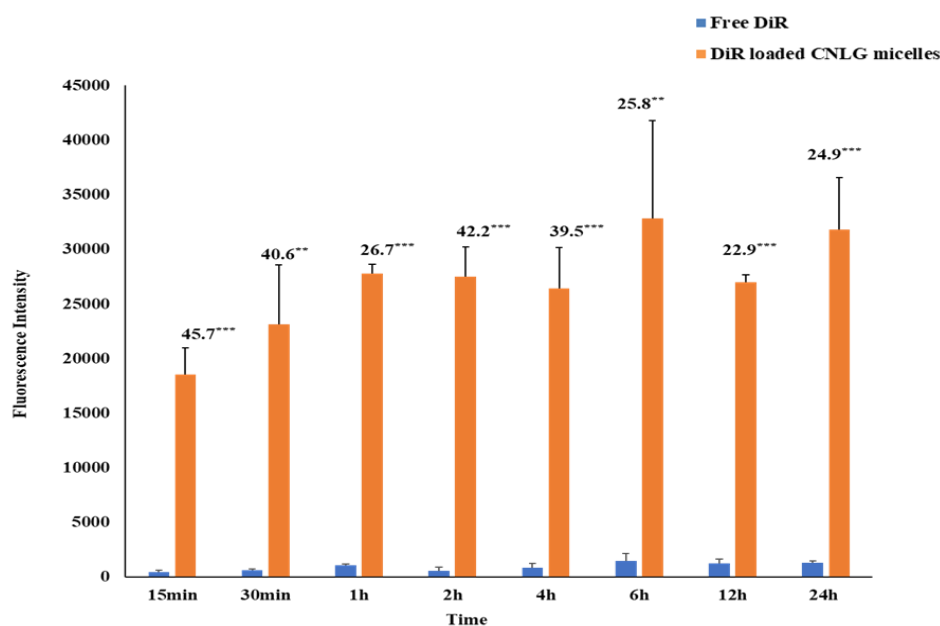


Figure 31. Brain fluorescence intensities from the whole-body imaging. *Results are presented as mean  $\pm$  SD (n=3).  $P < 0.01$  \*\*;  $P < 0.001$ \*\*\**

#### 2.2.4.5 *Ex-vivo* fluorescence imaging

It is known that the fluorescence intensity obtained through whole-body imaging can be affected by various factors though whole-body imaging has been used commonly in evaluating brain-targeting effects in the literature[187-190]. In this section, the *ex-vivo*

imaging technique was employed to confirm the brain targeting effect as well as tissue distribution of DiR loaded CNLG micelles. The brain and other tissues (heart, lung, liver, spleen, and kidney) from mice treated with free DiR (control) or DiR loaded CNLG micelles after 2 h were collected for *ex-vivo* imaging.

#### **2.2.4.5.1 Brain *ex-vivo* imaging**

The fluorescence images of the isolated brains with a treatment for 2 h showed that the fluorescence intensity was significantly higher (8.9 fold,  $P = 0.009$ , Student's t-test) from the brain of the mice treated with DiR loaded CNLG micelles when compared with free DiR (Figure 32). The increase was significantly lower than the increase obtained from the whole-body imaging. It is not clear why the increase obtained from *ex-vivo* imaging was lower than that from the whole-body imaging.

#### **2.2.4.5.2 *Ex-vivo* imaging of organs other than brain**

In addition to brain distribution, tissue distribution in other major organs (heart, lung, liver, spleen, and kidney) at 2 h was also investigated. The results are presented in Figure 33.

As shown in the Figure 33-I, free DiR distributed mainly to the lungs, spleen and liver with a high accumulation in the lungs. A minimum distribution of DiR in the heart and kidney was observed with free DiR. In contrast, CNLG micelles appear to distribute to the heart, lungs, liver, and kidneys with the highest accumulation in the liver. A high distribution in the liver was consistent with the tissue distribution behavior of nanoparticles since nanoparticles can be easily taken by phagocytes in the liver [191]. A relative high distribution in kidneys was observed that was consistent with the rich existence of GSH transporter in kidneys [151]. In addition, the total fluorescence

intensity from the collected organs appears to be stronger from the mice treated with DiR loaded CNLG micelles compared with free DiR (Figure 33-II).

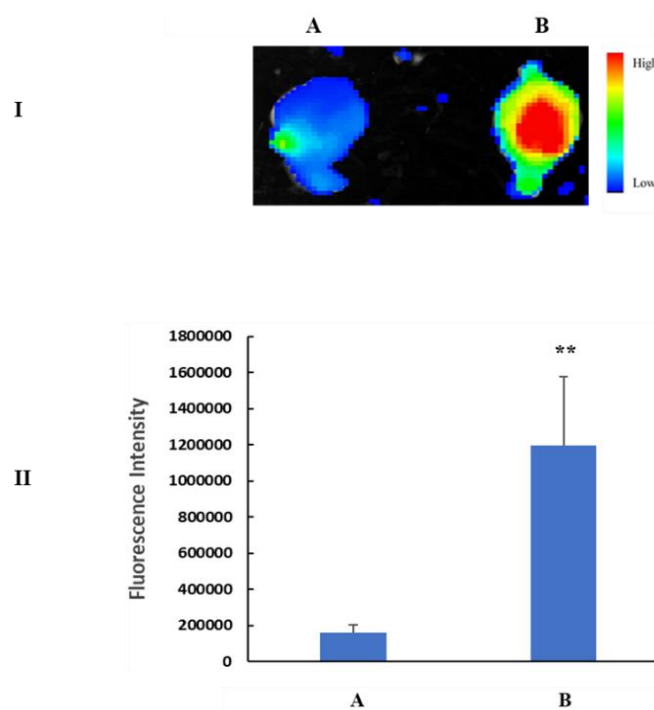


Figure 32. Representative ex-vivo images (I) and corresponding fluorescence intensities (II) of the mouse brains 2 h after i.v injection of free DiR (A), DiR loaded CNLG micelles (B). Results are presented as mean  $\pm$  SD (n=3). P < 0.01\*\*

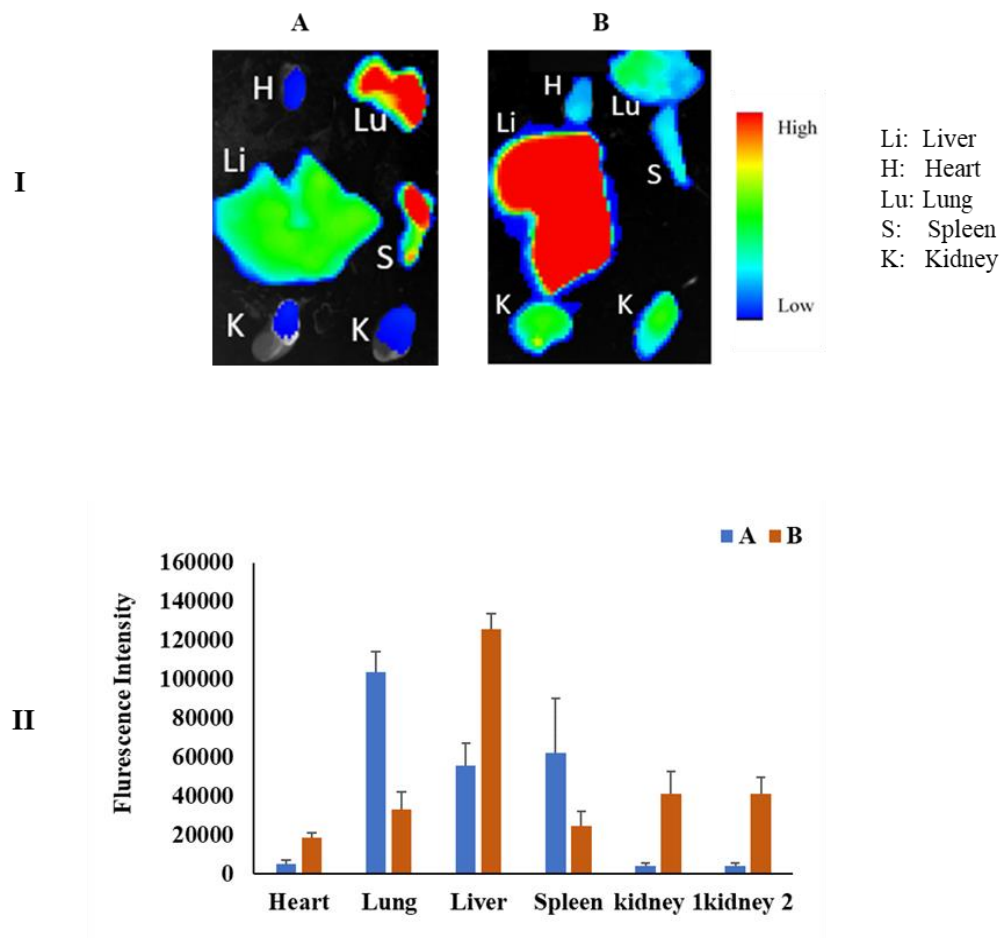


Figure 33. Representative *ex-vivo* images (I) and corresponding fluorescence intensities (II) of the organs 2 h after i.v injection of free DiR (A) or DiR loaded CNLG micelles (B). Results are presented as mean  $\pm$  SD ( $n=3$ ).

### 2.2.5 Conclusion

In this study, we demonstrated that COXP derivatives derived from the replacement of the linker in COXP with other linkers still led to effective brain targeting molecules which can undergo self-assemble to form brain targeting micelles. The micelles formed from the most effective brain targeting molecule CNLG exhibited better brain targeting effect than COXP micelles. CNLG micelles could deliver approximately 40 times more DiR to the brain compared with free DiR based on the whole-body

imaging and ~8.9 folds more based the *ex-vivo* imaging vs ~20 times more with the whole-body imaging and ~8 fold more based on *ex-vivo* imaging for COXP micelles. Our study suggests that replacement of the linker of COXP can be an effective structural modification to identify better brain targeting agents and better brain targeting micelles.

## **2.3 Methods**

### **2.3.1 Chemicals and materials**

Unless otherwise stated, all chemical reagents and solvents were obtained from commercial sources and used without further purification.

Cholesteryl chloroformate, 1,2-diaminoethane, triethylamine, pyridine, ethylene glycol, acryloyl chloride, and GSH were acquired from Fisher Scientific (Waltham, MA, USA). *P*-Toluenesulfonyl chloride, dioxane, dichloromethane, tetrahydrofuran, ethyl acetate, hexanes were purchased from Sigma-Aldrich (St. Louis, MO, USA).

RPMI 1640 growth medium supplemented with 10% FBS and 100 units/mL of penicillin was obtained from Mediatech, Inc. (Hendon, VA). DMEM growth medium supplemented with 10% FBS and 1% penicillin-streptomycin and Dulbecco's phosphate buffer saline (Gibco™ DPBS, without calcium and magnesium, 1x), DiR, ethanol, tetrahydrofuran (THF), and Rhodamine were purchased from Fisher Scientific (Waltham, MA, USA). Pyrene were obtained from Lipoid (Ludwigshafen, Germany).

Silica gel column (mesh 200-400) was obtained from Oakwood products, Inc (West Columbia, SC, USA).

### 2.3.2 Instrumentation

Flash column chromatography was carried out on a W-Prep 2 XY Yamazen Dual channel flush chromatography system (San Bruno, California).

$^1\text{H}$  NMR spectra were obtained from Bruker Varian 600 MHz spectrometer in deuterated solvents as indicated. All peaks were given as chemical shift in part per million relatives to TMS (tetramethyl saline) or DSS (4,4-dimethyl-4-silapentane-1-sulfonic acid) as an internal standard. Multiplicities are indicted by s (singlet), d (doublets), t (triplet), q (quartet), m (multiplet), and brs (broad singlet). *J* values are given in Hz.

The low-resolution mass spectra (LRMS) were acquired on Thermoquest Finnigan LCQ Deca mass spectrometer (Waltham, MA, USA) and the high-resolution mass spectra (HRMS) were obtained on a Bruker Daltonics solariX 12 teslas Fourier Transform Ion Cyclotron Resonance mass spectrometer (Department of chemistry, University at Buffalo, NY).

FTIR spectra were obtained on Thermo NICOLET 6700 FT-IR spectrometer (Thermo Fisher Scientific, Madison, WI).

Melting points were recorded on a MEL-TEMP® melting apparatus (Electrothermal, Dubuque, IA).

Cell numbers and cells viability were obtained on a Nexcelom Cellometer Auto T4 Automated Cell Counter (Lawrence, MA, USA).

The particle size and zeta potential of nanoparticles were obtained from Zetasizer (Malvern instrument, Westborough, MA).

Optical properties (absorbance and fluorescence) were obtained on a SpectraMax M2 microplate reader (Molecular Devices, Sunnyvale, California).

*In-vivo* and *ex-vivo* imaging was obtained on a Xtreme *in-vivo* imaging (Bruker).

### 2.3.3 HPLC/MS and LC/MS/MS condition

All HPLC/MS analysis was achieved on an Agilent 1260 infinity II HPLC coupled to Agilent infinity Lab MSD and a 1260 Infinity II Diode Array Detector (DAD) WR. Chromatographic separations were achieved by using Luna 3u C8(2) column (100×4.6 mm i.d., Phenomenex, Torrance, CA). The mobile phase comprised ammonium (pH 10.6) aqueous solution (phase A) and acetonitrile (phase B) at a flow rate of 1 mL/min. Phase B was initially set at 0% for 5 min, increased linearly to 90% over 20 min and held for 3 min, then returned to the initial conditions over 5 min. The system was re-equilibrated for 3 min before the next injection. The autosampler was thermostated at 4 °C. The sample was injected at a volume of 5 µL with a run time of 33 min. The wavelengths 210 nm were employed for UV/vis detection of COXP derivatives (CLG, COLG, CNLG).

The MS detection of CLG, COLG, and CNLG were set up with the selected ion monitoring (SIM) both in negative mode (ESI<sup>-</sup>) and positive mode (ESI<sup>+</sup>). *m/z* 747 (ESI<sup>-</sup>) and *m/z* 748 (ESI<sup>+</sup>) for CLG; *m/z* 878 (ESI<sup>-</sup>) and *m/z* 879 (ESI<sup>+</sup>) for COLG; *m/z* 832 (ESI<sup>-</sup>) and *m/z* 834 (ESI<sup>+</sup>) for CNLG. The following parameters of mass spectrometer in SIM mode were used: capillary voltage, 4 KV; desolvation temperature, 330 °C; nitrogen gas flow rate, 11 L/min; optimized fragmentation voltage, 135 V.

The LC/MS/MS detection of the fragmentation of CNLG, COLG, and CLG were set in the positive mode with the following parameters: capillary voltage, 5.5 KV; desolvation temperature, 330 °C; nitrogen gas flow rate, 11 L/min; optimized

fragmentation voltage, 135V; collision energy, 30V. The parent ion for CLG, COLG, CNLG is  $m/z$  748,  $m/z$  879, and  $m/z$  834, respectively.

#### **2.3.4 Cells and animals**

NCI-H226 cell line (human lung cancer cell line) and CV-1 cells (African green monkey kidney fibroblast cell line) were obtained from the National Cancer Institute and American Type Culture Collection (ATCC) respectively. The cells were cultured in RPMI 1640 growth medium with 10% FBS and 1% penicillin/streptomycin in a humidified atmosphere and 5% CO<sub>2</sub> at 37 °C.

Females BALB/Cj mice (6-8 weeks old, 17-20 g) and females BALB/Cj mice (2 weeks, 16 g) were purchased from Jackson Laboratory (Bar Harbor, ME, USA) and acclimatized to a laboratory condition for one week before the experiment. All animal process were performed following the protocol approved by the Institutional Animal Care and Use Committee (IACUC) at South Dakota State University Brookings, SD, USA.

Mouse kidney cells were isolated from females BALB/Cj mice (2 weeks, 16 g) followed the procedure described in the literature [186, 192-194]. Cells were maintained in a DMEM growth medium supplement with 10% FBS and 1% penicillin-streptomycin in a 5% CO<sub>2</sub> incubator at 37 °C.

#### **2.3.5 Synthesis of COXP derivatives (CLG, COLG, CNLG)**

##### **2.3.5.1 Synthesis of CLG**

- i. Synthesis of 10,13-dimethyl-17-(6-methylheptan-2-yl)-2,3,4,7,8,9,10,11,12,13,14,15,16,17-tetradecahydro-1H-cyclopenta[a]phenanthren-3-yl acrylate (Scheme 1, compound A1)*

To a stirred solution of cholesterol (2 g, 5.18 mmol) in anhydrous dichloromethane (30 mL) with triethylamine (1.18 mL) was added dropwise acryloyl chloride (0.64 mL, 7.8 mmol), the mixtures were allowed to react for 60 min before solvent removal under a reduced pressure. A silica gel column (silica size 200-400 mesh) was used to purify the compound with hexanes/ethyl acetate to yield white power product (1.2 g, 52 %). The compound was characterized by  $^1\text{H}$  NMR (600 MHz,  $\text{CDCl}_3$ )  $\delta$  6.38 (d,  $J = 17.3$  Hz, 1H), 6.09 (dd,  $J = 17.3, 10.4$  Hz, 1H), 5.78 (d,  $J = 10.4$  Hz, 1H), 5.39 (s, 1H), 4.68 (dd,  $J = 10.1, 4.6$  Hz, 1H), 2.49 – 2.30 (m, 2H), 2.05 – 1.80 (m, 4H), 1.67 – 0.84 (m, 32H), 0.76 – 0.57 (m, 3H).

ii. *Synthesis of N5-(1-((carboxymethyl)amino)-3-((3-((10,13-dimethyl -17-(6-methylheptan-2-yl)-2,3,4,7,8,9,10,11,12,13,14,15,16,17-tetradecahydro-1H-cyclopenta[a]phenanthren-3-yl) oxy)-3-oxopropyl) thiol)-1-oxopropan-2-yl) glutamine (Scheme 1, compound CLG)*

GSH (0.520 g, 1.68 mmol) and sodium carbonate (0.177 g, 1.68 mmol) were dissolved in 6 mL water before being added to a stirred solution of compound A1 (0.5 g, 1.13 mmol) in tetrahydrofuran (7 mL). The reaction was stirred at room temperature for 4 h and 40 °C for additional 3 h under the protection of argon. Formic acid was added to the mixture to precipitate the crude CLG after the reaction was completed. CLG was further purified by rinsing with ethyl acetate three times. The purified CLG was lyophilized to dry to yield white power in 48% yield. The melting point was determined by a MEL-TEMP® melting apparatus. CLG were characterized by IR, MS, HRMS.

### 2.3.5.2 Synthesis of COLG

- i. *Synthesis of 10,13-dimethyl-17-(6-methylheptan-2-yl)-2,3,4,7, 8,9,10,11, 12,13,14, 15,16,17-tetradecahydro-1H-cyclopenta[a]phenanthren-3-yl (2-(2-hydroxyethoxy)ethyl) carbonate (Scheme 2, compound B1)*

Cholesteryl chloroformate (1g, 2.2 mmol), triethylamine (0.9 mL) and diethylene glycol (3.498 g, 33 mmol) were mixed in anhydrous dichloromethane (30 mL). The reaction was allowed to react at room temperature overnight before solvent removal under a pressured rotary evaporator. The residual was purified through a silica gel column (silica size 200-400 mesh) with hexanes/ethyl acetate to produce a white product in a yield of 70%. The product was used for next step without further characterization.

- ii. *Synthesis of 2-(2-(((10,13-dimethyl-17-(6-methylheptan-2-yl)-2,3,4,7,8,9, 10,11,12,13,14,15,16,17-tetradecahydro-1H-cyclopenta[a]phenanthren-3-yl)oxy) carbonyl)oxy)ethoxy)ethyl acrylate (Scheme 2, compound B2)*

Acryloyl chloride (0.412 mL, 5.2 mmol) was added dropwise to a stirred solution of compound B1 (0.7 g, 1.35 mmol) in anhydrous dichloromethane (30 mL). Triethylamine (0.5 mL) was added, and the reaction was kept at 0 °C for 1.5 h before solvent removal using a rotary evaporator under reduced pressure. The residual was purified by a silica gel column (size 200-400 mesh) with hexanes/ethyl acetate to yield a colorless oily product ( 33%), the compound was characterized by <sup>1</sup>H NMR (600 MHz, CDCl<sub>3</sub>) δ 6.43 (dd, J = 17.3, 1.4 Hz, 1H), 6.16 (dd, J = 17.3, 10.4 Hz, 1H), 5.84 (dd, J = 10.4, 1.4 Hz, 1H), 5.44 – 5.31 (m, 1H), 4.48 (ddd, J = 16.5, 11.1, 5.2 Hz, 1H), 4.35 – 4.25

(m, 4H), 3.80 – 3.68 (m, 4H), 2.46 – 2.35 (m, 2H), 2.04 – 1.78 (m, 6H), 1.59 – 1.00 (m, 23H), 0.92 (t, J = 5.9 Hz, 3H), 0.89 – 0.84 (m, 6H), 0.68 (s, 3H).

iii. *Synthesis of 19-amino-14-((carboxymethyl)carbamoyl)-1-((10,13-dimethyl-17-(6-methylheptan-2-yl)-2,3,4,7,8,9,10,11,12,13,14,15,16,17-tetradecahydro-1H-cyclopentane[a]phenanthren-3-yl)oxy)-1,9,16-trioxo-2,5,8-trioxa-12-thia-15-zaicosan-20-oic acid (Scheme 2, compound COLG)*

GSH (0.147 g, 0.48 mmol), sodium carbonate (0.051 g, 0.48 mmol), and B2 (0.23 g, 0.40 mmol) were mixed in a mixed solvent of tetrahydrofuran (14 mL) and water (12 mL). The reaction was kept at room temperature for six hours followed by addition of excessive formic acid water (1%, v/v) to precipitate crude COLG. COLG was further purified by rinsing three times with formic acid water (1%, v/v) followed by washing with ethyl acetate three times. The precipitation was dried via lyophilization to yield white power in 58% yield. The melting point was determined by a MEL-TEMP® melting apparatus. The compound was fully characterized by FTIR, LRMS, and HRMS.

### 2.3.5.3 Synthesis of CNLG

i. *Synthesis of 10,13-dimethyl-17-(6-methylheptan-2-yl)-2,3,4,7,8,9,10,11,12,13,14,15,16,17-tetradecahydro-1H-cyclopenta[a]phenanthren-3-yl (2-aminoethyl)carbamate (Scheme 3, compound C1)*

To a stirred solution of 1,2-diaminoethane (4.45 mL, 66 mmol) in anhydrous dichloromethane (30 mL) was added dropwise cholesteryl chloroformate (2 g, 4.4 mmol) in 30 mL anhydrous dichloromethane and triethylamine (1.22 mL). The mixtures were allowed to react at 0 °C for 1 h before solvent removal using a rotary evaporator under a

reduce pressure. The residuals were loaded onto a silica gel column (silica size: mesh 200-400) for purification by hexanes/ethyl acetate to yield white power in 62.5%. The compound was fully characterized by  $^1\text{H}$  NMR (600 MHz,  $\text{CDCl}_3$ )  $\delta$  5.45 – 5.30 (m, 1H), 5.12 (d,  $J = 33.7$  Hz, 1H), 4.53-4.45 (m, 1H), 3.22 (d,  $J = 5.4$  Hz, 2H), 2.81 (t,  $J = 5.8$  Hz, 2H), 2.42 – 2.22 (m, 2H), 2.06 – 1.92 (m, 2H), 1.93 – 1.78 (m, 3H), 1.59 – 0.99 (m, 24H), 0.91 (d,  $J = 6.5$  Hz, 3H), 0.86 (dd,  $J = 6.6, 2.7$  Hz, 6H), 0.68 (s, 3H).

ii. *Synthesis of 10,13-dimethyl-17-(6-methylheptan-2-yl)-2,3,4,7,8,9,10,11, 12, 13,14,15,16,17-tetradecahydro-1H-cyclopenta[a]phenanthren-3-yl(2-acrylamidoethyl)carbamate (Scheme 3, compound C2)*

Acryloyl chloride (0.233 mL, 3 mmol) were dissolved in 15 mL anhydrous dichloromethane and stirred at  $0^\circ\text{C}$  for 20 min before adding compound C1 (0.7 g, 1.5 mmol) in 15 mL anhydrous dichloromethane drop wisely. The reaction was allowed to react at  $0^\circ\text{C}$  for 10 min before removal of solvent using a rotary evaporator under a reduce pressure. The desired compound was purified by a silica gel column using hexanes/ethyl acetate to produce a white power (yield. 62 %). The compound was fully characterized by  $^1\text{H}$  NMR (600 MHz,  $\text{CDCl}_3$ )  $\delta$  6.64 (s, 1H), 6.27 (d,  $J = 17.0$  Hz, 1H), 6.21 – 6.02 (m, 1H), 5.74 – 5.57 (m, 1H), 5.36 (dd,  $J = 10.9, 8.3$  Hz, 1H), 5.27 (t,  $J = 5.5$  Hz, 1H), 4.59 – 4.33 (m, 1H), 3.54 – 3.42 (m, 2H), 3.39 – 3.25 (m, 2H), 2.41 – 2.19 (m, 2H), 2.07 – 1.94 (m, 2H), 1.90 – 1.80 (m, 3H), 1.59 – 0.99 (m, 23H), 0.91 (d,  $J = 6.5$  Hz, 3H), 0.89 – 0.84 (m, 6H), 0.67 (s, 3H).

iii. *Synthesis of 16-amino-11-((carboxymethyl)carbamoyl)-1-((10,13-dimethyl-17-(6-methylheptan-2-yl)-2,3,4,7,8,9,10,11,12,13,14,15,16,17-tetradecahydro-1H-*

*cyclopenta[a]phenanthren-3-yl)oxy)-1,6,13-trioxo-9-thia-2,5,12-triazaheptadecan-17-oic acid (Scheme 3, compound CNLG)*

GSH (0.829 g, 2.7 mmol), sodium carbonate (0.434 g, 4 mmol), and compound C2 (0.45 g, 0.85 mmol) were dissolved in a mixed solution of tetrahydrofuran (28 mL) and water (24 mL). The mixture was allowed to stir at room temperature for 24 h before being mixed with excessive of aqueous formic acid (1%, v/v) to precipitate crude CNLG. The crude CNLG was further purified by washing three times with aqueous formic acid (1%, v/v) followed by washing with ethyl acetate three times. The precipitation was dried by lyophilization to yield white power in 43% yield. The melting point was determined by a MEL-TEMP® melting apparatus. CNLG was characterized by IR, MS, and HRMS.

### **2.3.6 Purity determination**

Stock solutions of CNLG (1 mg/mL) were prepared by dissolving CNLG in a solution of methanol and ammonium water (1:1 v/v, pH 10.2). The purity of CNLG(1 mg/mL) was checked by HPLC with a comparison to blank solvent (methanol and ammonium water (1:1 v/v, pH 10.2).

The same method was used to determine the purity of CLG and COLG.

### **2.3.7 *In vitro* cell cytotoxicity**

The cytotoxicity of CNLG against CV-1 cells and NCI-H226 cells was determine using the MTT [3-(4,5-dimethylthiazol-2-yl)-2,5-diphenyl tetrazolium bromide] assay. Briefly, cells were seeded in a 96-well plate with 3000 cells per well and incubated in the RPMI 1640 growth medium at 37 °C for 24 h. After 24 h, the growth medium was replaced with the fresh medium solution with various concentrations of

CNLG and continued to incubate for another 24 h. Subsequently, the cell viability was determined with the MTT assay. The absorbance (Abs) of each well was measured at 490 nm by a microplate reader. Cell viability was calculated by Eqs. (1):

$$Cell\ viability\ (\%) = \frac{Abs_{sample} - Abs_{blank}}{Abs_{control} - Abs_{blank}} \times 100 \quad (1)$$

### 2.3.8 CMC determination

The CMC of CNLG was measured by using pyrene as a fluorescent probe and following the procedure described in the literature [195]. Briefly, 1.5  $\mu$ L of 0.2 mM pyrene ethanol solution was placed in a vial containing 1mL each CNLG solution at different concentrations (0.00001 mg/mL to 1 mg/mL). After mixing, the fluorescence spectrum was recorded on a fluorescence spectrometer with the excitation wavelength of 334 nm, and the fluorescence intensities of the peaks at  $\sim$ 375 nm ( $I_1$ ) and  $\sim$ 384 ( $I_3$ ) were extracted from the spectra. A plot of  $I_3/I_1$  against the logarithm of CNLG concentration was made and the intersection of the two straight lines of the plot is the CMC value.

The same method was used to determine the CMC values of CLG and COLG.

### 2.3.9 Preparation of DiR loaded micelles

DiR loaded micelles were prepared by a film-dispersion method. Briefly, 7 mg of CNLG and 0.25 mg of DiR (5  $\mu$ L, 5 mg/mL in ethanol) were dissolved in 50  $\mu$ L ethanol and vortex mixed. The ethanol was completely evaporated under a gentle stream of nitrogen. The residue was hydrated with 1mL DPBS (no calcium, no magnesium, 1x) to a concentration of 7 mg/mL of CNLG followed by a sonication for 30 min with 5 min break at 40  $^{\circ}$ C. The solution was centrifuged at 14000 rpm for 10 min to remove insoluble DiR to yield CNLG DiR micelles [196].

The same method was used to prepare CLG DiR micelles and COLG DiR micelles.

### 2.3.10 Preparation of Rhodamine B loaded CNLG micelles

Rhodamine B loaded CNLG micelles were prepared for the cell uptake study and *in vitro* release study. The preparation of Rhodamine B loaded CNLG micelles followed the same procedure as that for DiR loaded CNLG micelles except Rhodamine B was used in place of DiR.

### 2.3.11 Characterization of DiR loaded micelles

DiR loaded micelles were characterized for their particle size and zeta potential (surface charge). Briefly, a solution of freshly prepared DiR loaded micelles was diluted with deionized water (0.5:100) before measurement of particle size and zeta potential on a Malvern Zetasizer Nano particle size analyzer .

### 2.3.12 Determination of DiR encapsulation efficiency and loading capacity

The encapsulation efficiency (EE%) and loading capacity (LC%) of DiR were determined by extracting DiR from DiR loaded CNLG micelles with ethanol and the fluorescence intensity was measured on a fluorescent plate reader by using 730 nm and 780 nm as the excitation and emission wavelengths. A calibration curve was constructed by spiking a known concentration of DiR to blank micelles. The EE% and LC% were calculated by the following Eqs. (2) and Eqs. (3):

$$EE \% = \frac{\text{weight of DiR loaded in micelles}}{\text{weight of total DiR used for encapsulation}} \times 100 \quad (2)$$

$$LC \% = \frac{\text{weight of DiR loaded in micelles}}{\text{weight of micelles}} \times 100 \quad (3)$$

### **2.3.13 Storage stability of DiR loaded micelles**

The storage stability of DiR loaded micelles was checked at 4 °C for a week. Briefly, freshly prepared DiR loaded micelles were stored at 4 °C. An aliquot (5µL) was withdrawn on day 0, day 1, day 2, day 3, and day 7. The aliquot was diluted with deionized water (0.5:100) before checked for particle sizes as described above.

### **2.3.14 Rhodamine B *in vitro* release study**

The *in vitro* release study of Rhodamine B from Rhodamine B loaded CNLG micelles was conducted by dialysis with both PBS buffer (pH 7.4, 0.1 M) and citric buffer (pH 4.5, 0.1 M) as the release medium. Rhodamine B loaded CNLG micelles (4.7 µg Rhodamine B /mL, 0.5 mL) were dialyzed in a pre-swollen dialysis bag (molecule weight cut-off: 10 kDa) immersed in the 40 mL release medium at 37 °C with a stirring speed of 100 rpm. At predetermined time intervals (0, 0.25, 0.5, 1, 2, 4, 6, 10, 24 h), an aliquot (3 mL) was withdrawn for determination of the released Rhodamine B by HPLC with a UV/vis detector (550 nm). The same volume of the fresh releasing medium was added back to the dialysis to maintain the dialysis volume. A parallel analysis with the release of Rhodamine B from ethanol solution was conducted for comparison.

### **2.3.15 Cellular uptake of Rhodamine B**

For cellular uptake study, the isolated mouse kidney cells (2<sup>nd</sup> passage) were seeded in 96-well plate at a density of ~ 5000 cells/well. When the cells reach 90 % confluence, the culture medium was removed, and the cells were treated with the culture medium only or probenecid (1 mM) for 30 min followed by a replacement of the medium containing Rhodamine B loaded CNLG micelles (116 µg/ml) or Rhodamine B loaded CNLG micelles (116 µg/ml) plus probenecid (1 mM) for additional 30 min at 37 °C

before removal of the medium. The cells were washed three times with DPBS. The fluorescence intensity was measured on a microplate reader ( $\lambda_{\text{ex}}$  540 nm,  $\lambda_{\text{em}}$  625 nm). The data were expressed as a percentage of control (n = 3).

### **2.3.16 *In vivo* animal study**

*In vivo* animal study was carried with females BALB/Cj mice (6-8 weeks old, 17-20 g) with the procedure approved by the Institutional Animal Care and Use Committee (IACUC) at South Dakota State University, Brookings, SD, USA.

For pre-evaluation of brain-targeting ability among CLG, COLG and CNLG, the mice were divided into 4 groups with 1 mouse/group and injected intravenously through the tail vein with free DiR solution (25  $\mu\text{g}/\text{mL}$ ), DiR loaded CLG micelles, DiR loaded COLG micelles or DiR loaded CNLG micelles.

For further evaluation of brain-targeting ability of DiR loaded CNLG micelles, the mice were randomly divided into 2 groups with 3 mice in each group and intravenously administered with free DiR solution (25  $\mu\text{g}/\text{mL}$ ) or CNLG DiR micelles through a tail vein injection.

All the injected doses were adjusted based on the determined encapsulation efficiency (EE%) of DiR loaded micelles to make sure that each mouse received the same amount of DiR.

#### **2.3.16.1 Whole-body fluorescence images of mice**

The mice were anesthetized with a gas mixture of oxygen and isoflurane at predetermined time intervals (15 min, 30 min, 1h, 2 h, 4 h, 6 h, 12 h, and 24 h) after administered with DiR loaded CNLG micelles or free DiR. The fluorescence images of

whole-body were obtained on a Bruker Xtream *in-vivo* imager ( $\lambda_{\text{ex}}$  730 nm,  $\lambda_{\text{em}}$  790 nm), and the fluorescence intensity was quantified using the Bruker MI SE software.

#### **2.3.16.2 *Ex-vivo* brain and organs imaging of mice**

The mice were sacrificed at 2 h post tail vein injection of DiR loaded micelles or free DiR, and the heart was perfused with DPBS to remove blood in tissues before organs were harvested. The fluorescence images of brain and other organs were obtained on a Bruker Xtream *in-vivo* imager ( $\lambda_{\text{ex}}$  730 nm,  $\lambda_{\text{em}}$  790 nm) and the fluorescence intensity was quantified using the Bruker MI SE software as well.

#### **2.3.17 Statistics**

Data were reported as mean  $\pm$  standard deviation (SD). Student's *t*-test was used for two group comparison and one-way ANOVA was used for multiple group comparison by analyzed with GraphPad Prism 8, Excel, or R software. *P*-value of less than 0.05, 0.01 or 0.001 was considered as statistically significant.

## CHAPTER 3 DESIGN, SYNTHESIS, AND EVALUATION OF OG AND OLG AS BRAIN TARGETING AGENTS

### 3.1 Introduction

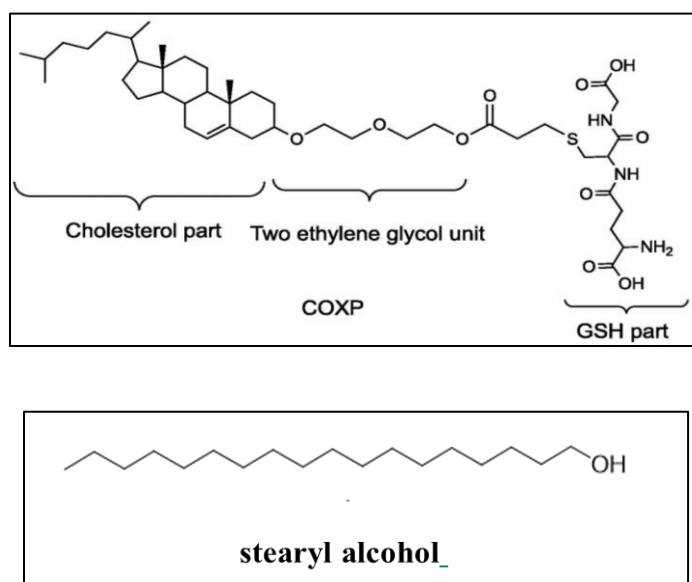
In the last chapter, we designed three COXP derivatives, namely CLG, COLG and CNLG, by modifying the linker structure between cholesterol and GSH of COXP. The results demonstrated that all three can undergo self-assembly to form micelles and the micelles are capable to deliver DiR to the brain with CNLG micelles being the most effective brain targeting micelles of all three.

In this chapter, we decided to replace the cholesterol structure with a hydrophobic fatty alcohol. We expected the replacement of the hydrophobic structure cholesterol with a hydrophobic structure fatty alcohol would maintain the amphiphilic nature of the molecule. Therefore, the resulting designed molecules would still be expected to self-assemble to form a micelle and the hydrophilic structure GSH would still be expected to cover the surface of the micelle to produce the brain-targeting effect.

After careful consideration, stearyl alcohol was selected as the fatty alcohol to replace cholesterol (Figure 34). Stearyl alcohol, also known as 1-octadecanol, is an endogenous long-chain saturated fatty alcohol with an 18-carbon chain and is located in many organs in our body, such as brain, skin, kidney, and intestine. It plays a biological role as a membrane stabilizer, energy source, energy storage and nutrient and involves in lipid transport and metabolism process. Therefore, stearyl alcohol is biocompatible and with low toxicity [197, 198]. Stearyl alcohol has been widely used as a surfactant and emulsifier in industry and has already been applied for topical drug delivery to increase skin permeation by incorporation into lipid nanoparticles [199, 200]. It is worth noting

that stearyl alcohol is prepared from stearic acid (SA), which has been conjugated onto chitosan (CS) to achieve stearic acid modified chitosan (CS-SA) brain targeting micelle drug delivery system and the result demonstrated that CS-SA micelles could effectively deliver doxorubicin across the BBB and enter into the brain[201]. In addition, with stearyl alcohol in the structure, the designed compound is expected to insert the stearyl alcohol part into liposome's lipid layer when used for the preparation of liposomes, just like cholesterol in liposomes, and orient its GSH on the surface of liposomes for brain targeting.

In this chapter, two brain targeting agents (OG and OLG) were designed by connecting stearyl alcohol to GSH through two different linkers (Figure 34).



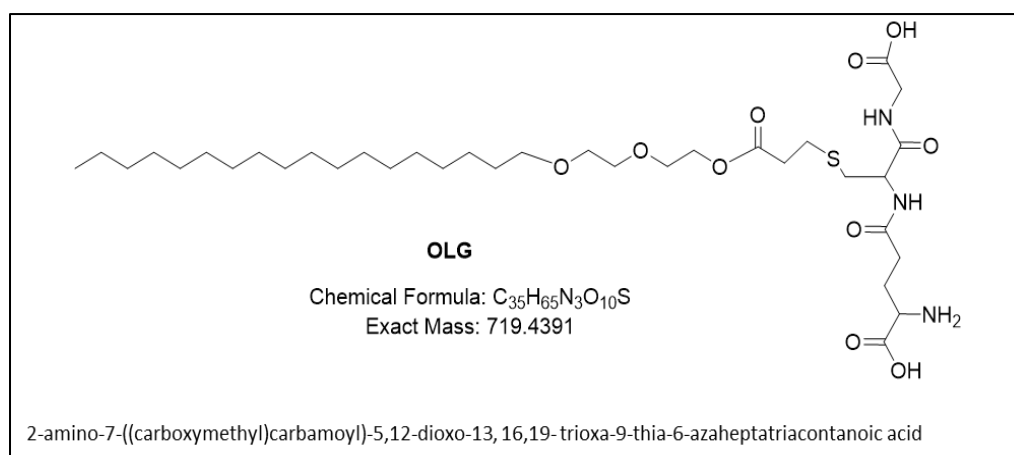
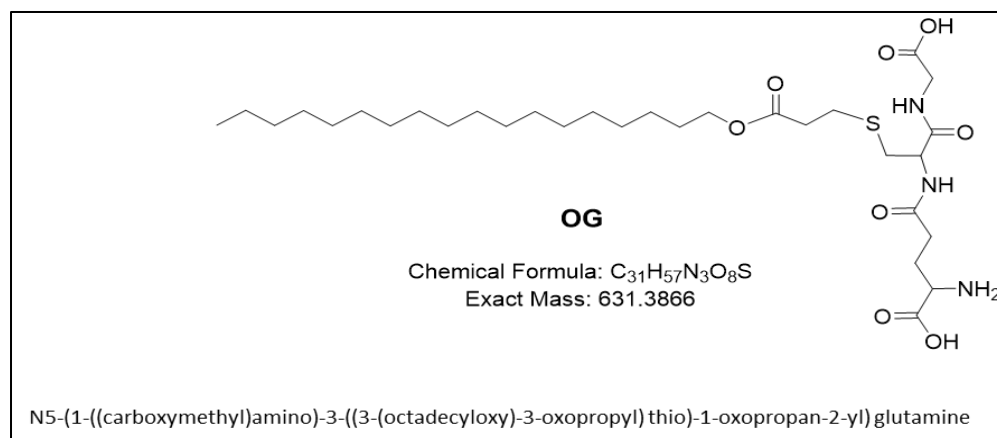


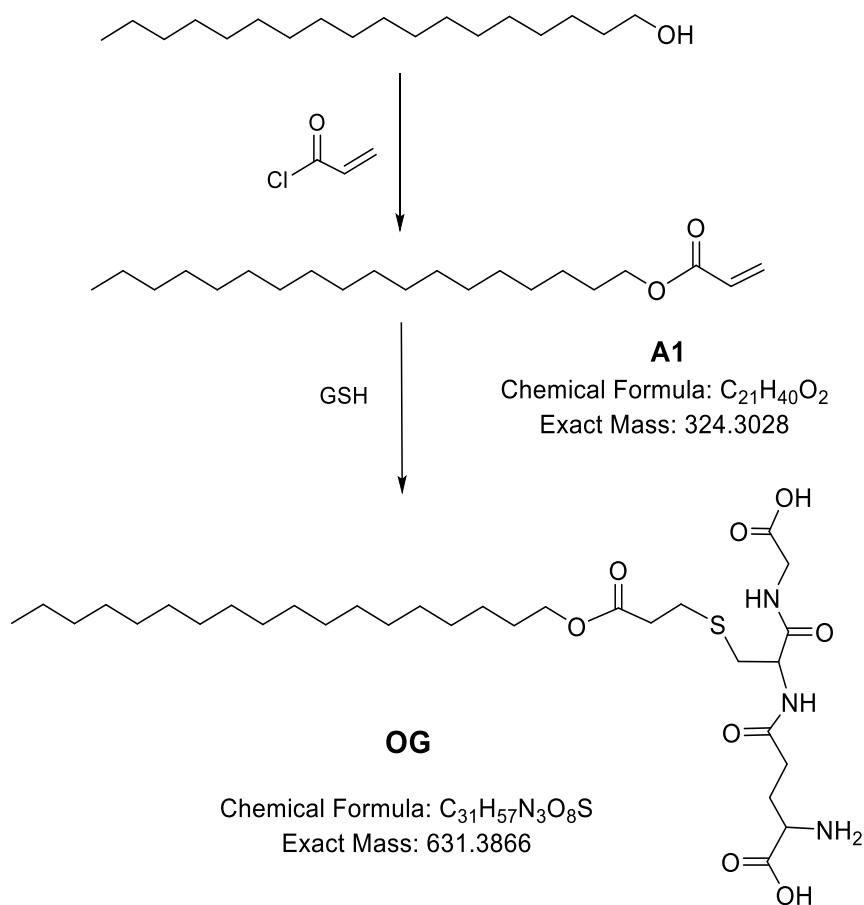
Figure 34. Chemical structure of COXP, Stearyl alcohol, OG and OLG .

## 3.2 Result and Discussion

### 3.2.1 Synthesis and characterization of OG

OG was synthesized in 2 steps as outlined in Scheme 4. The synthesis started with esterification of 1-octadecanol with acryloyl chloride in the presence of triethylamine to yield compound A1 in 44.1% yield. Compound A1 was then coupled with GSH via a Michael addition reaction in the presence of sodium carbonate to produce

the final compound (OG) in 21% yield with the melting point of 200 °C. The purity of OG was determined to be >95% by HPLC.



Scheme 4 Synthesis of OG

The characterization of OG was achieved by <sup>1</sup>H NMR, IR and HRMS. Figure 35 showed the HRMS spectrum of OG. The molecular weights of the calculated protonated form (M+H)<sup>+</sup> and sodium adduct (M+Na)<sup>+</sup> form of OG were 632.3939 and 654.3758, respectively. The observed molecular weights were 632.3941 and 654.3759 respectively

consistent with the expected structure. The sodium adduct peak was observed to be the most abundant peak.

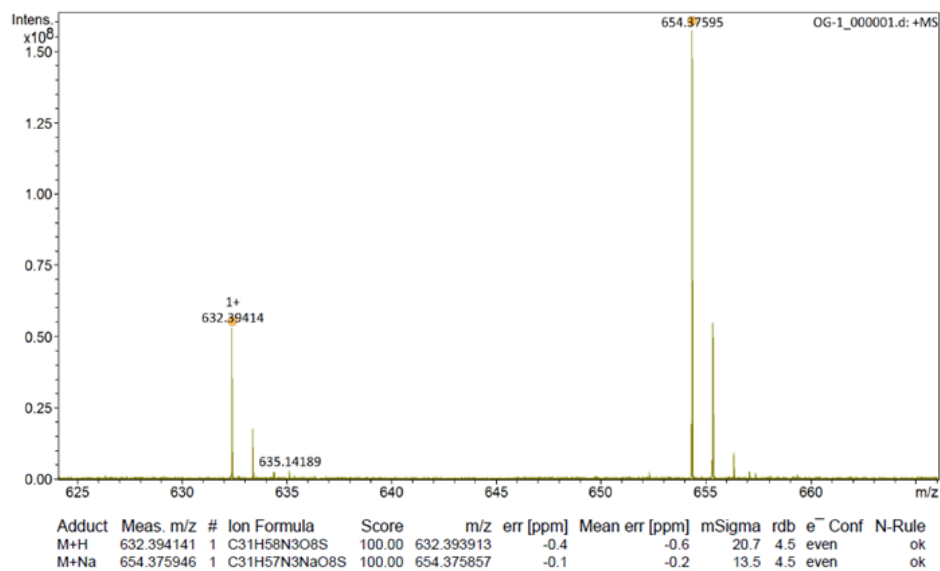


Figure 35. HRMS spectrum of OG

Similar to CLG, COLG, and CNLG, OG was confirmed to be the *S*-isomer by LC/MS/MS not *N*-isomer based on the fact that two fragments ( $m/z$  fragment at 558.54 and  $m/z$  fragment at 504.52) generated from the neutral losses of glycine and pyroglutamate respectively were observed (Figure 36) consistent with the structure of the *S*-isomer. Further, the  $m/z$  fragment at 400.95 generated from  $C_{22}H_{47}NO_2S$  provides an additional piece of evidence for the structure of the *S*-isomer.

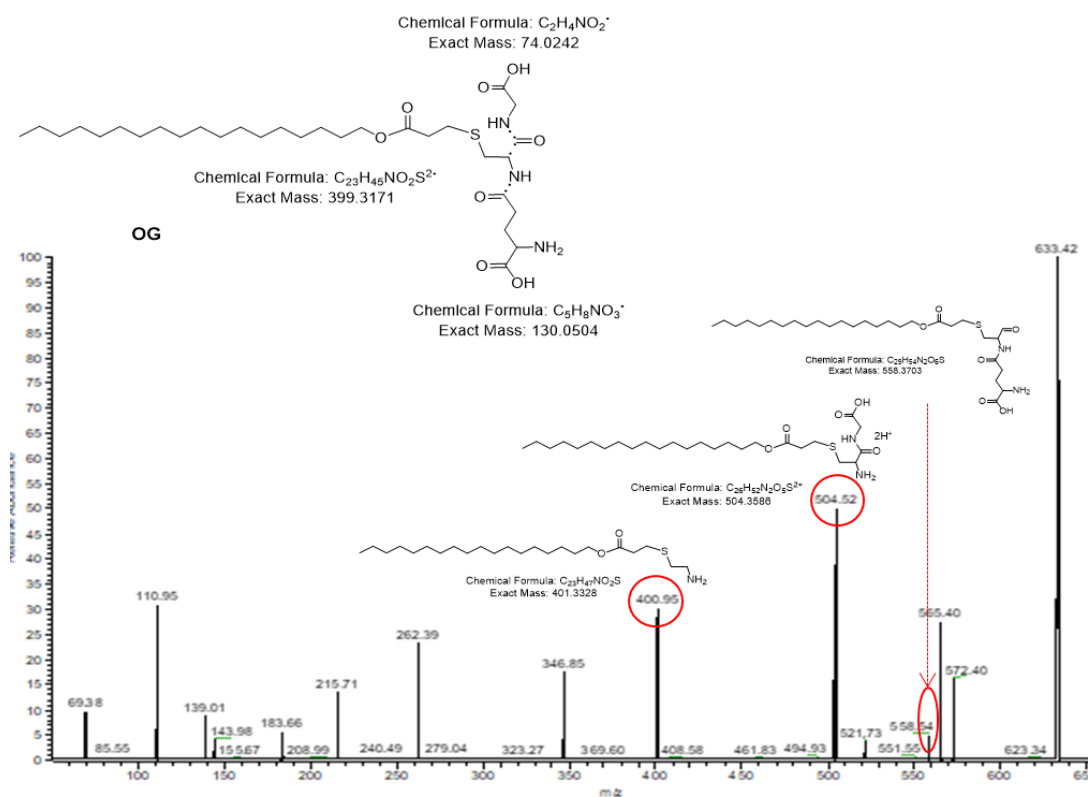
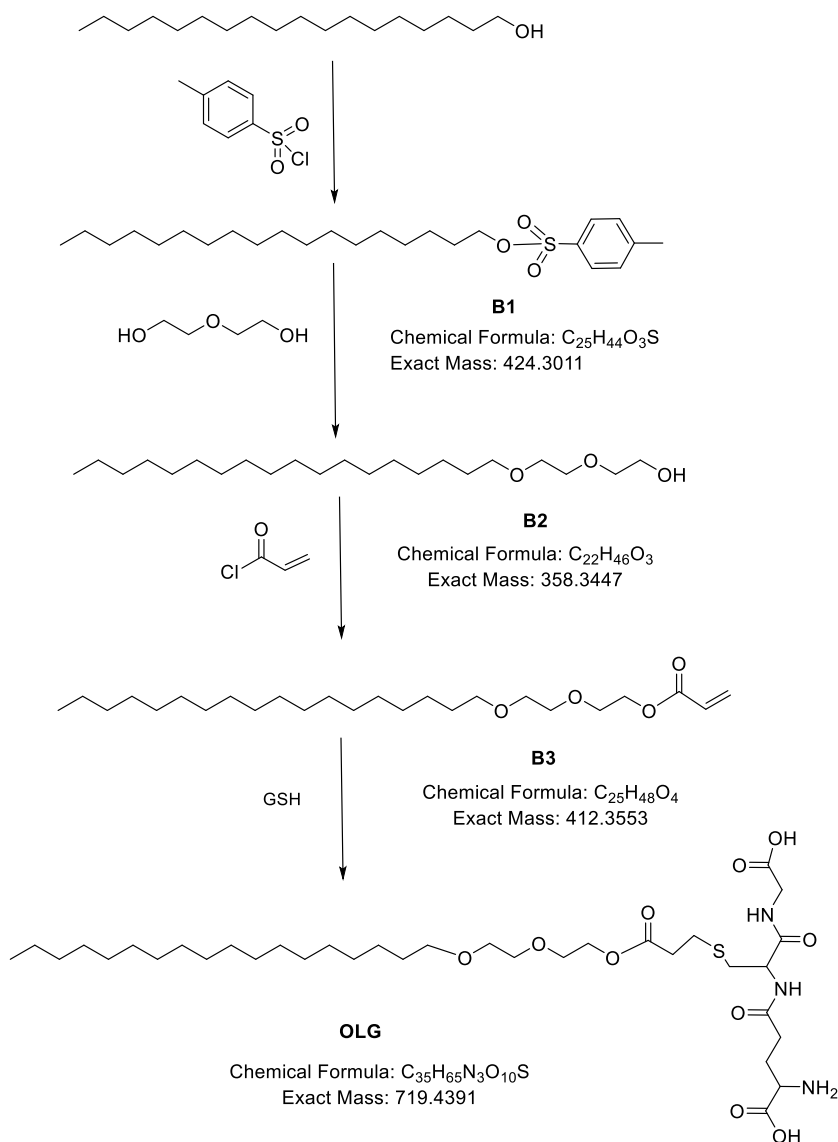


Figure 36. LC/MS/MS spectrum of OG.

### 3.2.2 Synthesis and characterization of OLG

OLG was synthesized in 4 steps as outlined in Scheme 5. The synthesis started with tosylation of 1-octadecanol with 4-toluenesulfonyl chloride in the presence of pyridine and triethylamine in anhydrous dichloromethane to yield tosylated 1-octadecanol (B1) in 35% yield. Diethylene glycol reacted with tosylated 1-octadecanol (B1) in dioxane under reflux condition to produce 2-(2-(octadecyloxy)ethoxy)ethan-1-ol (B2) in 63% yield. Then compound B2 was coupled with acryloyl chloride through esterification in the presence of triethylamine to produce 2-(2(octadecyloxy)ethoxy)ethyl acrylate (B3) in 43% yield, the final compound OLG was obtained through a Michael addition reaction by coupling GSH with compound B3 in the presence of sodium

carbonate in 60% yield with a melting point of 196 °C. The purity of OLG was determined to be >95% by HPLC.



Scheme 5 Synthesis of OLG

Characterization of OLG was achieved by <sup>1</sup>H NMR, IR and HRMS. The calculated HRMS for the protonated OLG [C<sub>35</sub>H<sub>66</sub>N<sub>3</sub>O<sub>10</sub>S (M+H)<sup>+</sup>] is 720.4463 and found at 720.4465 (Figure 37) consistent with the expected structure.

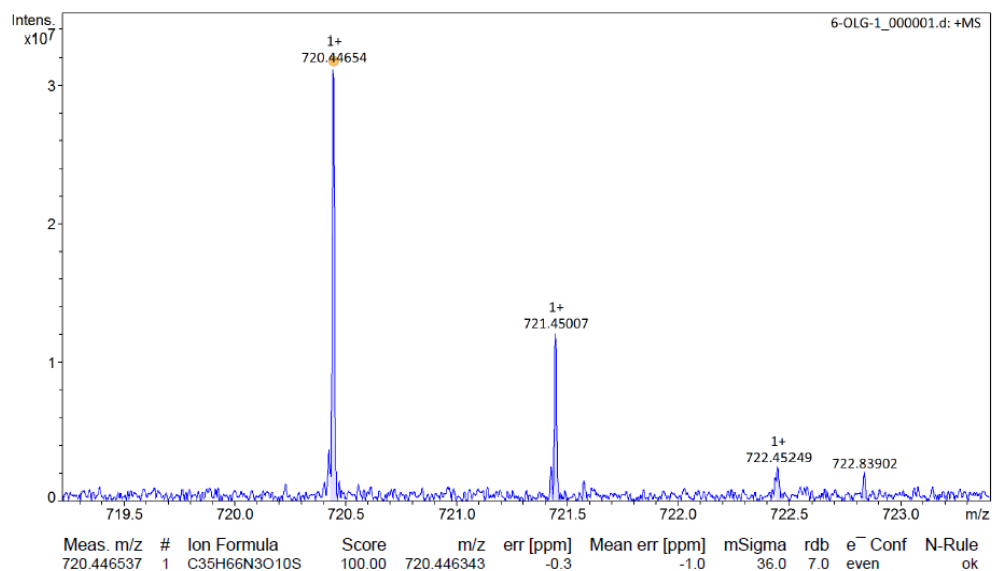


Figure 37. HRMS spectrum of OLG

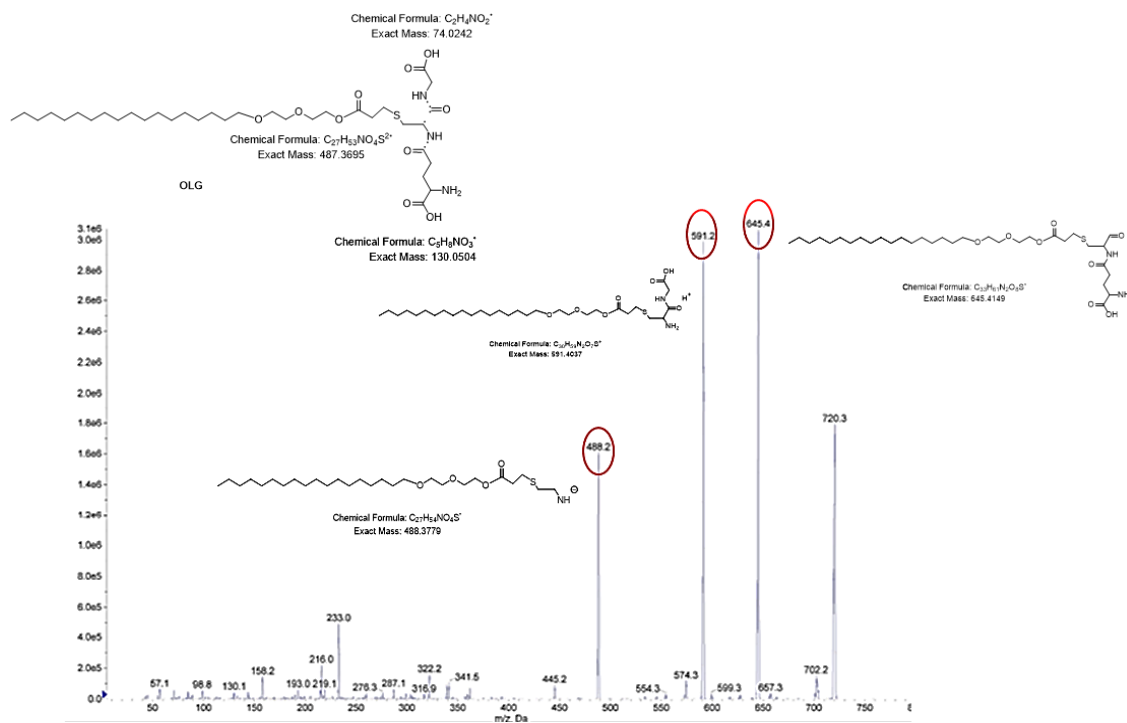


Figure 38. LC/MS/MS spectrum of OLG

Again, two neutral losses of OLG were observed in the LC/MS/MS spectrum of OLG (Figure 38),  $m/z$  fragment at 645.4 due to the neutral loss of glycine and  $m/z$  fragment at 591.2 due to the neutral loss of pyroglutamate, confirming that the structure is the *S*-isomer. In addition, the  $m/z$  fragment at 488.2 generated from  $C_{27}H_{54}NO_4S^-$  matches well with the structure of the *S*-isomer not *N*-isomer.

### 3.2.3 CMC determination

To determinate CMC of OG and OLG, the fluorescence intensity of pyrene ( $I_3/I_1$ ) against logarithm of the concentration of OG or OLG was plotted as described in section 2.3.8.

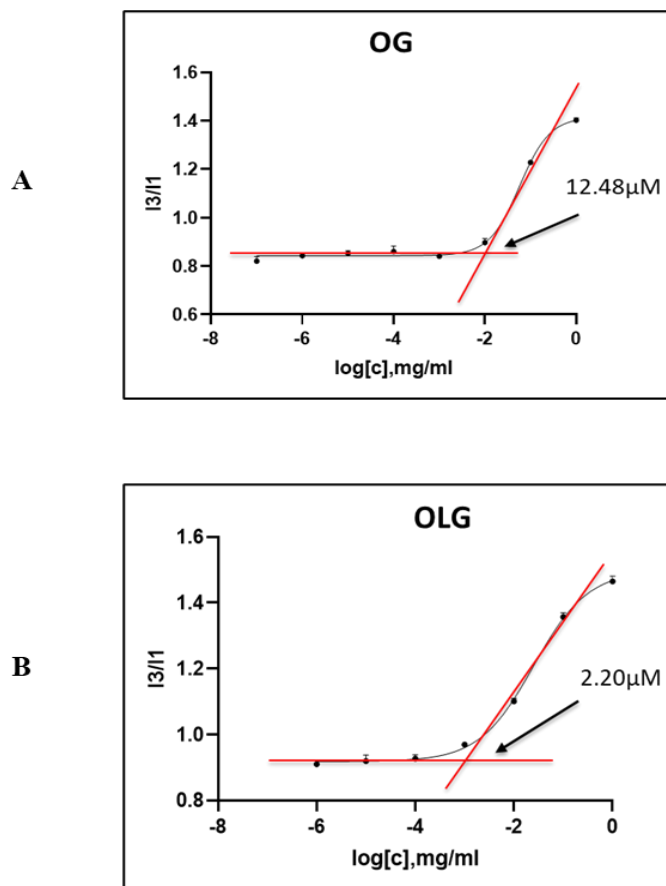


Figure 39. Determination of CMC of (A)OG micelles; (B) COLG micelles. Data are presented as the mean  $\pm$  SD (n=3).

As shown in Figure 39 when the concentration of OG or OLG was low, the fluorescence intensity of pyrene was low. When the concentration reached the CMC of OG or OLG, the fluorescence intensity of pyrene increased abruptly due to the fact that pyrene started to be encapsulated into the inner hydrophobic core of the micelles. The CMC of OG and OLG were determined to be 12.48  $\mu$ M and 2.20  $\mu$ M, respectively. Again, the low  $\mu$ M CMC suggests that OG or OLG micelles are stable enough when administrated into the blood circulation.

### 3.2.4 *In vitro* cytotoxicity

The *in vitro* cytotoxicity was tested with CV-1 cell line and NCI-H226 cell line through the MTT assay. Based on the dose-response curves (Figure 40), the  $IC_{50}$  values of OG for the CV-1 cell line and the NCI-H226 cell line were 124  $\mu$ M and 187  $\mu$ M, respectively. The  $IC_{50}$  values obtained from the dose-response curves of OLG (Figure 41) were 97.14  $\mu$ M and 100  $\mu$ M for the CV-1 cell line and the NCI-H226 cell line, respectively.

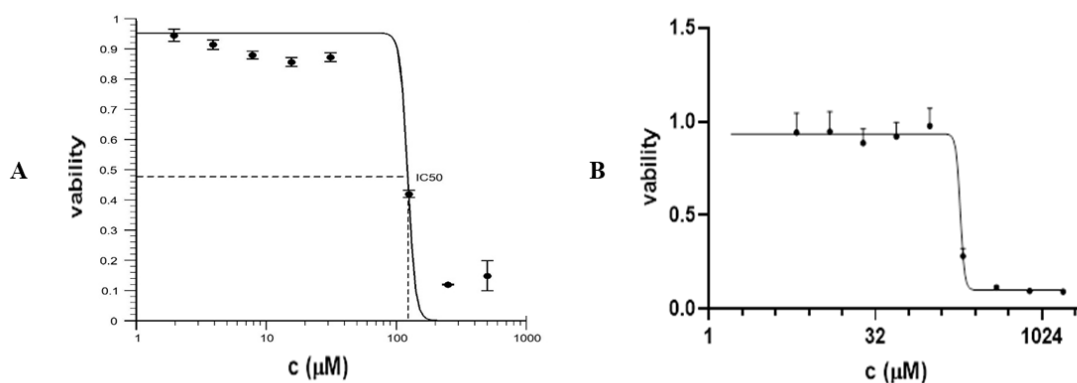


Figure 40. Dose-response curves for the determination of  $IC_{50}$  values of OG with (A) CV-1 cell line (B) NCI-H226 cell line. Data are presented as the mean  $\pm$  SD (n=3).

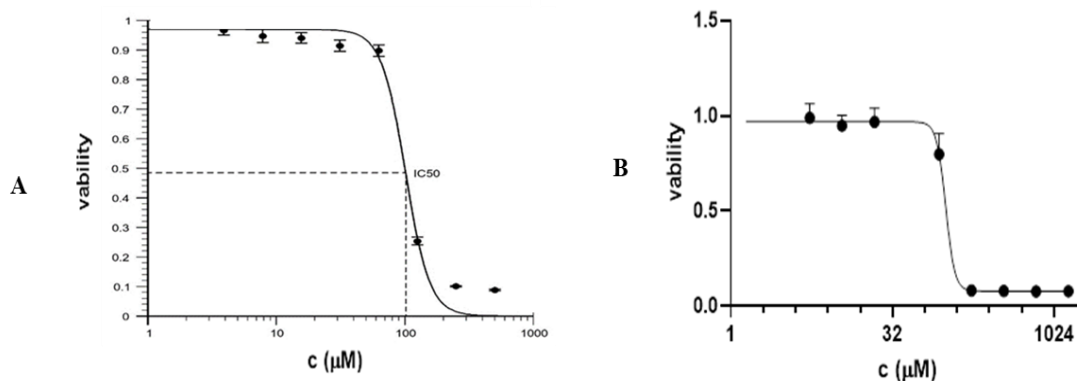
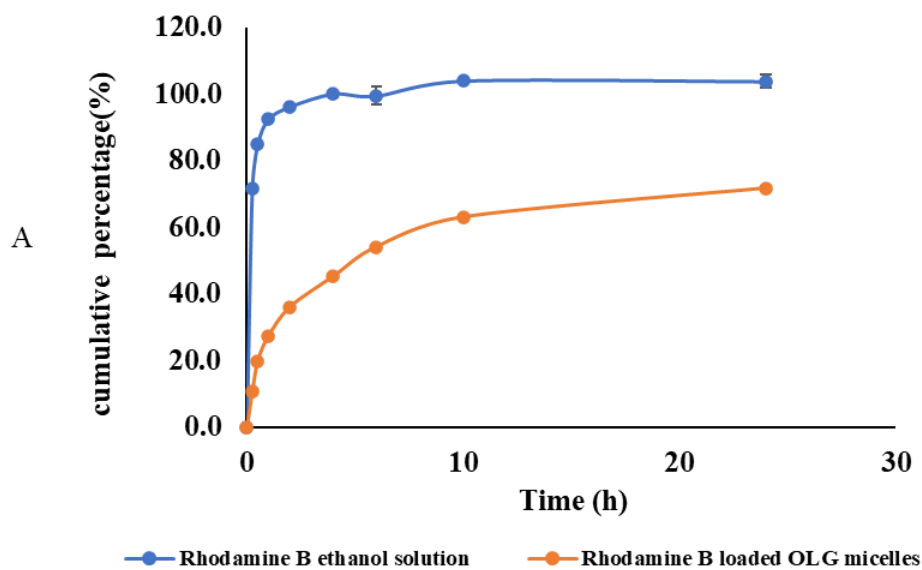


Figure 41. Dose-response curves for the determination of  $\text{IC}_{50}$  values of OLG with (A) CV-1 cell line (B) NCI-H226 cell line. Data are presented as the mean  $\pm$  SD (n=3).

The *in vitro* toxicity study indicated that OG and OLG could be used as a relatively safe carrier for the brain-targeting drug delivery.

### 3.2.5 Rhodamine B *in vitro* release study

The release study was conducted with Rhodamine B loaded OG micelles or OLG micelles through a dialysis method with PBS (pH 7.4) as the release medium.



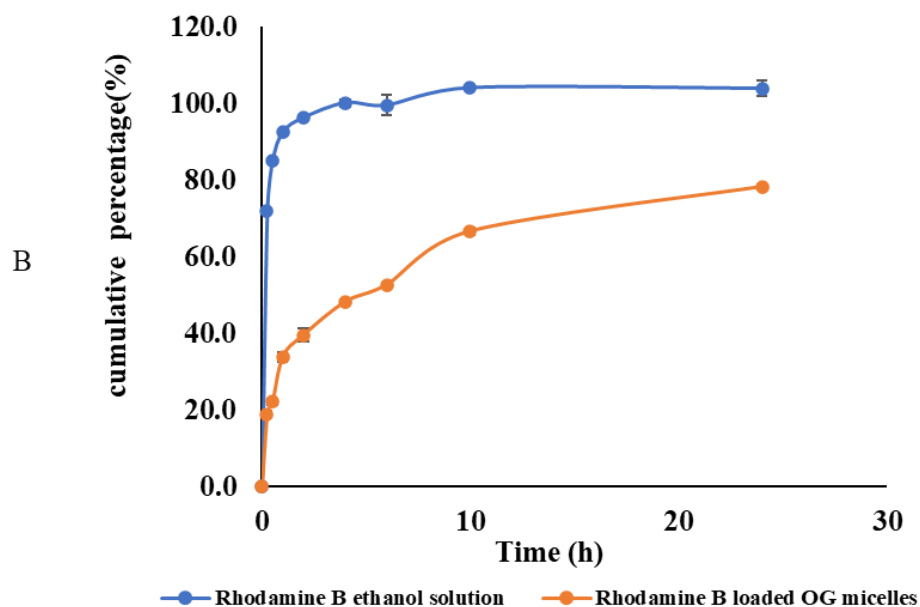


Figure 42. Release of Rhodamine B from (A) Rhodamine B loaded OG micelles and (B) Rhodamine B loaded OLG micelles with a comparison to the Rhodamine B ethanol solution in a pH 7.4 PBS buffer. *Data are presented as mean  $\pm$  SD (n=3).*

As shown in Figure 42, Rhodamine B loaded OG micelles or OLG micelles has the similar releasing behavior with ~50% of Rhodamine B released from the micelles within 4 hours. The release was consistently until the cumulative Rhodamine B released reached approximately 80% in 24 hours. Compared with the observation that the majority of Rhodamine B was released from the ethanol solution within 4h, OG micelles and OLG micelles exhibited a relatively slow and sustained release.

### 3.2.6 Cellular uptake of Rhodamine B

For cellular uptake study, the isolated mouse kidney cells were employed to check the cell uptake of Rhodamine B loaded OG or OLG micelles as well as the uptake in the presence of probenecid – a GSH transporter inhibitor.

As demonstrated in Figure 43, Rhodamine B loaded OG or OLG micelles were taken by the kidney cells readily. In the presence of 1mM probenecid, ~50% cell uptake of OG micelles and ~60% cell uptake of OLG micelles were inhibited, suggesting OG or OLG micelles entered the cells through a GSH transporter. The results were consistent with earlier studies for COXP and CNLG [202].

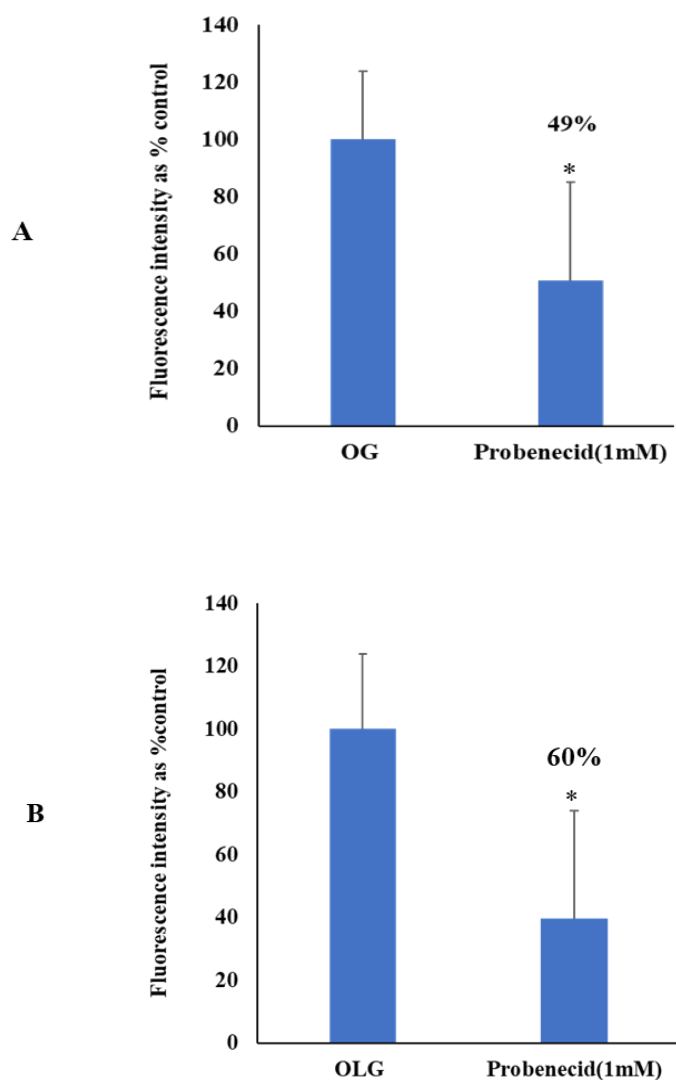


Figure 43. Cell uptake inhibition of (A) OG micelles and (B) OLG micelles by probenecid. Data are presented as mean  $\pm$  SD ( $n=3$ ).  $P < 0.05$  \*

### 3.2.7 Preparation and characterization of DiR loaded micelles

DiR loaded OG micelles or OLG micelles were prepared for brain targeting studies. DiR loaded OG micelles or OLG micelles were prepared by a film-dispersion method as described earlier in section 2.2.3.1.

As shown in Table 7-I the particle size of DiR loaded OG micelles was determined to be  $220.03 \pm 15.90$  nm (n=3), which is slightly larger than the preferred brain targeting size (<150 nm). In contrast, the particle size of DiR loaded OLG micelles was much smaller ( $18.04 \pm 2.16$  nm, n=3). The PDI values of DiR loaded OG micelles and OLG micelles were found to be  $0.31 \pm 0.01$  nm and  $0.57 \pm 0.06$  nm, respectively reflecting a narrow size distribution of the micelles. DiR loaded OG micelles or OLG micelles were found to carry a negative surface charge with zeta potential of  $-51.5 \pm 0.82$  and  $-31.7 \pm 6.05$ , respectively, confirming that the negatively charged GSH molecule is oriented outside of the micelles.

The EE% of DiR loaded OG micelles and DiR loaded OLG micelles were determined to be  $99.59 \pm 0.37\%$  and  $79.83 \pm 0.73\%$  with the LC% to be  $0.35 \pm 0.0013\%$  and  $0.28 \pm 0.0026\%$ , respectively (Table 7-II), indicating DiR was successfully encapsulated into the hydrophobic core of OG or OLG micelles. It is worth noting that the EE % of DiR loaded OLG micelles is relatively lower (<90%). This may be caused by the smaller size of OLG micelles.

Table 7 Characterization of DiR loaded micelles

<b>I</b>	<b>Preparation</b>	<b>Size (nm)</b>	<b>PDI</b>	<b>Zeta potential (mV)</b>
	<b>DiR loaded OG micelle</b>		220.03±15.90	0.31±0.01
<b>DiR loaded OLG micelle</b>		18.04±2.16	0.57±0.06	-31.7±6.05

<b>II</b>	<b>Preparation</b>	<b>Theoretical loading (%)</b>	<b>EE (%)</b>	<b>LC (%)</b>
	<b>DiR loaded OG micelle</b>		0.35	99.59±0.37
<b>DiR loaded OLG micelle</b>		0.35	79.83±0.73	0.28±0.0026

*Data are presented as mean ± SD (n=3).*

### 3.2.8 Storage stability of DiR loaded micelles

The storage stability of DiR loaded OG or OLG micelles was checked by monitoring the changes in micellar particle size at 4 °C. The data are shown in Figure 44

For DiR loaded OG micelles, the particle size on time 0 was 220.03 ± 15.91 nm vs 216.83 ± 46.37 nm on time 24 h. No significant difference in particle size (P = 0.915, student's t test) was observe between day 0 and day 1, indicating DiR loaded OG micelles was stable for at least 24h.

For DiR loaded OLG micelles, the particle size on time 0 was  $18.04 \pm 2.16$  nm vs  $20.48 \pm 1.69$  nm on time 48 h, no significant difference in particle size ( $P = 0.115$ , one-way anova) was observed between days, suggesting DiR loaded OLG micelles was stable for 48 h.

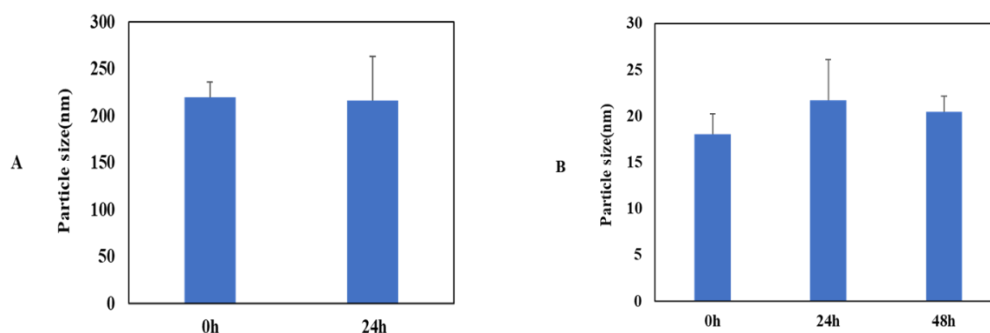


Figure 44. Stability of (A) DiR loaded OG micelles; (B) DiR loaded OLG storage at 4°C.

Data are presented as mean  $\pm$  SD ( $n=3$ ).

### 3.2.9 Whole-body fluorescence images of mice

Brain-targeting of DiR loaded OG or OLG micelles was investigated through whole-body imaging of mice. The mice were intravenously injected with free DiR, DiR loaded OG, or OLG micelles through tail vein before subjected to whole body imaging under a Bruker Xstream *in-vivo* imaging system. Images were taken at different time points after injection.

Figure 45 shows the whole-body fluorescence imaging and corresponding brain fluorescence intensity of the mice at 15 min, 30min, 1h, 2 h, 5 h, 12 h, and 24 h after injected with free DiR and DiR loaded OG micelles. As shown in the figure, the majority of DiR was observed in the liver for free DiR though a minimal brain distribution was observed. Compared with DiR delivered by free DiR, a much faster and significantly

more brain distribution of DiR were observed for DiR delivered by OG micelles with an increase of ~42-fold (B: A; Figure 45-II) observed at 15 min. The brain distribution of DiR reached the highest at 2h (63-fold increase, Figure 45-II), followed by a gradual drop after 2h. A 29-fold increase at 24 h was observed (B: A; Figure 45-II).

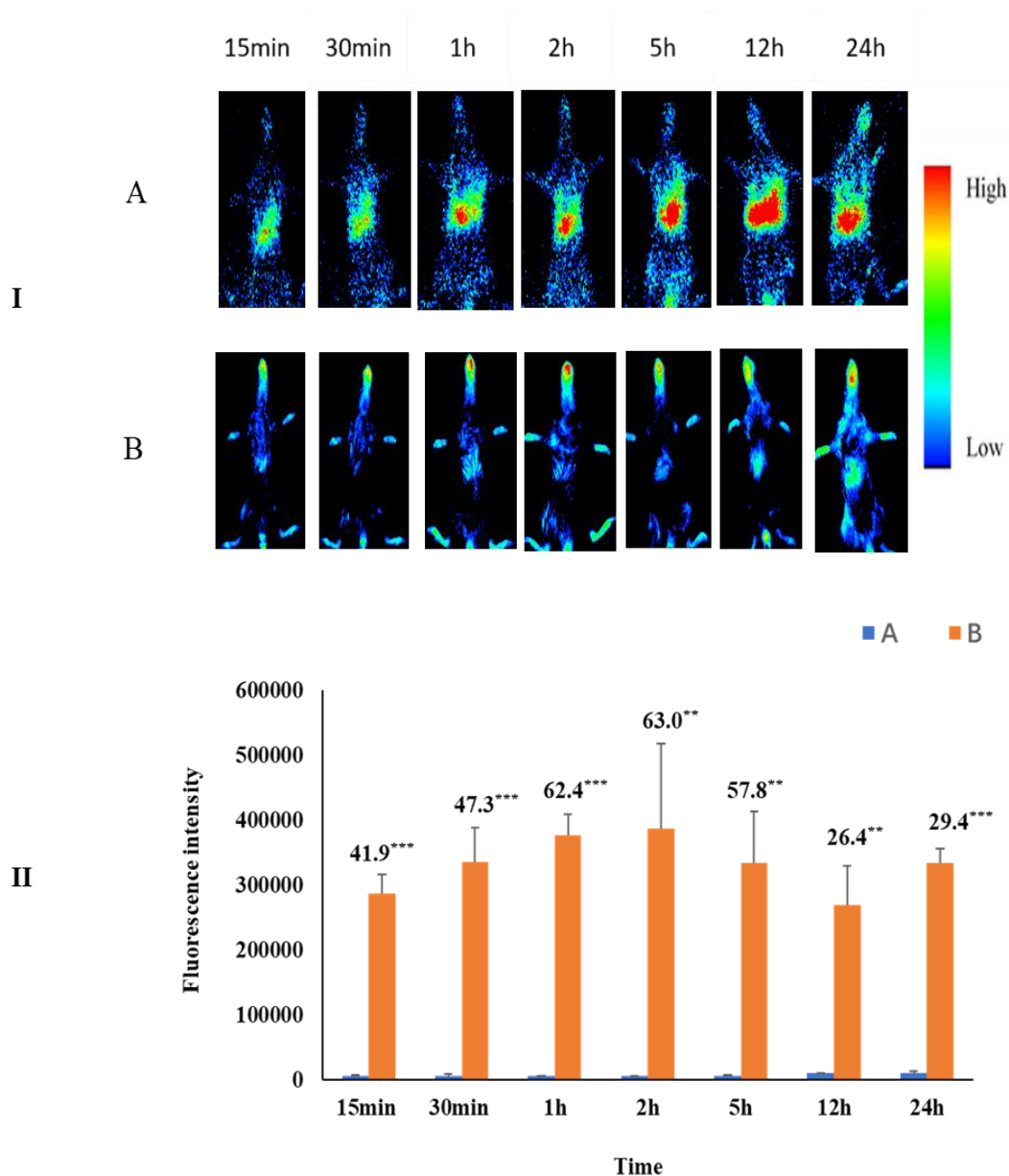
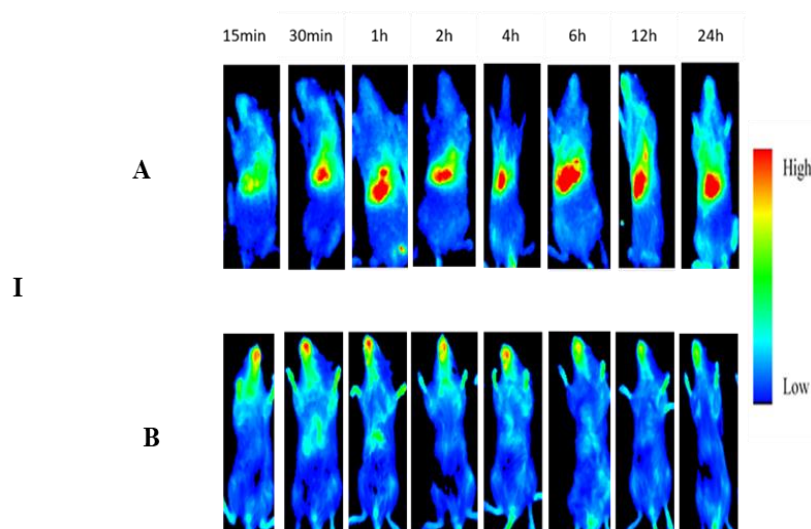


Figure 45. Representative whole-body fluorescence imaging (**I**) and corresponding fluorescence intensities (**II**) of the brains 2h after i.v injection of free DiR (**A**) or DiR

loaded OG micelles (**B**). Results are presented as mean  $\pm$  SD ( $n=3$ ).  $P < 0.01$  \*\*  $P < 0.001$  \*\*\*

The whole-body imaging results from the treatment of OLG micelles are presented in Figure 46. As shown in Figure 46-I, a similar distribution profile of DiR delivered by free DiR was observed with a minimum brain distribution and the majority DiR distributed in the liver during the 24-h treatment. In contrast, the majority DiR was found in the brain for DiR delivered by OLG micelles with the highest at 30 min for a 98-fold increase, then dropped afterwards. It still remained a 24-fold increase at 24 h (Figure 46-II).



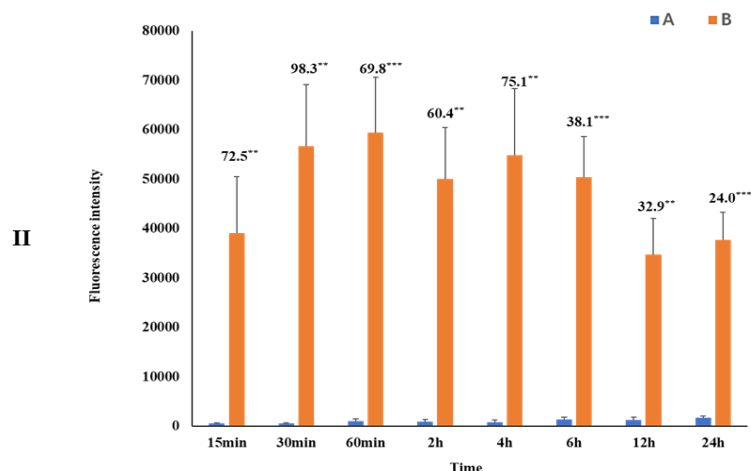


Figure 46. Representative whole-body fluorescence imaging (I) and corresponding fluorescence intensities (II) of the mouse brains after i.v injection of free DiR (A), DiR loaded OLG micelles (B). Results are presented as mean  $\pm$  SD ( $n=3$ ).  $P < 0.01$  \*\*  $P < 0.001$  \*\*\*

### 3.2.10 *Ex-vivo* fluorescence imaging

To further confirm the brain targeting effect and check the tissue biodistribution of DiR loaded OG and OLG micelles, the *ex-vivo* imaging of the brain and other major organs (heart, lung, liver, spleen, and kidney) of mice treated with DiR loaded OG or OLG micelles after 2h was performed.

#### 3.2.10.1 *Ex-vivo* imaging of brain

The *ex-vivo* imaging of brain of mice treated with OG micelles at 2 h (Figure 47-I) showed that a higher fluorescence than that of mice treated with free DiR. Based on the fluorescence intensity (Figure 47-II), OG micelles were able to increase the delivery of DiR to the brain by 6.4-fold ( $P=0.039$ , Student's t test) at 2 h compared with free DiR.

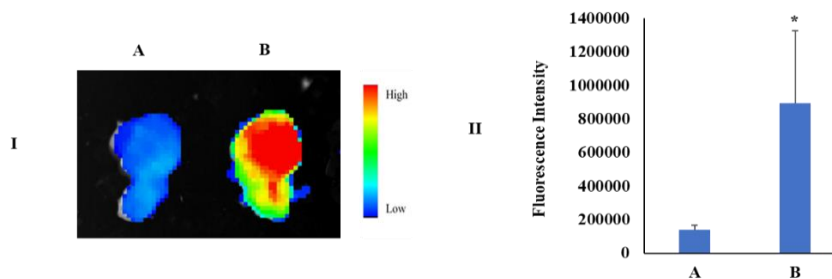


Figure 47. Representative *ex-vivo* images (I) and corresponding fluorescence intensities (II) of the mouse brains 2 h after a single dose tail vein injection of (A) free DiR and (B) DiR loaded OG micelles. Results are presented as mean  $\pm$  SD ( $n=3$ ).  $P < 0.05$  \*

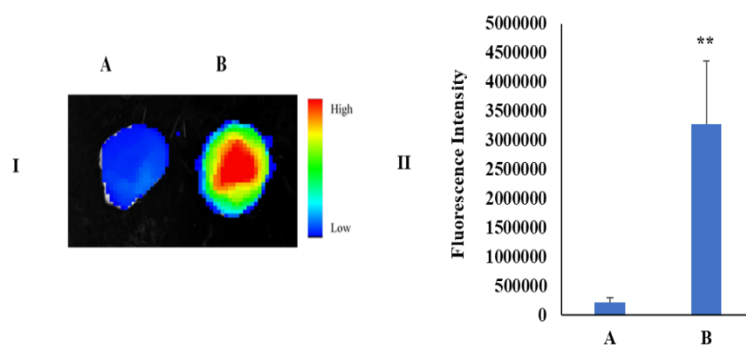


Figure 48. Representative *ex-vivo* images (I) and corresponding fluorescence intensities (II) of the mouse brains 2 h after a single dose tail vein injection of (A) free DiR and (B) DiR loaded OLG micelles. Results are presented as mean  $\pm$  SD ( $n=3$ ).  $P < 0.01$  \*\*

A much higher fluorescence was observed in the brains of mice treated with OLG micelles compare with that treated with free DiR (Figure 48-I). Based on the fluorescence intensity (Figure 48-II), OLG micelles were able to increase the delivery of DiR to the brain by ~14.3-fold ( $P=0.008$ , student's t test) at 2 h compared with free DiR.

### 3.2.10.2 *Ex-vivo* imaging of major organs other than brain

Figure 49 and Figure 50 illustrate the distribution of DiR delivered by OG micelles or OLG micelles in other major organs at 2h following a treatment. It was found that free DiR distributed mainly to the lung, spleen, and liver with a high accumulation in the lungs while the majority of OG or OLG micelles distribute to the liver, though distribution in the lung, heart, kidney, and spleen was also observed (Figure 49-1 and Figure 50-I). The uptake of the micelles by phagocytes in the mononuclear phagocyte system was likely the explanation for the strong fluorescence observed in the liver. The fluorescence observed in the kidney was associated with the existence of GSH transporters in the kidney [151]. It appears that the total fluorescence intensity from the isolated organs of mice treated with OG or OLG micelles is stronger than that from the mice treated with free DiR (Figure 49-II and Figure 50-II).

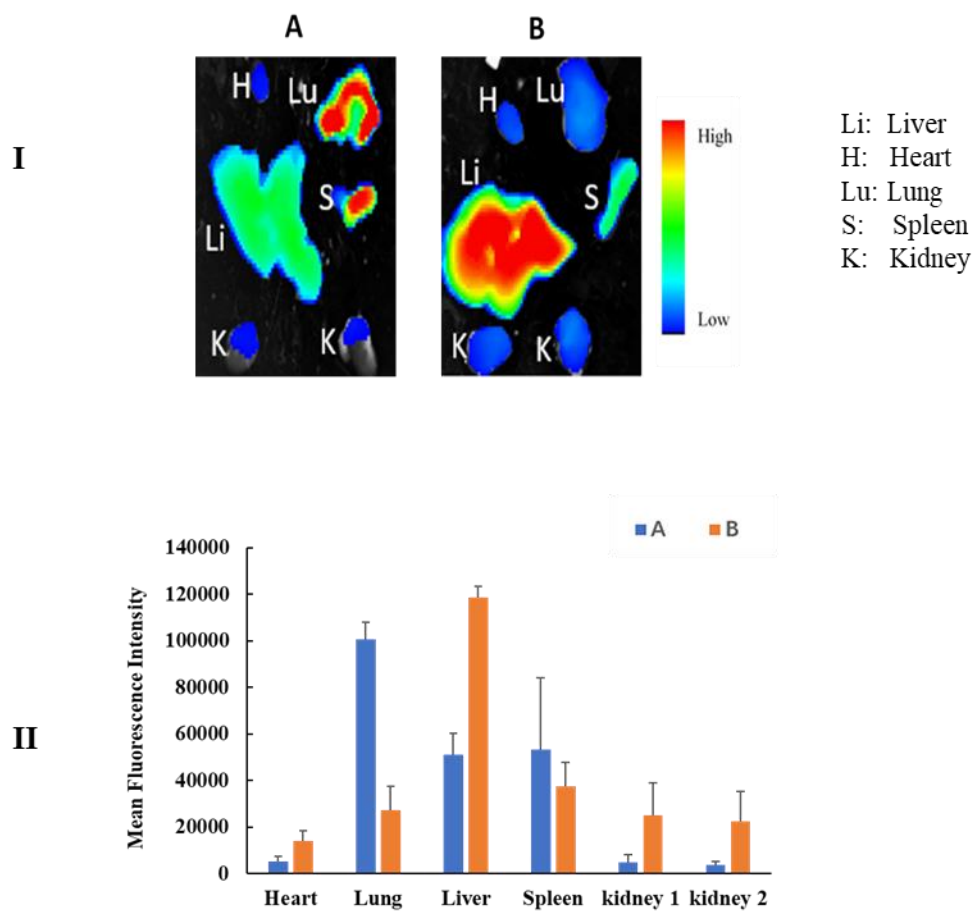


Figure 49. Representative *ex-vivo* images (**I**) and corresponding fluorescence intensities (**II**) of the organs 2 h after i.v. injection of (**A**) free DiR and (**B**) DiR loaded OG micelles. Results are presented as mean  $\pm$  SD ( $n=3$ ).

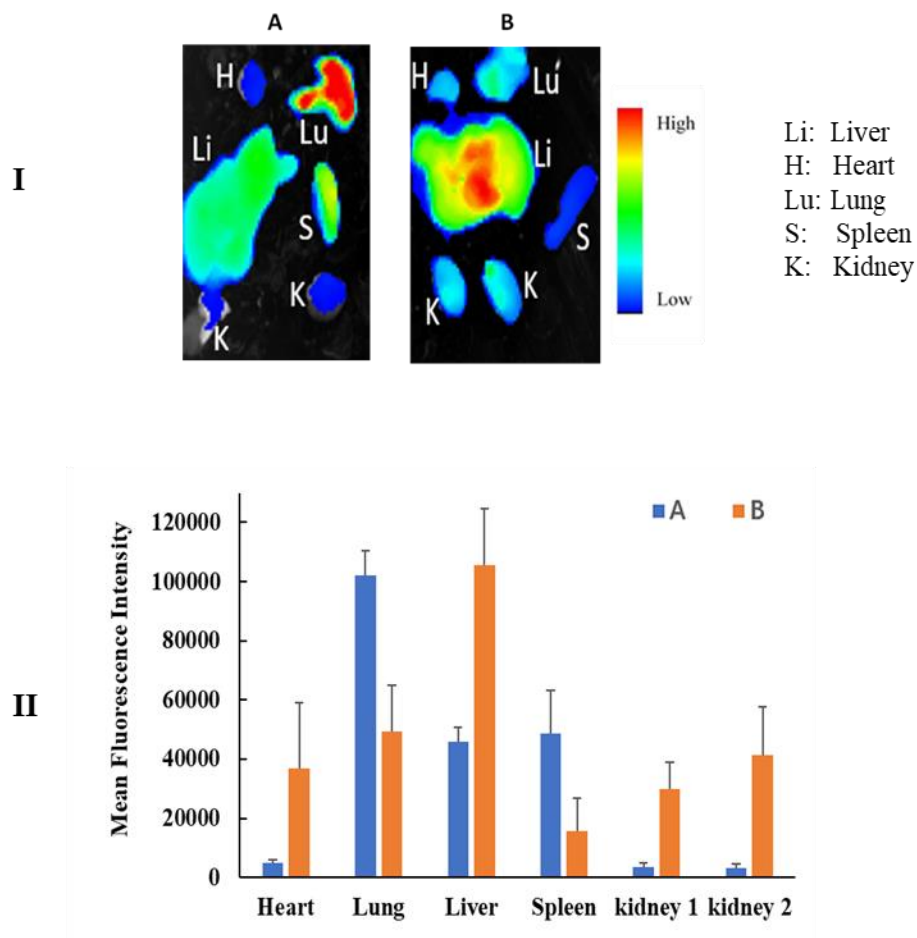


Figure 50. Representative *ex-vivo* images (**I**) and corresponding fluorescence intensities (**II**) of the organs 2 h after i.v. injection of (**A**) free DiR and (**B**) DiR loaded OLG micelles. Results are presented as mean  $\pm$  SD ( $n=3$ ).

Although our data showed OLG micelles exhibit better brain targeting effect than OG, it is not clear if the better brain targeting effect is contributed by the structure modification or by a much smaller particle size of OLG (18 nm for OLG vs 220 nm for OG).

### 3.2.11 Conclusion

The fatty alcohol modified GSH derivatives, namely OG and OLG, were successfully designed and synthesized. Both OG and OLG were able to form micelles with a

low CMC value (12.48  $\mu\text{M}$  for OG and 2.2  $\mu\text{M}$  for OLG) and both micelles were stable enough to be used as a drug delivery system. For the brain targeting effect, OLG micelles were able to deliver a maximum of  $\sim 98.3$  times more DiR to the brain than that delivered by free DiR while OG micelles delivered a maximum of  $\sim 63$  times more DiR to the brain. The brain targeting effects of these two micelles were further confirmed by *ex-vivo* imaging of the isolated brains. OLG micelles produced a  $\sim 14$ -fold increase in the delivery of DiR to the brain while OG micelles showed a  $\sim 6.4$ -fold increase based on the *ex-vivo* imaging results. Compared with DiR delivered by COXP micelles ( $\sim 20$  times more with the whole-body imaging and  $\sim 8$  fold more based on *ex-vivo* imaging), OLG micelles exhibited better brain targeting effect (maximum of  $\sim 98.3$  times more with the whole-body imaging and  $\sim 14$  fold more based on *ex-vivo* imaging). The investigation from this study validates the structural modification of a replacement of the hydrophobic structure cholesterol in COXP with a hydrophobic fatty alcohol for brain targeting micelles.

### **3.3 Methods**

#### **3.3.1 Chemicals and materials**

Unless otherwise stated, all chemicals were analytical or chromatographic grade and obtained from commercial sources.

1-octadecanol, 4-toluenesulfonyl chloride, 1,2-diaminoethane, triethylamine, pyridine, ethylene glycol, acryloyl chloride, and glutathione were acquired from Fisher Scientific (Waltham, MA, USA). Dioxane, dichloromethane, tetrahydrofuran, ethyl acetate, and hexanes were purchased from Sigma-Aldrich (St. Louis, MO, USA).

RPMI 1640 growth medium supplement with 10% FBS 100 units/ml of penicillin was obtained from Mediatech, Inc. (Hendon, VA). DMEM growth medium and Dulbecco's phosphate buffer saline (Gibco™ DPBS, without calcium and magnesium, 1x) were purchased from Fisher Scientific (Waltham, MA, USA). 3-(4, 5-Dimethylthiazol-2-yl)-2,5-diphenyl-tetrazolium bromide (MTT) was from Sigma (St Louis, MO).

DiR dye and Rhodamine B dye were products of Thermo Fisher Scientific (Waltham, MA, USA). Pyrene was obtained from lipid (Ludwigshafen, Germany).

Silica gel column (mesh 200-400) was purchased from Oakwood Products, Inc (West Columbia, SC, USA).

#### **3.3.2 Instrumentation**

Flash column chromatography was carried out on a W-Prep 2 XY Yamazen dual channel flush chromatography system (San Bruno, California).

$^1\text{H}$  NMR spectra were recorded from Bruker Varian 600 MHz spectrometer in deuterated solvents as indicated. All peaks were given as chemical shift in part per million relatives to TMS (tetramethyl saline) or DSS (4,4-dimethyl-4-silapentane-1-sulfonic acid) as an internal standard. Multiplicities are indicated by s (singlet), d (doublets), t (triplet), q (quartet), m (multiplet), and brs (broad singlet).  $J$  value are given in Hz.

The low-resolution mass spectra (LRMS or MS) were acquired on Thermoquest Finnigan LCQ Deca mass spectrometer (Waltham, MA, USA) and the high-resolution mass spectra (HRMS) were obtained on a Bruker Daltonics solariX 12 teslas Fourier Transform Ion Cyclotron Resonance mass spectrometer (Department of chemistry, University at Buffalo, NY).

FTIR spectra were obtained on Thermo NICOLET 6700 FT-IR spectrometer (Thermo Fisher Scientific, Madison, WI).

Melting points were recorded on a MEL-TEMP® melting apparatus (Electrothermal, Dubuque, IA).

Cell number and cells viability were obtained on a Nexcelom Cellometer Auto T4 Automated Cell Counter (Lawrence, MA, USA).

The particle size and zeta potential of nanoparticles were obtained from Zetasizer (Malvern instrument, Westborough, MA).

Optical properties (absorbance and fluorescence) were determined on a SpectraMax M2 microplate reader (Molecular Devices, Sunnyvale, California).

*In-vivo* and *ex-vivo* imaging was performed on a Xtreme *in-vivo* imaging (Bruker).

### 3.3.3 HPLC/MS and LC/MS/MS condition

All HPLC/MS analysis was achieved on an Agilent 1260 infinity II HPLC coupled to Agilent infinity InfinityLab MSD and a 1260 Infinity II Diode Array Detector (DAD) WR. Chromatographic separations were achieved by using Luna 3u C8(2) column (100×4.6 mm i.d., Phenomenex, Torrance, CA). The mobile phase consisted of ammonium (pH 10.6) aqueous solution (phase A) and acetonitrile (phase B) and the flow rate was kept at 1 mL/min. Phase B was initially set at 0% for 5 min, increased linearly to 90% over 20 min and held for 3 min, then returned to the initial condition over 5 min. The system was re-equilibrated for 3 min before the next injection. The temperature was set to 4 °C. The sample was injected at a volume of 5 µL with a run time of 33 min. OG or OLG was monitored at 210 nm.

The MS detection of OG or OLG achieved by selected ion monitoring (SIM) in positive mode (ESI<sup>+</sup>):  $m/z$  632.3 (ESI<sup>+</sup>) for OG and  $m/z$  720.4 (ESI<sup>+</sup>) for OLG. The following parameters of the mass spectrometer in SIM mode were used: capillary voltage, 4 KV; desolvation temperature, 330 °C; nitrogen gas flow rate, 11 L/min; optimized fragmentation voltage, 135V.

The LC/MS/MS detection of the fragmentation of OG and OLG was achieved in the positive mode with the following parameters: capillary voltage, 5.5 KV; desolvation temperature, 330 °C; nitrogen gas flow rate, 11 L/min; optimized fragmentation voltage, 135 V; collision energy, 30V. The parent ion for OG, OLG is  $m/z$  632.3 and  $m/z$  720.3, respectively.

### 3.3.4 Cells and animals

NCI-H226 cell line (human lung cancer cell line) and CV-1 cells (African green monkey kidney fibroblast cell line) were obtained from the National Cancer Institute and American Type Culture Collection (ATCC) respectively. The cells were cultured in RPMI 1640 growth medium with 10% FBS and 1% penicillin/streptomycin in a humidified atmosphere and 5% CO<sub>2</sub> at 37 °C.

Females BALB/Cj mice (6-8 weeks old, 17-20 g) and females BALB/Cj mice (2 weeks, 16 g) were purchased from Jackson Laboratory (Bar Harbor, ME, USA) and acclimatized to a laboratory condition for one week before the experiment. All animal experiments were performed according to the protocols approved by the Institutional Animal Care and Use Committee (IACUC) at South Dakota State University, Brookings, SD, USA.

Mouse kidney cells were isolated from females BALB/Cj mice (2 weeks, 16 g) by following the procedure as reported [186, 192-194]. Cells were maintained in a DMEM growth medium supplement with 10% FBS and 1% penicillin-streptomycin in a 5% CO<sub>2</sub> incubator at 37 °C.

### 3.3.5 Synthesis of OG or OLG

#### 3.3.5.1 Synthesis of OG

- i. Synthesis of octadecyl acrylate (Scheme 4, compound A1).*

To a stirred solution of octadecanol (1.5 g 5.5 mmol) in a mixed solvent of anhydrous tetrahydrofuran (15 mL) and anhydrous methylene chloride (15 mL) was added dropwise acryloyl chloride (0.448 mL, 5.5 mmol) and triethylamine (0.837 mL).

The reaction was stirred at room temperature for 2 h before solvent removal using a rotary evaporator under a reduce pressure. The desired compound was purified by a silica gel column using hexanes/ethyl acetate to produce a white oil product in 44.1% yield.

The compound was characterized by  $^1\text{H}$  NMR (600 MHz,  $\text{CDCl}_3$ )  $\delta$  6.38 (m, 1H), 6.23 – 6.02 (m, 1H), 5.89 – 5.69 (m, 1H), 4.32 – 3.94 (m, 2H), 1.67 (dd,  $J = 13.1, 6.4$  Hz, 2H), 1.48 – 1.09 (m, 30H), 0.88 (t,  $J = 6.0$  Hz, 3H).

ii. *Synthesis of N5-(1-((carboxymethyl)amino)-3-((3-(octadecyloxy)-3-oxopropyl)thio)-1-oxopropan-2-yl)glutamine (Scheme 4, compound OG)*

GSH (0.75 g, 2.4 mmol), sodium carbonate (0.258 g, 2.43 mmol), and compound C2 (0.79 g, 2.4 mmol) were dissolved and stirred in a mixed solution of tetrahydrofuran (28 mL) and water (32 mL) at room temperature overnight, then the solvents were removed by lyophilization. Crude OG was purified through precipitation using a gradient of water (pH 4)/acetonitrile to produce white powder (yield. 21%). The compound was characterized with FTIR, MS and HRMS.

### 3.3.5.2 Synthesis of OLG

i. *Synthesis of octadecyl 4-methylbenzenesulfonate (Scheme 5, compound B1)*

1-Octadecanol (8 g, 29 mmol), *p*-toluenesulfonylchloride (5 g, 26 mmol), triethylamine (6 mL), pyridine (4 mL) were dissolved in anhydrous dichloromethane (60 mL). The mixture was allowed to stir at room temperature for 4 h in the presence of catalytic amounts of 4-(dimethylamino)pyridine (DMAP) before solvent removal using a rotary evaporator under a reduce pressure. The compound was purified using a silica gel column (mesh 200-400) with hexanes/ethyl acetate to yield compound B1 as a white

powder in 35% yield. The compound was characterized by  $^1\text{H}$  NMR (600 MHz,  $\text{CDCl}_3$ )  $\delta$  7.79 (dd,  $J = 11.2, 4.5$  Hz, 2H), 7.33 (t,  $J = 6.8$  Hz, 2H), 4.17 – 3.89 (m, 2H), 2.47 (dd,  $J = 42.2, 20.4$  Hz, 3H), 1.66 – 1.59 (m, 2H), 1.23 (d,  $J = 27.7$  Hz, 30H), 0.92 – 0.84 (m, 3H).

ii. *Synthesis of 2-(2-(octadecyloxy) ethoxy)ethan-1-ol (Scheme 5, compound B2)*

Compound B1 (4 g, 9.7 mmol) was mixed together with diethylene glycol (38 mL, 400 mmol) in 40 mL anhydrous dioxane and stirred under reflux conditions for 48 h. the solvents were removed using a rotary evaporator under a reduce pressure. The crude was purified using a silica gel column (mesh 200-400) with hexanes/ethyl acetate to yield compound B2 as a white powder in 63% yield. The compound was characterized by  $^1\text{H}$  NMR (600 MHz,  $\text{CDCl}_3$ )  $\delta$  3.75 – 3.52 (m, 8H), 3.48 – 3.40 (m, 2H), 1.57 (d,  $J = 6.5$  Hz, 2H), 1.25 (m, 30H), 0.87 (t,  $J = 6.9$  Hz, 3H).

iii. *Synthesis of 2-(2-(octadecyloxy) ethoxy)ethyl acrylate (Scheme 5, compound B3)*

To a stirred solution of compound B3 (2 g, 5.6 mmol) in 30 mL anhydrous dichloromethane (30 mL) was add dropwise acryloyl chloride (0.88 mL, 11.2 mmol) and triethylamine (1.2 mL). the reaction was stirred at room temperature for 5 min before solvent removal using a rotary evaporator under a reduceD pressure. The resulting residue was purified by a silica gel column (mesh 200-400) with hexanes/ethyl acetate to yield compound B3 as a with oily product in 43% yield. The pure compound was characterized by  $^1\text{H}$  NMR (600 MHz,  $\text{CDCl}_3$ )  $\delta$  6.43 (d,  $J = 17.3$  Hz, 1H), 6.23 – 6.08 (m, 1H), 5.83 (d,  $J = 10.5$  Hz, 1H), 4.36 – 4.27 (m, 2H), 3.80 – 3.69 (m, 2H), 3.68 – 3.62

(m, 2H), 3.62 – 3.54 (m, 2H), 3.50 – 3.39 (m, 2H), 1.63 – 1.49 (m, 2H), 1.46 – 1.16 (m, 30H), 0.88 (t, J = 6.7 Hz, 3H).

iv. *Synthesis of 2-amino-7-((carboxymethyl)carbamoyl)-5,12-dioxo-13, 16,19-trioxa-9-thia-6-azaheptatriacontanoic acid (Scheme 5, OLG)*

GSH (0.89 g, 2.88 mmol), sodium carbonate (0.314 g, 2.88 mmol), and compound B3 (1 g, 2.4 mmol) was dissolved in a mixed solution of tetrahydrofuran (14 mL) and water (12 mL) at room temperature for 4 h. OLG was purified through precipitation using formic acid (0.1%) water and separated by centrifugation, then the compound was further purified by washing three time with 0.1% formic acid water and ethyl acetate respectively to yield white powder product in 60% yield. The compound was characterized by FTIR, MS, HRMS

### 3.3.6 Purity determination

Stock solutions of OG or OLG (1 mg/mL) were prepared by dissolving OG or OLG in a solution of methanol and ammonium water (1:1 v/v, pH 10.2). The purity of OG or OLG (1mg/mL) was checked by HPLC with a comparison to blank solvent (methanol and ammonium water (1:1 v/v, pH 10.2)).

### 3.3.7 *In vitro* cell cytotoxicity

The cytotoxicity of OG or OLG against CV-1 cells and NCI-H226 cells was measured using the MTT assay. Briefly, cells were seeded in a 96-well plate at a density of 3000 cells per well and incubated in RPMI 1640 growth medium at 37 °C for 24 h. After 24 h, the growth medium was replaced with the fresh medium solution with a series of OG or OLG concentration and continue to incubate for another 24 h. Subsequently,

cell viability was determined with the standard MTT assay. The absorbance (Abs) of each well was measured at 490 nm by a microplate reader. Cell viability was calculated by Eqs. (1):

$$Cell\ viability\ (\%) = \frac{Abs_{sample} - Abs_{blank}}{Abs_{control} - Abs_{blank}} \times 100 \quad (1)$$

### 3.3.8 CMC determination (use the same procedure I edited earlier)

The CMC of OG or OLG in an aqueous solution was determined using pyrene as a fluorescent probe by following the procedure as described [195]. Briefly, 1.5  $\mu$ L of 0.2 mM pyrene ethanol solution was placed in a vial containing 1mL each OG solution at different concentrations (0.00001 mg/mL to 1 mg/mL). After mixing, the fluorescence spectrum was recorded on a fluorescence spectrometer with the excitation wavelength of 334 nm, and the fluorescence intensities of the peaks at  $\sim$ 375 nm ( $I_1$ ) and  $\sim$ 384 ( $I_3$ ) were extracted from the spectra. A plot of  $I_3/I_1$  against the logarithm of OG concentration was made and the intersection of the two straight lines of the plot is the CMC value.

The same method was used to determine the CMC values of OLG.

### 3.3.9 Preparation of DiR loaded micelles

DiR loaded micelles were prepared by a film-dispersion method. Briefly, 7 mg of OG or OLG and 0.25 mg (5  $\mu$ L, 5 mg/mL in ethanol) of DiR were dissolved in 50  $\mu$ L ethanol and vortexed to mix. The ethanol was completely evaporated under a gentle stream of nitrogen. The residue was dissolved in 1mL DPBS (no calcium, no magnesium, 1x) to a concentration of 7 mg/mL of OG or OLG. The mixture was subjected to sonication for 30 min with a 5 min break in a water bath at 40  $^{\circ}$ C, followed

by centrifugation at 14000 rpm for 10 min to remove insoluble DiR to produce DiR loaded OG or OLG micelles [196].

### 3.3.10 Preparation of Rhodamine B loaded micelles

Rhodamine B loaded OG OR OLG micelles were prepared for the following cell uptake study and *in vitro* release study. The method for preparing Rhodamine B loaded OG or OLG micelles was same with preparing DiR loaded OG or OLG micelles except Rhodamine B was used in place with DiR.

### 3.3.11 Characterization of DiR loaded micelles

The particle size and zeta potential (surface charge) of DiR loaded OG or OLG micelles were measured by dynamic light scattering using on a Malvern Zetasizer. Briefly, DiR loaded micelles were freshly prepared. The solution was then diluted with deionized water (0.5:100) before the measurement of particle size and zeta potential.

### 3.3.12 Determination of DiR encapsulation efficiency and loading capacity

The encapsulation efficiency (EE%) and loading capacity (LC%) of DiR were estimated by extracting DiR from DiR loaded OG or OLG micelles with ethanol. The concentration of DiR was measured by fluorescence intensity obtained using a fluorescent microplate reader with the excitation wavelength and emission wavelength of 730 nm and 780 nm, respectively. A calibration curve was constructed by spiking a known concentration of DiR to blank micelles. The EE% and LC% were calculated by the Eqs. 2 and Eqs. 3 below:

$$EE\% = \frac{\text{weight of DiR loaded in micelles}}{\text{weight of total DiR used for encapsulation}} \times 100 \quad (2)$$

$$LC\% = \frac{\text{weight of DiR loaded in micelles}}{\text{weight of micelles}} \times 100 \quad (3)$$

### 3.3.13 Storage stability of DiR loaded micelles

The storage stability of DiR loaded micelles was checked at 4 °C. Briefly, fresh DiR loaded micelles were prepared as described above and stored at 4 °C. Each sample (5 µL) were drawn followed by dilution with deionized water (0.5:100). The stability was determined by measuring the particle size as described before.

### 3.3.14 Rhodamine B *in vitro* release study

The *in vitro* release studies of Rhodamine B was conducted with Rhodamine B loaded OG or OLG micelles in PBS buffer (pH 7.4, 0.1 M). OG or OLG Rhodamine B micelles (4.7 µg Rhodamine B /mL, 0.5 mL) was added into a pre-swollen dialysis bag (molecule weight cut-off: 10 kDa) and put into plastic tube containing 40 mL PBS (pH 7.4). The plastic tube was then placed in an incubator shaker with temperature maintained at 37 °C and shaken horizontally at the speed of 100 rpm. At predetermined time intervals (0, 0.25, 0.5, 1, 2, 4, 6, 10, 24 h), aliquots (3 mL) of sample solution were withdrawn and the same volume of the fresh PBS buffer was added back to maintain the volume of releasing medium. The amount of Rhodamine B was determined by HPLC with a UV detector (550 nm). Meanwhile, the release study of Rhodamine B from ethanol solution was performed for comparison.

### 3.3.15 Cellular uptake of Rhodamine B

For cellular uptake study, the isolated mouse kidney cells (2<sup>nd</sup> passage) were seeded in 96-well plate at a density of ~ 5000 cells/well. When the cells reach 90% confluence, the culture medium was removed, and cells were treated with culture medium

only (no inhibitor), probenecid (1 mM) for 30 min followed by a replacement of the medium containing Rhodamine B loaded OG or OLG micelles (116  $\mu\text{g}/\text{mL}$ ) or Rhodamine B loaded OG or OLG micelles (116  $\mu\text{g}/\text{ml}$ ) plus probenecid (1 mM) for additional 30 min at 37 °C before removal of the medium. Then, the cells were washed three times with DPBS, and cellular uptake was measured by fluorescence intensity using fluorescence microplate reader ( $\lambda_{\text{ex}}$  540 nm,  $\lambda_{\text{em}}$  625 nm). The data were expressed as a percentage of control (n = 3).

### **3.3.16 *In vivo* animal study**

*In vivo* animal study was carried with females BALB/Cj mice (6-8 weeks old, 17-20 g) with the procedure evaluated and approved by the Institutional Animal Care and Use Committee (IACUC) at South Dakota State University, Brookings, SD, USA.

The mice were randomly divided into 2 groups with 3 mice in each group and intravenously administered with free DiR solution (25  $\mu\text{g}/\text{mL}$ ) and DiR loaded OG or OLG micelles through a tail vein injection, respectively.

All the injected dose was adjusted based on the determined encapsulation ratio (EE%) of DiR loaded micelles to make sure that each mouse was received with the same amount of DiR.

#### **3.3.16.1 Whole-body fluorescence images of mice**

To acquire the whole-body fluorescence images of mice, the mice were anesthetized with a gas mixture of oxygen and isoflurane at predetermined time intervals (15 min, 30 min, 1h, 2 h, 4 h, 6 h, 12 h, and 24 h) after administered with DiR loaded micelles or free DiR. The fluorescence images of whole-body were obtained on a Bruker

Xtream *in-vivo* imager ( $\lambda_{\text{ex}}$  730 nm,  $\lambda_{\text{em}}$  790 nm), and the fluorescence intensity was quantified using the Bruker MI SE software.

### **3.3.16.2 *Ex-vivo* brain and organs imaging of mice**

To get the distribution of micelles in brain and other organs (liver, heart, lung, spleen, and kidney), the mice were sacrificed at 2 h post tail vein injection of DiR loaded micelles or free DiR, and the heart was perfused with DPBS to remove blood in tissues before the brain and organs was removed. The fluorescence images of brain and other organs were obtained on Bruker Xtream *in-vivo* imager ( $\lambda_{\text{ex}}$  730 nm,  $\lambda_{\text{em}}$  790 nm) and the fluorescence intensity was quantified using the Bruker MI SE software as well.

### **3.3.17 Statistics**

Data were reported as mean  $\pm$  standard deviation (SD). Student's *t*-test was used for two group comparison and one-way ANOVA was used for multiple group comparison by analyzed with GraphPad Prism 8, Excel, or R software. *P*-value of less than 0.05, 0.01 or 0.001 was considered as statistically significant.

## CHAPTER 4. CONCLUSION AND FUTURE PLAN

### 4.1 Conclusion

The BBB is a highly selective barrier between blood and brain and formed by endothelial cells of the capillary wall, astrocyte end-feet, and pericytes. The BBB is a protection mechanism that limits exogenous compounds from entering the brain. However, it is this barrier that causes most treatment failure for brain diseases since it limits a drug molecule from entering the brain to achieve its effective therapeutic concentration. Extensive research efforts have been made to improve drug delivery to the brain.

Although the BBB limits exogenous molecules from entering the brain, it allows endogenous molecules to enter the brain to meet the brain's need. The endogenous molecules can enter the brain through the aid of their corresponding transporters or receptors. Successes have been made by using a ligand or a ligand derivative of these transporter/receptors present in the BBB as a brain targeting agent to aid the delivery of a drug to the brain.

GSH is an endogenous molecule and transported to the brain through a GSH transporter in the BBB. GSH transporters are richly expressed in the BBB with a limited presence in other tissues except the kidneys. The unique brain distribution of GSH transporters in the BBB provides the rational basis for using GSH or a GSH analog as a brain targeting agent.

In our previous work, we have successfully demonstrated COXP as a brain targeting agent. COXP was formed by connecting a molecule of GSH to a molecule of cholesterol through a two-ethylene glycol unit linker. The amphiphilic nature of COXP

(hydrophilic GSH and hydrophobic cholesterol) enables the molecule to self-assemble to form a micelle (COXP micelle). Through the whole-body imaging technique, COXP micelles were demonstrated to deliver DiR to the brain ~20 folds more when compared with DiR in the brain from free DiR.

The aim of this dissertation was to determine if structural modification of the structures other than the GSH part of COXP can lead to a brain targeting agent, and, by maintaining its amphiphilic nature, brain targeting micelles.

In this dissertation, the structural modification was conducted by involving two parts of the COXP structure: i). replacement of the linker between GSH and cholesterol; ii). replacement of the hydrophobic cholesterol structure with a hydrophobic fatty alcohol. All designed compounds remain to be an amphiphilic molecule.

We have demonstrated both structural modifications led to molecules that can form micelles effectively and these micelles were stable with a low  $\mu\text{M}$  CMC value. All micelles were effective brain targeting micelles. Further, both structural modifications could lead to more effective brain targeting micelles than COXP micelles. The most effective brain targeting micelles (CNLG micelles) from the structural modification of the linker exhibited the ability to deliver DiR to the brain ~40 folds more compared with free DiR while the most effective brain targeting micelles (OLG micelles) from the replacement of cholesterol with stearyl alcohol exhibited the ability to deliver DiR to the brain as high as ~90 folds more when compared with free DiR, significantly higher than the 20-fold increase achieved by COXP micelles. By using mouse kidney cells, we demonstrated that the micelles were taken to the cells by a GSH transporter.

This dissertation not only validate that our design strategy to use GSH to develop brain targeting agents and brain targeting micelles but also confirm that the structural modifications of the linker and the cholesterol part of COXP are valid structural modifications and can lead to more effective brain targeting agents and brain targeting micelles.

Compared with previously reported uses of GSH to develop brain targeting drug delivery systems that include to link GSH to PEG[203] or to link GSH to bovine serum albumin nanoparticles[204], our compounds were derived from linking a molecule of GSH to a molecule of cholesterol or to stearyl alcohol. Cholesterol and stearyl alcohol are quite different than PEG or BSA in terms of the chemical structure and hydrophobicity. Both cholesterol and stearyl alcohol are hydrophobic while PEG and BSA are hydrophilic. When compared with an addition of a hydrophilic structure to a molecule, addition of a hydrophobic structure to a molecule in general will produce significantly different physical chemical impacts which in turn will impact pharmaceutical properties. Specifically, use of cholesterol or stearyl alcohol in our molecules leads to following two novel features : 1) resulting in an amphiphilic molecule that is capable of undergoing self-assembly to form a micelle with its surface fully covered with GSH as a ligand for the GSH transporter for brain targeting. The maximum coverage of the surface with the brain targeting ligand GSH properly contributes to the outstanding brain-targeting of the micelles. To our knowledge, no GSH brain targeting agent that can undergo self-assembly to form brain targeting micelles has been reported. Most importantly, our work demonstrates that our micelles exhibit an excellent brain targeting efficiency compared with most literature reported brain targeting delivery systems (~4-5-fold increase). 2)

Both cholesterol and stearyl alcohol are cheap and readily available from commercial sources, which makes it easy for scale-up production of micelles if clinical trials are warranted.

It needs to be noted that one of the advantages of CNLG micelles is its pH-sensitive release: more release at pH 4.5 than pH 7.4. This property helps increase the blood circulation half-life of the micelles since the pH of blood is 7.4. When the micelles are transported into the brain by the GSH transporter, they are most likely to be in lysosomes through a transporter mediated endocytosis pathway instead of transcytosis pathway as reported for other transporters [205, 206]. The acidic pH (4.5-5.0) in lysosomes helps promote the release from the micelles.

Several limitations are associated with our studies. One of the limitations is the selection of free DiR as a control in our animal studies. The pharmacokinetic (PK) properties of free DiR could be quite different than DiR encapsulated in the micelles. Ideally, we should have used a control in which DiR was encapsulated in a micelle and the micelle had the same negative charge, same particle size, but had no GSH on the surface. Unfortunately, it is challenging to find such a control. For this reason, free DiR has been used as a common control in other brain-targeting studies[201, 207, 208].

Nevertheless, the different PK properties of free DiR and DiR encapsulated in our micelles would definitely affect the brain distribution. It is not clear at this point if the PK difference would make a positive or negative contribution to the brain targeting effect. However, we can be confident to conclude that our micelles exhibited the brain targeting effect since the brain targeting effect of the micelles was significant even at the early time point (15 min) when PK's impact would be minimal. Regardless, a PK study

on free DiR and DiR encapsulated in our micelles is needed to clarify the roles of PK on the micelles' brain-targeting effect.

The other limitation of this dissertation is the use of whole-body imaging results as a parameter to compare the brain targeting effects for our micelles' drug delivery systems. It is noted that the ratios obtained from the *ex vivo* experiment were much lower than the whole-body brain imaging. In general, the ratio obtained from the isolated brains should be a more accurate reflection of brain-targeting selectivity, since the fluorescence intensity obtained from the whole-body imaging could be affected by various factors. However, fluorescence intensity ratios obtained from the whole-body imaging have been a commonly used parameter reported for brain-targeting. To be consistent with the literature, we used the whole-body imaging results for comparison. In the meantime, we also obtained the *ex vivo* data.

## **4.2 Future plan**

It needs to be noted that only three derivatives were made with the structural modification of the linker and two derivatives were prepared with the structural replacement of the cholesterol structure in this dissertation. The dissertation basically provides a proof of concept that structural modification of the linker and replacement of cholesterol with another hydrophobic molecule are valid and effective structural modifications. We are confident that more effective brain targeting agents and brain targeting micelles can be identified through the structural modification of the linker and the cholesterol part of COXP. Therefore, one of the future focuses will be to continue the structural modification to identify more effective brain targeting agents and brain targeting micelles through these two structural modifications.

Since our work only demonstrates that the brain targeting micelles delivered DiR to the brain, data are needed to demonstrate that the brain targeting micelles can deliver a therapeutic agent to the brain to treat a brain disease. Therefore, another plan is to conduct an investigation to demonstrate that the micelles can deliver a therapeutic to the brain to treat a brain disease, such as brain cancer. Further, we demonstrated earlier that COXP could be used to prepare brain targeting liposomes (COXP liposomes). The ability of newly designed brain targeting GSH derivatives in preparing brain targeting liposomes will be investigated as well.

## CHAPTER 5. PHARMACOKINETIC CONSIDERATIONS IN THE DEVELOPMENT OF THERAPEUTICAL MONOCLONAL ANTIBODIES COMPARED WITH SMALL-MOLECULE DRUGS

Due to the confidentiality of this part of work from Food and Drug administration (FDA), only a summary is presented, and it does not reflect the official views of FDA.

### 5.1 Introduction

Monoclonal antibody (mAbs) are identical immunoglobulin that are produced by B-cell and can specifically target at a unique epitope on a single antigen. Since the first therapeutic mAb, muromonab-CD3 (Orthoclone OKT3) was approved by FDA in 1986, at least 570 therapeutic mAbs have been studied in clinical trials around the world and about 94 therapeutic mAbs have been approved by either US or EU [209].

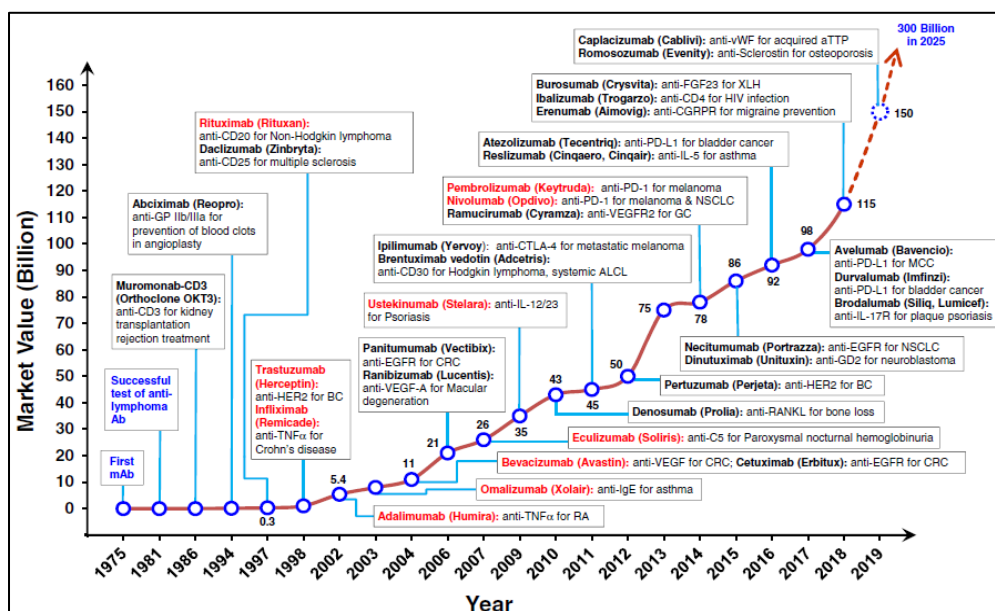


Figure 51. Development of antibody therapeutics and their applications. Adapted from Ref [210].

The important role of therapeutic mAbs is apparent since they have been applied in a wide variety of therapeutic areas, including oncology or non-oncology (inflammatory disease and hematological disease) as shown in Figure 51. In particular, numerous mAbs have been developed or repurposed for either the treatment or prevention of COVID-19 since the COVID-19 pandemic broke out in early 2020. Emergency use authorizations (EUAs) have been granted for monoclonal antibody therapies for the treatment mild-to-moderate COVID-19 in adults and certain pediatric patients. These therapies include REGEN-COV (casirivimab and imdevimab administered together) and bamlanivimab and etesevimab administered together. Therefore, the potential of mAbs in the future drug development market cannot be underestimated.

Compared with small-molecule drugs used in a conventional therapy, therapeutic mAbs can increase the efficacy of treatment or reduce the potential side effects due to their high target specificity through directly working on their targets or indirectly via antibody-dependent cellular toxicity (ADCC) or cell-dependent cytotoxicity (CDC). mAbs differ from small-molecule drugs not only in their pharmacological mechanism but also in their pharmacokinetic properties. In this chapter, clinical pharmacokinetic properties of therapeutic mAbs will be discussed.

## **5.2 Route of Administration and Absorption of mAbs**

mAbs are most commonly administered via the intravenous route. They are also possible to be administered via subcutaneous or intramuscular route, but it generally takes a few days to reach the peak plasma concentration due to the slow absorption into the systemic circulation, since adsorption of mAbs is triggered by the lymphatic system. In addition, the bioavailability of mAbs after subcutaneous and intramuscular administration

is often low as a result of the proteolytic degradation of the mAbs in the interstitial fluid or the lymphatic system.

Compared with a small-molecule drug, oral administration of mAbs is infeasible due to their large size, high hydrophilicity and instability resulting from gastrointestinal degradation, which leads to the inadequate bioavailability.

### 5.3 Distribution of mAbs

Given their unique physicochemical property and large size, the distribution of mAbs from blood into the tissue cannot be achieved by passive diffusion. Extravasation process for mAbs mainly occurs through convective transport that is driven by the osmotic pressure between blood and tissue and the sieving effect of paracellular pores (Figure 52). In case where convection extravasations is limited in tissues, neonatal Fc receptor mediated transcytosis through vascular epithelial cells is likely to be the key distribution mechanism for mAbs.

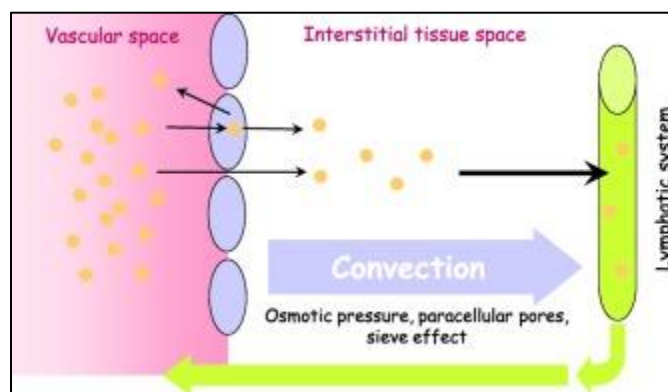


Figure 52. Convective extravasation as a major distribution process for monoclonal antibodies. Adapted from Ref [211].

Unlike a small-molecule drug that can be distributed in almost any tissues depending on their physicochemical characteristic, mAbs mainly distribute in plasma and extracellular fluid since their large size and hydrophilic properties prevent them from distribution to tissues, resulting in the low volumes of distribution that is similar with the volume of plasma. Another reason that account for the low volumes of distribution of mAbs is the slow distribution mechanism form systemic circulation to tissues.

#### **5.4 Metabolism of mAbs**

Most of small-molecule drugs are metabolized via cytochrome p450 (CYP) and UDP-glucuronosyltransferase (UGT) enzyme in the liver. However, unlike a small-molecule drug, mAbs are usually metabolized to peptides and amino acids via catabolism, and these metabolites will be reabsorbed for *de novo* synthesis of proteins.

#### **5.5 Elimination of mAbs**

mAbs are too large to be eliminated through kidney or excreted into urine except in a disease condition while the main elimination route for small-molecule drugs is by kidney.

Several mechanisms for elimination of mAbs have been proposed. First, similar with elimination of endogenous IgG, the unspecific elimination route after catabolic metabolism of antibody is pinocytosis uptake that present in the endothelial cells. This route can happen throughout the body instead of a specific organ and tissue. Second, another nonspecific elimination pathway similar with endogenous IgG occurs through internalization and subsequent degradation by lysosomes within the immune system after binding of Fc domain of the antibody to Fc-gamma-receptors (Fc $\gamma$ Rs) present on the immune cells (i.e., macrophages, monocytes, dendritic cells). Last but not the least,

elimination through target-mediated drug disposition (TMDD) after binding of Fab domain of mAbs to a specific target antigen located on cells, meaning the internalization and subsequent lysosome degradation take place within the target cells. mAbs eliminated via TMDD exhibit dose-dependent elimination, since at the higher dose and concentration of mAbs, the target antigen will be saturated and thereby resulting in nonlinear elimination.

It is worth noting the special salvage pathway exists to protect the IgG from subsequent catabolic metabolism after pinocytotic uptake by endothelial cells in order to maintain the normal plasma concentration of IgG (12 mg/mL) to provide long-term immunity that can be reflected by the long elimination half-life of IgG (~21 days).

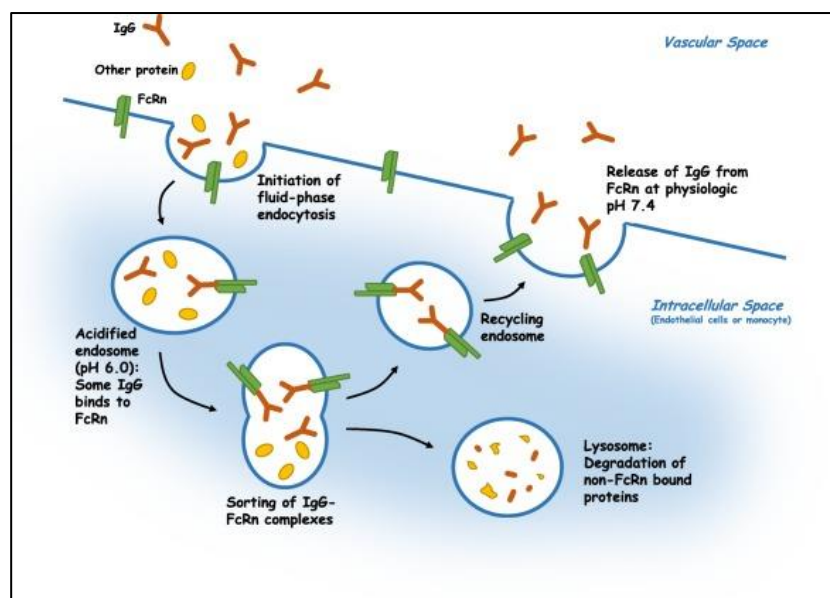


Figure 53. FcRn-mediated recycling protection mechanism of IgG. Adapted from Ref [212].

This protection mechanism is achieved through binding of neonatal Fc receptor (FcRn) to nonspecific Fc domain of IgG that takes place in acidified endosome (Figure

53). In general, at the therapeutic dosage of mAb, it is not likely to saturate FcRn-mediated recycling protection mechanism, since the plasma concentration of mAbs is far lower than that of endogenous IgG.

## **5.6 Conclusion**

Unlike a small-molecule drug, the pharmacokinetic behavior of mAbs are complex and could be affected by multiple elimination mechanisms, thereby resulting in both linear pharmacokinetic behavior and non-linear pharmacokinetic behavior. Knowledge of the pharmacokinetic of therapeutical mAbs is able to help the development as well as the optimization of therapeutic mAbs for clinical use.

## **References**

1. Abbott, N.J., et al., *Structure and function of the blood-brain barrier*. Neurobiol Dis, 2010. **37**(1): p. 13-25.

2. Buckner, R.L., J.R. Andrews-Hanna, and D.L. Schacter, *The brain's default network: anatomy, function, and relevance to disease*. Ann N Y Acad Sci, 2008. **1124**: p. 1-38.
3. Ehrlich, P., *Beitrage zur Kenntnis der granulierten. Bindegewebszellen und der eosinophilen Leukozyten*. Arch Anat Physiol, 1879. **3**: p. 166-169.
4. Goldmann, E.E., *Vitalfärbung am Zentralnervensystem: Beitrag zur Pathologie des Plexus chorioideus und der Hirnhäute*. 1913: Königl. Akademie der Wissenschaften.
5. Brightman, M. and T. Reese, *Junctions between intimately apposed cell membranes in the vertebrate brain*. The Journal of cell biology, 1969. **40**(3): p. 648-677.
6. Reese, T. and M.J. Karnovsky, *Fine structural localization of a blood-brain barrier to exogenous peroxidase*. The Journal of cell biology, 1967. **34**(1): p. 207-217.
7. Saunders, N.R., *Development of the Blood—Brain Barrier to Macromolecules*, in *Barriers and Fluids of the Eye and Brain*, M.B. Segal, Editor. 1992, Macmillan Education UK: London. p. 128-155.
8. Grontoft, O., *Intracranial haemorrhage and blood-brain barrier problems in the new-born; a pathologico-anatomical and experimental investigation*. Acta Pathol Microbiol Scand Suppl, 1954. **100**: p. 8-109.
9. Ballabh, P., A. Braun, and M. Nedergaard, *The blood–brain barrier: an overview: structure, regulation, and clinical implications*. Neurobiology of disease, 2004. **16**(1): p. 1-13.
10. Luissint, A.-C., et al., *Tight junctions at the blood brain barrier: physiological architecture and disease-associated dysregulation*. Fluids and Barriers of the CNS, 2012. **9**(1): p. 1-12.
11. Abbott, N.J., *Astrocyte–endothelial interactions and blood–brain barrier permeability*. Journal of anatomy, 2002. **200**(5): p. 523-534.
12. Löscher, W. and H.J.N.R.N. Potschka, *Drug resistance in brain diseases and the role of drug efflux transporters*. 2005. **6**(8): p. 591.
13. Löscher, W. and H. Potschka, *Role of drug efflux transporters in the brain for drug disposition and treatment of brain diseases*. Progress in neurobiology, 2005. **76**(1): p. 22-76.
14. Lai, C.-H. and K.-H. Kuo, *The critical component to establish in vitro BBB model: Pericyte*. Brain research reviews, 2005. **50**(2): p. 258-265.
15. Gonul, E., et al., *Early pericyte response to brain hypoxia in cats: an ultrastructural study*. Microvascular research, 2002. **64**(1): p. 116-119.
16. Dore-Duffy, P., et al., *Pericyte migration from the vascular wall in response to traumatic brain injury*. Microvascular research, 2000. **60**(1): p. 55-69.
17. Dixit, S., et al., *Transferrin receptor-targeted theranostic gold nanoparticles for photosensitizer delivery in brain tumors*. Nanoscale, 2015. **7**(5): p. 1782-1790.
18. Hawkins, B.T. and T.P. Davis, *The blood-brain barrier/neurovascular unit in health and disease*. Pharmacological reviews, 2005. **57**(2): p. 173-185.
19. Tao-Cheng, J.-H. and M.W. Brightman, *Development of membrane interactions between brain endothelial cells and astrocytes in vitro*. International Journal of Developmental Neuroscience, 1988. **6**(1): p. 25-37.

20. Holash, J., D. Noden, and P. Stewart, *Re - evaluating the role of astrocytes in blood - brain barrier induction*. Developmental dynamics, 1993. **197**(1): p. 14-25.
21. Tao-Cheng, J.-H., Z. Nagy, and M.W. Brightman, *Tight junctions of brain endothelium in vitro are enhanced by astroglia*. Journal of Neuroscience, 1987. **7**(10): p. 3293-3299.
22. Abbott, N.J., L. Rönnbäck, and E. Hansson, *Astrocyte–endothelial interactions at the blood–brain barrier*. Nature reviews neuroscience, 2006. **7**(1): p. 41-53.
23. Shulman, R.G., F. Hyder, and D.L. Rothman, *Cerebral metabolism and consciousness*. Comptes rendus biologiques, 2003. **326**(3): p. 253-273.
24. Paemeleire, K., *The cellular basis of neurovascular metabolic coupling*. Acta neurologica belgica, 2002. **102**(4): p. 153-157.
25. Winkler, M.K., et al., *Impaired neurovascular coupling to ictal epileptic activity and spreading depolarization in a patient with subarachnoid hemorrhage: possible link to blood–brain barrier dysfunction*. Epilepsia, 2012. **53**: p. 22-30.
26. Petty, M.A. and J.G. Wettstein, *Elements of cerebral microvascular ischaemia*. Brain Res Brain Res Rev, 2001. **36**(1): p. 23-34.
27. Cederberg, H.H., N.C. Uhd, and B. Brodin, *Glutamate efflux at the blood-brain barrier: cellular mechanisms and potential clinical relevance*. Arch Med Res, 2014. **45**(8): p. 639-45.
28. Bernacki, J., et al., *Physiology and pharmacological role of the blood-brain barrier*. Pharmacol Rep, 2008. **60**(5): p. 600-22.
29. Medbø, J.I. and O.M. Sejersted, *Plasma potassium changes with high intensity exercise*. J Physiol, 1990. **421**: p. 105-22.
30. Bradbury, M.W., et al., *THE DISTRIBUTION OF POTASSIUM, SODIUM, CHLORIDE AND UREA BETWEEN LUMBAR CEREBROSPINAL FLUID AND BLOOD SERUM IN HUMAN SUBJECTS*. Clin Sci, 1963. **25**: p. 97-105.
31. Hansen, A.J., *Effect of anoxia on ion distribution in the brain*. Physiol Rev, 1985. **65**(1): p. 101-48.
32. Jeong, S.M., et al., *Changes in magnesium concentration in the serum and cerebrospinal fluid of neuropathic rats*. Acta Anaesthesiol Scand, 2006. **50**(2): p. 211-6.
33. Nischwitz, V., A. Berthele, and B. Michalke, *Speciation analysis of selected metals and determination of their total contents in paired serum and cerebrospinal fluid samples: An approach to investigate the permeability of the human blood-cerebrospinal fluid-barrier*. Anal Chim Acta, 2008. **627**(2): p. 258-69.
34. Wang, L., et al., *Current understanding of metal ions in the pathogenesis of Alzheimer's disease*. Transl Neurodegener, 2020. **9**: p. 10.
35. Villaseñor, R., et al., *Intracellular transport and regulation of transcytosis across the blood-brain barrier*. Cell Mol Life Sci, 2019. **76**(6): p. 1081-1092.
36. van Bree, J., et al., *Peptide transport across the blood-brain barrier*. Journal of Controlled Release, 1990. **13**(2-3): p. 175-184.
37. Abbott, N.J., et al., *Structure and function of the blood–brain barrier*. Neurobiology of disease, 2010. **37**(1): p. 13-25.

38. Lapilover, E., et al., *Peri-infarct blood–brain barrier dysfunction facilitates induction of spreading depolarization associated with epileptiform discharges*. *Neurobiology of disease*, 2012. **48**(3): p. 495-506.
39. Glezer, I., A. Simard, and S. Rivest, *Neuroprotective role of the innate immune system by microglia*. *Neuroscience*, 2007. **147**(4): p. 867-883.
40. Maggio, N., et al., *Thrombin induces long-term potentiation of reactivity to afferent stimulation and facilitates epileptic seizures in rat hippocampal slices: toward understanding the functional consequences of cerebrovascular insults*. *Journal of Neuroscience*, 2008. **28**(3): p. 732-736.
41. Nadal, A., et al., *Plasma albumin is a potent trigger of calcium signals and DNA synthesis in astrocytes*. *Proceedings of the National Academy of Sciences*, 1995. **92**(5): p. 1426-1430.
42. Gingrich, M.B. and S.F. Traynelis, *Serine proteases and brain damage—is there a link?* *Trends in neurosciences*, 2000. **23**(9): p. 399-407.
43. Cockerill, I., et al., *Blood-brain barrier integrity and clearance of amyloid- $\beta$  from the BBB*. *Molecular, cellular, and tissue engineering of the vascular system*, 2018: p. 261-278.
44. Engelhardt, B. and L. Sorokin, *The blood-brain and the blood-cerebrospinal fluid barriers: function and dysfunction*. *Semin Immunopathol*, 2009. **31**(4): p. 497-511.
45. Pardridge, W.M., *Blood-brain barrier carrier-mediated transport and brain metabolism of amino acids*. *Neurochemical research*, 1998. **23**(5): p. 635-644.
46. McAllister, M.S., et al., *Mechanisms of glucose transport at the blood–brain barrier: an in vitro study*. *Brain research*, 2001. **904**(1): p. 20-30.
47. Lepist, E.I., et al., *Transport of A1 adenosine receptor agonist tecadenoson by human and mouse nucleoside transporters: evidence for blood-brain barrier transport by murine equilibrative nucleoside transporter 1 mENT1*. *Drug Metab Dispos*, 2013. **41**(4): p. 916-22.
48. Tărlungeanu, D.C., et al., *Impaired Amino Acid Transport at the Blood Brain Barrier Is a Cause of Autism Spectrum Disorder*. *Cell*, 2016. **167**(6): p. 1481-1494.e18.
49. Duffy, K.R. and W.M. Pardridge, *Blood-brain barrier transcytosis of insulin in developing rabbits*. *Brain Res*, 1987. **420**(1): p. 32-8.
50. Fishman, J., et al., *Receptor - mediated transcytosis of transferrin across the blood - brain barrier*. *Journal of neuroscience research*, 1987. **18**(2): p. 299-304.
51. Schinkel, A.H., *P-Glycoprotein, a gatekeeper in the blood–brain barrier*. *Advanced drug delivery reviews*, 1999. **36**(2-3): p. 179-194.
52. Schinkel, A., et al., *Disruption of the mouse *mdr1a* P-glycoprotein gene leads to a deficiency in the blood-brain barrier and to increased sensitivity to drugs*. *Cell*, 1994. **77**(4): p. 491-502.
53. Hervé, F., N. Ghinea, and J.-M. Scherrmann, *CNS delivery via adsorptive transcytosis*. *The AAPS journal*, 2008. **10**(3): p. 455-472.
54. Chrétien, F., et al., *Pathogenesis of cerebral *Cryptococcus neoformans* infection after fungemia*. *The Journal of infectious diseases*, 2002. **186**(4): p. 522-530.
55. González-Scarano, F. and J. Martín-García, *The neuropathogenesis of AIDS*. *Nature reviews immunology*, 2005. **5**(1): p. 69-81.

56. Park, K., *Trojan monocytes for improved drug delivery to the brain*. Journal of Controlled Release, 2008. **2**(132): p. 75.
57. Pardridge, W.M., *Molecular Trojan horses for blood–brain barrier drug delivery*. Current opinion in pharmacology, 2006. **6**(5): p. 494-500.
58. Temsamani, J., et al., *Brain drug delivery technologies: novel approaches for transporting therapeutics*. Pharmaceutical science & technology today, 2000. **3**(5): p. 155-162.
59. Blasberg, R., C. Patlak, and J. Fenstermacher, *Intrathecal chemotherapy: brain tissue profiles after ventriculocisternal perfusion*. Journal of Pharmacology and Experimental Therapeutics, 1975. **195**(1): p. 73-83.
60. Krewson, C.E., M.L. Klarman, and W.M. Saltzman, *Distribution of nerve growth factor following direct delivery to brain interstitium*. Brain research, 1995. **680**(1-2): p. 196-206.
61. Voges, J., et al., *Imaging - guided convection - enhanced delivery and gene therapy of glioblastoma*. Annals of Neurology: Official Journal of the American Neurological Association and the Child Neurology Society, 2003. **54**(4): p. 479-487.
62. Ai, Y., et al., *Intrapatamenal infusion of GDNF in aged rhesus monkeys: distribution and dopaminergic effects*. Journal of Comparative Neurology, 2003. **461**(2): p. 250-261.
63. Greenwood, J., et al., *Hyperosmolar opening of the blood-brain barrier in the energy-depleted rat brain. Part 1. Permeability studies*. Journal of Cerebral Blood Flow & Metabolism, 1988. **8**(1): p. 9-15.
64. Kroll, R.A., E.A. Neuwelt, and E.A. Neuwelt, *Outwitting the blood-brain barrier for therapeutic purposes: osmotic opening and other means*. Neurosurgery, 1998. **42**(5): p. 1083-1099.
65. Doolittle, N.D., et al., *Blood-brain barrier disruption for the treatment of malignant brain tumors: The National Program*. Journal of Neuroscience Nursing, 1998. **30**(2): p. 81-91.
66. Salahuddin, T., et al., *Observations on exsudation of fibronectin, fibrinogen and albumin in the brain after carotid infusion of hyperosmolar solutions*. Acta neuropathologica, 1988. **76**(1): p. 1-10.
67. Matsukado, K., et al., *Enhanced tumor uptake of carboplatin and survival in glioma-bearing rats by intracarotid infusion of bradykinin analog, RMP-7*. Neurosurgery, 1996. **39**(1): p. 125-134.
68. Bartus, R.T., et al., *Intravenous cereport (RMP-7) modifies topographic uptake profile of carboplatin within rat glioma and brain surrounding tumor, elevates platinum levels, and enhances survival*. Journal of Pharmacology and Experimental Therapeutics, 2000. **293**(3): p. 903-911.
69. Emerich, D.F., et al., *Intravenous cereport (RMP-7) enhances delivery of hydrophilic chemotherapeutics and increases survival in rats with metastatic tumors in the brain*. Pharmaceutical research, 2000. **17**(10): p. 1212-1219.
70. Stamatovic, S.M., R.F. Keep, and A.V. Andjelkovic, *Brain endothelial cell-cell junctions: how to “open” the blood brain barrier*. Current neuropharmacology, 2008. **6**(3): p. 179-192.

71. Hwang, S.R. and K. Kim, *Nano-enabled delivery systems across the blood–brain barrier*. Archives of pharmacal research, 2014. **37**(1): p. 24-30.
72. Erdlenbruch, B., et al., *Alkylglycerol opening of the blood – brain barrier to small and large fluorescence markers in normal and C6 glioma – bearing rats and isolated rat brain capillaries*. British journal of pharmacology, 2003. **140**(7): p. 1201-1210.
73. Patel, M.M., et al., *Getting into the brain: approaches to enhance brain drug delivery*. CNS Drugs, 2009. **23**(1): p. 35-58.
74. Rautio, J., et al., *Prodrug approaches for CNS delivery*. The AAPS journal, 2008. **10**(1): p. 92-102.
75. Misra, A., et al., *Drug delivery to the central nervous system: a review*. J Pharm Pharm Sci, 2003. **6**(2): p. 252-273.
76. Pardridge, W.M., *Blood–brain barrier delivery*. Drug discovery today, 2007. **12**(1-2): p. 54-61.
77. Pardridge, W.M., *Recent advances in blood-brain barrier transport*. Annual review of pharmacology and toxicology, 1988. **28**(1): p. 25-39.
78. Lambert, D.M., *Rationale and applications of lipids as prodrug carriers*. European journal of pharmaceutical sciences, 2000. **11**: p. S15-S27.
79. Greig, N.H., et al., *Pharmacokinetics of chlorambucil-tertiary butyl ester, a lipophilic chlorambucil derivative that achieves and maintains high concentrations in brain*. Cancer chemotherapy and pharmacology, 1990. **25**(5): p. 320-325.
80. Pardridge, W.M., *Drug targeting to the brain*. Pharmaceutical research, 2007. **24**(9): p. 1733-1744.
81. Pardridge, W.M., *Blood-brain barrier drug targeting: the future of brain drug development*. Molecular interventions, 2003. **3**(2): p. 90.
82. Bodor, N., *Drug targeting and retrometabolic drug design approaches introduction*. Advanced drug delivery reviews, 1994. **14**(2-3): p. 157-166.
83. Kumagai, A.K., J.B. Eisenberg, and W.M. Pardridge, *Absorptive-mediated endocytosis of cationized albumin and a beta-endorphin-cationized albumin chimeric peptide by isolated brain capillaries. Model system of blood-brain barrier transport*. J Biol Chem, 1987. **262**(31): p. 15214-9.
84. Pardridge, W.M., D. Triguero, and J.L. Buciak, *Beta-endorphin chimeric peptides: transport through the blood-brain barrier in vivo and cleavage of disulfide linkage by brain*. Endocrinology, 1990. **126**(2): p. 977-84.
85. Triguero, D., et al., *Blood-brain barrier transport of cationized immunoglobulin G: enhanced delivery compared to native protein*. Proc Natl Acad Sci U S A, 1989. **86**(12): p. 4761-5.
86. Pardridge, W.M., D. Triguero, and J. Buciak, *Transport of histone through the blood-brain barrier*. Journal of Pharmacology and Experimental Therapeutics, 1989. **251**(3): p. 821-826.
87. Pardridge, W.M., et al., *Protamine-mediated transport of albumin into brain and other organs of the rat. Binding and endocytosis of protamine-albumin complex by microvascular endothelium*. The Journal of clinical investigation, 1993. **92**(5): p. 2224-2229.

88. Schwarze, S.R., et al., *In vivo protein transduction: delivery of a biologically active protein into the mouse*. Science, 1999. **285**(5433): p. 1569-1572.
89. Oldendorf, W.H., *Brain uptake of radiolabeled amino acids, amines, and hexoses after arterial injection*. American Journal of Physiology-Legacy Content, 1971. **221**(6): p. 1629-1639.
90. Mena, I. and G.C. Cotzias, *Protein intake and treatment of Parkinson's disease with levodopa*. New England Journal of Medicine, 1975. **292**(4): p. 181-184.
91. Dairman, W., J.G. Christenson, and S. Udenfriend, *Decrease in liver aromatic L-amino-acid decarboxylase produced by chronic administration of L-dopa*. Proc Natl Acad Sci U S A, 1971. **68**(9): p. 2117-20.
92. Pardridge, W.M., R.J. Boado, and C.R. Farrell, *Brain-type glucose transporter (GLUT-1) is selectively localized to the blood-brain barrier. Studies with quantitative western blotting and in situ hybridization*. Journal of Biological Chemistry, 1990. **265**(29): p. 18035-18040.
93. Anderson, B.D., *Prodrugs for improved CNS delivery*. Advanced drug delivery reviews, 1996. **19**(2): p. 171-202.
94. Bonina, F.P., et al., *Synthesis, stability, and pharmacological evaluation of nipectic acid prodrugs*. Journal of pharmaceutical sciences, 1999. **88**(5): p. 561-567.
95. Bonina, F.P., et al., *Synthesis, pharmacokinetics and anticonvulsant activity of 7-chlorokynurenic acid prodrugs*. International journal of pharmaceutics, 2000. **202**(1-2): p. 79-88.
96. Gynther, M., et al., *Large neutral amino acid transporter enables brain drug delivery via prodrugs*. Journal of medicinal chemistry, 2008. **51**(4): p. 932-936.
97. Gao, B., et al., *Organic anion-transporting polypeptides mediate transport of opioid peptides across blood-brain barrier*. Journal of Pharmacology and Experimental Therapeutics, 2000. **294**(1): p. 73-79.
98. Hosokawa, H., et al., *Cloning and characterization of a brain-specific cationic amino acid transporter*. Journal of Biological Chemistry, 1997. **272**(13): p. 8717-8722.
99. Vijay, N. and M.E. Morris, *Role of monocarboxylate transporters in drug delivery to the brain*. Current pharmaceutical design, 2014. **20**(10): p. 1487-1498.
100. Chishty, M., et al., *Interaction of nucleoside analogues with nucleoside transporters in rat brain endothelial cells*. Journal of drug targeting, 2004. **12**(5): p. 265-272.
101. Cornford, E.M., L.D. Braun, and W.H. Oldendorf, *Carrier mediated blood - brain barrier transport of choline and certain choline analogs*. Journal of neurochemistry, 1978. **30**(2): p. 299-308.
102. Patching, S.G., *Glucose transporters at the blood-brain barrier: function, regulation and gateways for drug delivery*. Molecular neurobiology, 2017. **54**(2): p. 1046-1077.
103. Kannan, R., et al., *GSH transport in immortalized mouse brain endothelial cells: Evidence for apical localization of a sodium - dependent GSH transporter*. Journal of neurochemistry, 1999. **73**(1): p. 390-399.

104. Iantomasi, T., F. Favilli, and M.T. Vincenzini, *Evidence of glutathione transporter in rat brain synaptosomal membrane vesicles*. Neurochemistry international, 1999. **34**(6): p. 509-516.
105. Duffy, K.R. and W.M. Pardridge, *Blood-brain barrier transcytosis of insulin in developing rabbits*. Brain research, 1987. **420**(1): p. 32-38.
106. Boado, R.J., et al., *Up-regulation of blood-brain barrier short-form leptin receptor gene products in rats fed a high fat diet*. J Neurochem, 1998. **71**(4): p. 1761-4.
107. Zhang, Y. and W.M. Pardridge, *Rapid transferrin efflux from brain to blood across the blood-brain barrier*. Journal of neurochemistry, 2001. **76**(5): p. 1597-1600.
108. Schlachetzki, F., C. Zhu, and W.M. Pardridge, *Expression of the neonatal Fc receptor (FcRn) at the blood-brain barrier*. Journal of neurochemistry, 2002. **81**(1): p. 203-206.
109. Laske, D.W., R.J. Youle, and E.H. Oldfield, *Tumor regression with regional distribution of the targeted toxin TF-CRM107 in patients with malignant brain tumors*. Nature medicine, 1997. **3**(12): p. 1362-1368.
110. Pardridge, W.M., *Receptor-mediated peptide transport through the blood-brain barrier*. Endocrine reviews, 1986. **7**(3): p. 314-330.
111. Pardridge, W.M., *Blood-brain barrier drug delivery of IgG fusion proteins with a transferrin receptor monoclonal antibody*. Expert opinion on drug delivery, 2015. **12**(2): p. 207-222.
112. Derakhshan, F. and C. Toth, *Insulin and the brain*. Current diabetes reviews, 2013. **9**(2): p. 102-116.
113. Werner, H. and D. LeRoith, *Insulin and insulin-like growth factor receptors in the brain: physiological and pathological aspects*. European Neuropsychopharmacology, 2014. **24**(12): p. 1947-1953.
114. Johnsen, K.B., et al., *Targeting the transferrin receptor for brain drug delivery*. Progress in neurobiology, 2019. **181**: p. 101665.
115. Banks, W., et al., *Principles of strategic drug delivery to the brain (SDDB): development of anorectic and orexigenic analogs of leptin*. Physiology & behavior, 2011. **105**(1): p. 145-149.
116. Wu, D. and W.M. Pardridge, *Blood-brain barrier transport of reduced folic acid*. Pharmaceutical research, 1999. **16**(3): p. 415-419.
117. Alam, M.I., et al., *Strategy for effective brain drug delivery*. European journal of pharmaceutical sciences, 2010. **40**(5): p. 385-403.
118. Dehouck, B., et al., *A new function for the LDL receptor: transcytosis of LDL across the blood-brain barrier*. The Journal of cell biology, 1997. **138**(4): p. 877-889.
119. Shaik, N., et al., *P-glycoprotein-mediated active efflux of the anti-HIV1 nucleoside abacavir limits cellular accumulation and brain distribution*. Drug metabolism and disposition, 2007. **35**(11): p. 2076-2085.
120. Schinkel, A.H., et al., *Absence of the mdr1a P-Glycoprotein in mice affects tissue distribution and pharmacokinetics of dexamethasone, digoxin, and cyclosporin A*. The Journal of clinical investigation, 1995. **96**(4): p. 1698-1705.

121. Kawamura, K., et al., *In vivo evaluation of P-glycoprotein and breast cancer resistance protein modulation in the brain using [11C] gefitinib*. Nuclear medicine and biology, 2009. **36**(3): p. 239-246.
122. de Vries, N.A., et al., *P-glycoprotein and breast cancer resistance protein: two dominant transporters working together in limiting the brain penetration of topotecan*. Clinical Cancer Research, 2007. **13**(21): p. 6440-6449.
123. Dallas, S., L. Schlichter, and R. Bendayan, *Multidrug resistance protein (MRP) 4- and MRP 5-mediated efflux of 9-(2-phosphonylmethoxyethyl) adenine by microglia*. Journal of Pharmacology and Experimental Therapeutics, 2004. **309**(3): p. 1221-1229.
124. Leggas, M., et al., *Mrp4 confers resistance to topotecan and protects the brain from chemotherapy*. Molecular and cellular biology, 2004. **24**(17): p. 7612-7621.
125. Thorne, R.G., et al., *Quantitative analysis of the olfactory pathway for drug delivery to the brain*. Brain research, 1995. **692**(1-2): p. 278-282.
126. Tiwari, S.B. and M.M. Amiji, *A review of nanocarrier-based CNS delivery systems*. Current drug delivery, 2006. **3**(2): p. 219-232.
127. Sonali, et al., *Transferrin receptor-targeted vitamin E TPGS micelles for brain cancer therapy: preparation, characterization and brain distribution in rats*. Drug delivery, 2016. **23**(5): p. 1788-1798.
128. Hülsermann, U., et al., *Uptake of apolipoprotein E fragment coupled liposomes by cultured brain microvessel endothelial cells and intact brain capillaries*. Journal of drug targeting, 2009. **17**(8): p. 610-618.
129. Shilo, M., et al., *Transport of nanoparticles through the blood-brain barrier for imaging and therapeutic applications*. Nanoscale, 2014. **6**(4): p. 2146-2152.
130. He, H., et al., *Solid lipid nanoparticles as a drug delivery system to across the blood-brain barrier*. Biochemical and biophysical research communications, 2019. **519**(2): p. 385-390.
131. Roberts, H.C., et al., *Quantitative measurement of microvascular permeability in human brain tumors achieved using dynamic contrast-enhanced MR imaging: correlation with histologic grade*. American Journal of Neuroradiology, 2000. **21**(5): p. 891-899.
132. Thöle, M., et al., *Uptake of cationized albumin coupled liposomes by cultured porcine brain microvessel endothelial cells and intact brain capillaries*. Journal of drug targeting, 2002. **10**(4): p. 337-344.
133. Rao, K.S., et al., *TAT-conjugated nanoparticles for the CNS delivery of anti-HIV drugs*. Biomaterials, 2008. **29**(33): p. 4429-4438.
134. Li, L., et al., *Large amino acid transporter 1 mediated glutamate modified docetaxel-loaded liposomes for glioma targeting*. Colloids and Surfaces B: Biointerfaces, 2016. **141**: p. 260-267.
135. Kuo, Y.-C. and C.-Y. Chung, *Transcytosis of CRM197-grafted polybutylcyanoacrylate nanoparticles for delivering zidovudine across human brain-microvascular endothelial cells*. Colloids and Surfaces B: Biointerfaces, 2012. **91**: p. 242-249.
136. Jones, A.R. and E.V. Shusta, *Blood-brain barrier transport of therapeutics via receptor-mediation*. Pharmaceutical research, 2007. **24**(9): p. 1759-1771.

137. Bao, H., et al., *OX26 modified hyperbranched polyglycerol-conjugated poly (lactic-co-glycolic acid) nanoparticles: synthesis, characterization and evaluation of its brain delivery ability*. Journal of Materials Science: Materials in Medicine, 2012. **23**(8): p. 1891-1901.
138. Saul, J.M., et al., *Controlled targeting of liposomal doxorubicin via the folate receptor in vitro*. Journal of Controlled Release, 2003. **92**(1-2): p. 49-67.
139. Bhattacharya, R., et al., *Targeted Delivery of Complexes of Biotin-PEG-Polyethylenimine and NF- $\kappa$ B Decoys to Brain-derived Endothelial Cells in Vitro*. Pharmaceutical research, 2008. **25**(3): p. 605-615.
140. Ulbrich, K., T. Knobloch, and J. Kreuter, *Targeting the insulin receptor: nanoparticles for drug delivery across the blood-brain barrier (BBB)*. Journal of drug targeting, 2011. **19**(2): p. 125-132.
141. Hu, K., et al., *Lactoferrin conjugated PEG-PLGA nanoparticles for brain delivery: preparation, characterization and efficacy in Parkinson's disease*. International journal of pharmaceutics, 2011. **415**(1-2): p. 273-283.
142. Wang, Z.H., et al., *Trimethylated chitosan-conjugated PLGA nanoparticles for the delivery of drugs to the brain*. Biomaterials, 2010. **31**(5): p. 908-915.
143. Shevtsov, M.A., et al., *Superparamagnetic iron oxide nanoparticles conjugated with epidermal growth factor (SPION-EGF) for targeting brain tumors*. International journal of nanomedicine, 2014. **9**: p. 273.
144. Gonzalez-Carter, D., et al., *Targeting nanoparticles to the brain by exploiting the blood-brain barrier impermeability to selectively label the brain endothelium*. Proceedings of the National Academy of Sciences, 2020. **117**(32): p. 19141-19150.
145. Dringen, R., *Metabolism and functions of glutathione in brain*. Progress in neurobiology, 2000. **62**(6): p. 649-671.
146. Orłowski, M. and A. Karkowsky, *Glutathione metabolism and some possible functions of glutathione in the nervous system*, in *International review of neurobiology*. 1976, Elsevier. p. 75-121.
147. Kannan, R., et al., *Carrier-mediated GSH transport at the blood-brain barrier and molecular characterization of novel brain GSH transporters*. Glutathione in the nervous system, 1998: p. 45-62.
148. Kannan, R., et al., *GSH transport in human cerebrovascular endothelial cells and human astrocytes: evidence for luminal localization of Na<sup>+</sup>-dependent GSH transport in HCEC*. Brain research, 2000. **852**(2): p. 374-382.
149. Kannan, R., et al., *Evidence for carrier-mediated transport of glutathione across the blood-brain barrier in the rat*. The Journal of clinical investigation, 1990. **85**(6): p. 2009-2013.
150. Slivka, A., C. Mytilineou, and G. Cohen, *Histochemical evaluation of glutathione in brain*. Brain research, 1987. **409**(2): p. 275-284.
151. Lv, H., et al., *Unraveling the potential role of glutathione in multiple forms of cell death in cancer therapy*. Oxidative medicine and cellular longevity, 2019. **2019**.
152. Gaillard, P.J., et al., *Pharmacokinetics, brain delivery, and efficacy in brain tumor-bearing mice of glutathione pegylated liposomal doxorubicin (2B3-101)*. PloS one, 2014. **9**(1): p. e82331.

153. Birngruber, T., et al., *Enhanced doxorubicin delivery to the brain administered through glutathione PEGylated liposomal doxorubicin (2B3-101) as compared with generic Caelyx,®/Doxil®—a cerebral open flow microperfusion pilot study*. Journal of pharmaceutical sciences, 2014. **103**(7): p. 1945-1948.
154. Gaillard, P.J., et al., *Enhanced brain delivery of liposomal methylprednisolone improved therapeutic efficacy in a model of neuroinflammation*. Journal of controlled release, 2012. **164**(3): p. 364-369.
155. Lindqvist, A., et al., *Enhanced brain delivery of the opioid peptide DAMGO in glutathione pegylated liposomes: a microdialysis study*. Molecular pharmaceutics, 2013. **10**(5): p. 1533-1541.
156. Englert, C., et al., *Crossing the blood-brain barrier: Glutathione-conjugated poly (ethylene imine) for gene delivery*. Journal of Controlled Release, 2016. **241**: p. 1-14.
157. Nosrati, H., et al., *Glutathione (GSH) peptide conjugated magnetic nanoparticles as blood–brain barrier shuttle for MRI-monitored brain delivery of paclitaxel*. ACS Biomaterials Science & Engineering, 2019. **5**(4): p. 1677-1685.
158. More, S.S. and R. Vince, *Design, synthesis and biological evaluation of glutathione peptidomimetics as components of anti-Parkinson prodrugs*. Journal of medicinal chemistry, 2008. **51**(15): p. 4581-4588.
159. Najmi, A., et al., *2-(2-Cholesteroxyethoxyl)ethyl 3'-S-glutathionylpropionate and its self-assembled micelles for brain delivery: Design, synthesis and evaluation*. International Journal of Pharmaceutics, 2021. **600**: p. 120520.
160. Kim, S., et al., *Overcoming the barriers in micellar drug delivery: loading efficiency, in vivo stability, and micelle–cell interaction*. Expert opinion on drug delivery, 2010. **7**(1): p. 49-62.
161. Feng, X., et al., *Methoxy poly (ethylene glycol)-conjugated linoleic acid polymeric micelles for paclitaxel delivery*. Colloid Journal, 2006. **68**(6): p. 779-783.
162. Kulkarni, V.S. and C. Shaw, *Essential chemistry for formulators of semisolid and liquid dosages*. 2015: Academic Press.
163. Cabral, H., et al., *Accumulation of sub-100 nm polymeric micelles in poorly permeable tumours depends on size*. Nature nanotechnology, 2011. **6**(12): p. 815-823.
164. Fox, M.E., F.C. Szoka, and J.M. Fréchet, *Soluble polymer carriers for the treatment of cancer: the importance of molecular architecture*. Accounts of chemical research, 2009. **42**(8): p. 1141-1151.
165. Venkatachalam, M.A. and H.G. Rennke, *The structural and molecular basis of glomerular filtration*. Circulation research, 1978. **43**(3): p. 337-347.
166. Jain, R.K., *Transport of molecules across tumor vasculature*. Cancer and Metastasis Reviews, 1987. **6**(4): p. 559-593.
167. Jiang, W., et al., *Nanoparticle-mediated cellular response is size-dependent*. Nature nanotechnology, 2008. **3**(3): p. 145-150.
168. Tang, L., et al., *Investigating the optimal size of anticancer nanomedicine*. Proceedings of the National Academy of Sciences, 2014. **111**(43): p. 15344-15349.

169. Lamb, M., et al., *In vitro maturation of viable islets from partially digested young pig pancreas*. Cell Transplant, 2014. **23**(3): p. 263-72.
170. Lu, Y., et al., *Strategies to improve micelle stability for drug delivery*. Nano Res, 2018. **11**(10): p. 4985-4998.
171. Lu, Y., et al., *Micelles with ultralow critical micelle concentration as carriers for drug delivery*. Nature biomedical engineering, 2018. **2**(5): p. 318-325.
172. Bloch, K., *Cholesterol: evolution of structure and function*, in *New Comprehensive Biochemistry*. 1991, Elsevier. p. 363-381.
173. Xiangming, G., et al., *Glutathione-cholesterol derivatives as brain targeting agents*. 2020, Google Patents.
174. Lassila, T., et al., *Tandem mass spectrometric analysis of S - and N - linked glutathione conjugates of pulegone and menthofuran and identification of P450 enzymes mediating their formation*. Rapid Communications in Mass Spectrometry, 2016. **30**(7): p. 917-926.
175. Daman, Z., et al., *Preparation, optimization and in vitro characterization of stearyl-gemcitabine polymeric micelles: a comparison with its self-assembled nanoparticles*. Int J Pharm, 2014. **468**(1-2): p. 142-51.
176. Pineiro, L., M. Novo, and W. Al-Soufi, *Fluorescence emission of pyrene in surfactant solutions*. Adv Colloid Interface Sci, 2015. **215**: p. 1-12.
177. Meng, X., et al., *Pluronic F127 and D-alpha-Tocopheryl Polyethylene Glycol Succinate (TPGS) Mixed Micelles for Targeting Drug Delivery across The Blood Brain Barrier*. Sci Rep, 2017. **7**(1): p. 2964.
178. Zhan, C., et al., *Micelle-based brain-targeted drug delivery enabled by a nicotine acetylcholine receptor ligand*. Angew Chem Int Ed Engl, 2011. **50**(24): p. 5482-5.
179. Jiang, Y., et al., *Enhanced Antiglioma Efficacy of Ultrahigh Loading Capacity Paclitaxel Prodrug Conjugate Self-Assembled Targeted Nanoparticles*. ACS Appl Mater Interfaces, 2017. **9**(1): p. 211-217.
180. Xie, Y.T., et al., *Brain-targeting study of stearic acid-grafted chitosan micelle drug-delivery system*. Int J Nanomedicine, 2012. **7**: p. 3235-44.
181. Xie, F., et al., *Investigation of glucose-modified liposomes using polyethylene glycols with different chain lengths as the linkers for brain targeting*. Int J Nanomedicine, 2012. **7**: p. 163-75.
182. Li, F., et al., *Preparation and Characterization of Lipophilic Doxorubicin Pro-drug Micelles*. J Vis Exp, 2016(114).
183. Meng, X.Y., et al., *Electro-responsive brain-targeting mixed micelles based on Pluronic F127 and D- $\alpha$ -tocopherol polyethylene glycol succinate-ferrocene*. Colloids and Surfaces A: Physicochemical and Engineering Aspects, 2020. **601**: p. 124986.
184. More, S.S. and R. Vince, *Design, synthesis and biological evaluation of glutathione peptidomimetics as components of anti-Parkinson prodrugs*. J Med Chem, 2008. **51**(15): p. 4581-8.
185. Hagos, F.T., et al., *Probenecid, an organic anion transporter 1 and 3 inhibitor, increases plasma and brain exposure of N-acetylcysteine*. Xenobiotica; the fate of foreign compounds in biological systems, 2017. **47**(4): p. 346-353.
186. Hagen, T.M., T.Y. Aw, and D.P. Jones, *Glutathione uptake and protection against oxidative injury in isolated kidney cells*. Kidney Int, 1988. **34**(1): p. 74-81.

187. Gu, G., et al., *PEG-co-PCL nanoparticles modified with MMP-2/9 activatable low molecular weight protamine for enhanced targeted glioblastoma therapy*. *Biomaterials*, 2013. **34**(1): p. 196-208.
188. Jiang, Y., et al., *Enhanced antiglioma efficacy of ultrahigh loading capacity paclitaxel prodrug conjugate self-assembled targeted nanoparticles*. *ACS applied materials & interfaces*, 2017. **9**(1): p. 211-217.
189. Li, X.-Y., et al., *Multifunctional liposomes loaded with paclitaxel and artemether for treatment of invasive brain glioma*. *Biomaterials*, 2014. **35**(21): p. 5591-5604.
190. Zhang, B., et al., *LDLR-mediated peptide-22-conjugated nanoparticles for dual-targeting therapy of brain glioma*. *Biomaterials*, 2013. **34**(36): p. 9171-9182.
191. Zhang, Y.-N., et al., *Nanoparticle–liver interactions: cellular uptake and hepatobiliary elimination*. *Journal of controlled release*, 2016. **240**: p. 332-348.
192. Consigli, R.A., J. Zabielski, and R. Weil, *Plaque assay for polyoma virus on primary mouse kidney cell cultures*. *Appl Microbiol*, 1973. **26**(4): p. 627-8.
193. Ding, W., K. Yousefi, and L.A. Shehadeh, *Isolation, Characterization, And High Throughput Extracellular Flux Analysis of Mouse Primary Renal Tubular Epithelial Cells*. *J Vis Exp*, 2018(136).
194. Consigli, R.A., J. Zabielski, and R. Weil, *Plaque assay for polyoma virus on primary mouse kidney cell cultures*. *Applied microbiology*, 1973. **26**(4): p. 627.
195. Cai, L., M. Gochin, and K. Liu, *A facile surfactant critical micelle concentration determination*. *Chemical Communications*, 2011. **47**(19): p. 5527-5529.
196. Li, F., et al., *Preparation and Characterization of Lipophilic Doxorubicin Pro-drug Micelles*. *JoVE (Journal of Visualized Experiments)*, 2016(114): p. e54338.
197. Noweck, K. and W. Grafahrend, *Fatty alcohols*. *Ullmann's encyclopedia of industrial chemistry*, 2000.
198. Aungst, B.J., N. J. Rogers, and E. Shefter, *Enhancement of naloxone penetration through human skin in vitro using fatty acids, fatty alcohols, surfactants, sulfoxides and amides*. *International Journal of Pharmaceutics*, 1986. **33**(1): p. 225-234.
199. Dong, X. and R. Mumper, *The metabolism of fatty alcohols in lipid nanoparticles by alcohol dehydrogenase*. *Drug development and industrial pharmacy*, 2006. **32**(8): p. 973-980.
200. Müller-Goymann, C.C., *Physicochemical characterization of colloidal drug delivery systems such as reverse micelles, vesicles, liquid crystals and nanoparticles for topical administration*. *European Journal of Pharmaceutics and Biopharmaceutics*, 2004. **58**(2): p. 343-356.
201. Xie, Y.-T., et al., *Brain-targeting study of stearic acid–grafted chitosan micelle drug-delivery system*. *International journal of nanomedicine*, 2012. **7**: p. 3235.
202. Hagen, T.M., T.Y. Aw, and D.P. Jones, *Glutathione uptake and protection against oxidative injury in isolated kidney cells*. *Kidney international*, 1988. **34**(1): p. 74-81.
203. Geldenhuys, W., et al., *Brain-targeted delivery of doxorubicin using glutathione-coated nanoparticles for brain cancers*. *Pharmaceutical development and technology*, 2015. **20**(4): p. 497-506.

204. Raval, N., et al., *Development of glutathione - conjugated asiatic acid - loaded bovine serum albumin nanoparticles for brain - targeted drug delivery*. Journal of Pharmacy and Pharmacology, 2015. **67**(11): p. 1503-1511.
205. Park, J., et al., *Bile acid transporter mediated endocytosis of oral bile acid conjugated nanocomplex*. Biomaterials, 2017. **147**: p. 145-154.
206. Al-Hasani, H., C.S. Hinck, and S.W. Cushman, *Endocytosis of the glucose transporter GLUT4 is mediated by the GTPase dynamin*. Journal of Biological Chemistry, 1998. **273**(28): p. 17504-17510.
207. Zou, D., et al., *Penetration of blood–brain barrier and antitumor activity and nerve repair in glioma by doxorubicin-loaded monosialoganglioside micelles system*. International journal of nanomedicine, 2017. **12**: p. 4879.
208. Li, C., et al., *Paclitaxel-loaded cholesterol-conjugated polyoxyethylene sorbitol oleate polymeric micelles for glioblastoma therapy across the blood–brain barrier*. Polymer Chemistry, 2015. **6**(14): p. 2740-2751.
209. Ecker, D.M., S.D. Jones, and H.L. Levine. *The therapeutic monoclonal antibody market*. in *MAbs*. 2015. Taylor & Francis.
210. Lu, R.-M., et al., *Development of therapeutic antibodies for the treatment of diseases*. Journal of biomedical science, 2020. **27**(1): p. 1-30.
211. Ryman, J.T. and B. Meibohm, *Pharmacokinetics of monoclonal antibodies*. CPT: pharmacometrics & systems pharmacology, 2017. **6**(9): p. 576-588.
212. Ryman, J.T. and B. Meibohm, *Pharmacokinetics of Monoclonal Antibodies*. CPT Pharmacometrics Syst Pharmacol, 2017. **6**(9): p. 576-588.